芝浦工業大學

SHIBAURA INSTITUTE OF TECHNOLOGY

GRADUATE SCHOOL OF SCIENCE AND ENGINEERING

REGIONAL ENVIRONMENT SYSTEM

DOCTORAL THESIS

GROWTH AND CHARACTERIZATION OF THERMOELECTRIC THIN FILMS FOR HEAT HARVESTING

Candidate:

Giovanna LATRONICO
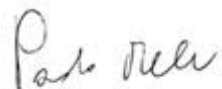
Supervisor: Prof. Paolo MELE

March 2022

DECLARATION

I hereby declare that except where specific reference is made to the work of others, the contents of this dissertation are original and have not been submitted in whole or in part for consideration for any other degree or qualification in this, or any other university. This dissertation is my own work and contains nothing that is the outcome of work done in collaboration with others, except as specified in the text and acknowledgements.

Signed: Giovanna LATRONICO, NA19103

Certified by: Prof. Paolo MELE

ABSTRACT

The increasing worldwide demand for energy and the resultant depletion of fossil fuels have brought new challenges for the scientific community [1]. One of the major issues is to develop high-efficiency devices for capturing energy from abundant natural sources such as solar wind and geothermal energy. Another surplus, but mostly unused, source of energy is waste heat. There are huge waste heat sources in our environments covering a wide range of temperatures (300~1200 K): industrial processes, domestic stoves and radiators, lighting, pipelines, electrical substations, subway networks, automotive exhaust tubes, but also geothermal heat, body heat, and so on: about 66 % of the of annual world energy consumption is lost as waste heat, and the loss corresponds to the stellar amount of $3 \cdot 10^{20}$ J per year, just considering the past 10 years [2,3]. A highly promising method for energy recovery from such heat sources is the utilization of thermoelectric (TE) devices that can convert various types of waste heat flows into electricity.

The TE performance of a material is expressed by means of the concept of figure of merit, Z, defined by E. Altenkirch at the beginning of the XX century [4], a relation expressed by means of the electrical conductivity σ, Seebeck coefficient S and thermal conductivity κ. Seeing that Z differs with absolute temperature T, an advantageous way to display the efficiency is the non-dimensional figure-of-merit ZT. Commonly, ZT values of both the n-type and p-type TE materials contribute to the definition of the efficiency of a thermoelectric device.

State-of-the-art TE materials for heat conversion can operate at $T = 300 \sim 1200$ K, with $ZT = 0.1 \sim 2.6$, corresponding to an efficiency in the range of $1 \sim 20\%$. Therefore, after two centuries, TE devices are seldom utilized in daily life. TE modules have obtained brilliant success, though in niche applications (powering space probe Cassini [5]) while high-conversion modules to harvest waste heat of car engines remained at the state of prototypes [6]. The efficiency of TE must be strongly improved to make them competitive with the common

[1] S. Chu, A. Majumdar, "Opportunities and challenges for a sustainable energy future", *Nature* **2012**, *488*, 294–303.

[2] BP statistical review of world energy **2021**, https://www.bp.com/en/global/corporate/energy-economics/statistical-review-of-world-energy.html

[3] Annual energy flow charts by Lawrence Livermore Nat. Lab. https://flowcharts.llnl.gov/commodities/energy

[4] CRC *Handbook of Thermoelectrics* (ed. D.M. Rowe), CRC Press Inc. **1995**.

[5] V. Mireles J. W. Stultz, "Radioisotope Thermoelectric Generator Waste Heat System for the Cassini Propulsion Module", *J. Aerosp. Eng.* **1994**, SAE Transactions, *103*(1), 548-556.

[6] D. Crane, J. LaGrandeur, V. Jovovic, M. Ranalli, M. Adldinger, E. Poliquin, J. Dean, D. Kossakovski, B. Mazar, C. Maranville, "TEG On-Vehicle Performance and Model Validation and What It Means for Further TEG Development", *J. Electron. Mater*. **2013**, *42*, 1582–1591.

thermodynamic cycles based on fossil fuel burning, solar conversion and nuclear power plants. The improvement of *ZT* can be obtained by enhancing σ and/or *S*, or the product σS^2 which is called power factor, and/or by decreasing the total thermal conductivity.

In the past decade, due to their amazing advantages, such as light weight, flexibility and small sizes, thin films emerged in the thermoelectric research field. They can be considered competitive in meeting the requirements for micro-machines and small-scale accessories, such as micro-coolers, micro-power generators, micro-sensors [7]. Flexible thin films have the potential to be useful for wearable devices, while transparent thin films, like ZnO, can be employed on external glass walls or electronic screens for heat harvesting purposes. Regarding efficiency, thin films are interesting for TE applications because their structure opens various paths to enhance thermoelectric properties. It is common knowledge that the interface between the film and the substrate, or the ones between multilayers, have a significant effect on the grain growth, which tunability can be used to control TE performances.

This thesis is articulated into seven chapters. In Chapters 1, 2 and 3 a general introduction about thermoelectricity is followed by some experimental details of interest regarding the research conducted during the doctoral program. Thermoelectric thin films of various materials were prepared and characterized with various techniques. In Chapter 4, two complementary works regarding novel Fe,Ni-based filled skutterudites thin films deposited via Pulsed Laser Deposition (PLD) are reported. Substrate temperature and consecutive annealing were optimized in order to tune the thermoelectric properties of the material. Moreover, a preliminary study of the performances of a thin film module composed of only Fe,Ni-based filled skutterudite's legs was carried out as well. Chapter 5 is dedicated to aluminium-doped zinc oxide (AZO) and the study is aiming to investigate the effect of SnO_2 doping on thermoelectric properties of PLD AZO thin films. A preliminary study regarding Co-doped copper aluminium oxide is the main topic of Chapter 6. Best conditions to deposit the desired phase by PLD were explored, including annealing processes. Chapter 7 is dedicated to a general summary of conclusions and perspective of all the previous themes part of this doctoral thesis.

---

[7] X. Chen, Z. Zhou, Y.H. Lin, C. Nan, "Thermoelectric thin films: Promising strategies and related mechanism on boosting energy conversion performance", *J. Materiomics* **2020**, *6*(3), 494-512.

Contents

1 INTRODUCTION

In the last 40 years, the worldwide total energy supply has been improved from 5500 Mtoe in 1971 to 14300 Mtoe in 2018 (toe = tonne of oil equivalent, 1 toe = 11.63 MWh) in order to face the ceaseless growth of energy consumption. The main energy sources are oil (31.5%), coal (28.9%) and natural gas (22.8%). Biofuels, nuclear energy, hydroelectricity and other energy sources (including renewable energy) are still limited to 18.8%, even though they are slightly expanding [1].

The increasing global energy demand together with the health and environmental consequences of the consumption of fossil fuels are becoming increasingly alarming, leading scientists to search for new sustainable energy sources and energy-saving routes, increasing energy efficiency, and electrifying sectors such as transportation and buildings [2]. Undoubtedly, in order to reduce the carbon footprint, several alternatives should be employed, such as solar [3] and wind [4] power, as well as fuel cell [5,6] technologies.
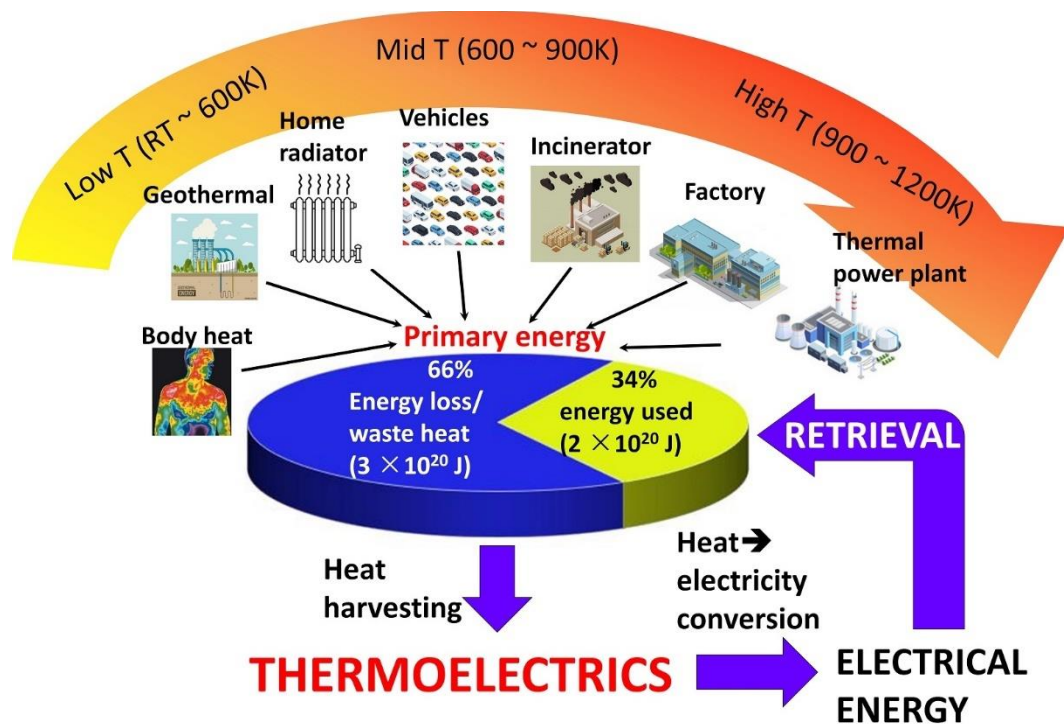

Figure 1 - Sketch of the role of thermoelectrics (TE) in the recovery of electrical energy from various sources of waste heat at increasing operating temperature.

There are huge waste heat sources in our environments covering a wide range of temperatures (300~1200 K): industrial processes, domestic stoves and radiators, lighting, pipelines, electrical substations, subway networks, automotive exhaust tubes, but also geothermal heat, body heat, and so on: about 66 % of the of annual world energy consumption is lost as waste heat, and the loss corresponds to the stellar amount of $3 \cdot 10^{20}$ J per year, just considering the past 10 years [7,8]. A highly promising method for energy recovery from such heat sources is the utilization of thermoelectric (TE) materials that can convert various types of waste heat flows into electricity.

Energy harvesting, in this regard, representing the energy derived from ambient sources directly converted into electrical energy, can be one solution to increase the sustainability of energetic usage. In this scenario, thermoelectricity is a promising and attractive property of materials that could play a notable role in the future global requirement of energy due to its dual function in power generation and refrigeration. Thermoelectric generators (TEGs) are able to recover wasted thermal energy and convert it into useful electrical energy. They provide a route for energy saving and improving systems efficiency, without using fossil fuels, leading to a reduction of greenhouse gas emissions (Figure 1). Thermoelectric generators work based on the thermoelectric effect and it relies on the possibility to create a difference of potential, and thus electricity, directly when the device undergoes a difference of temperature between its two sides. At the atomic scale, an applied temperature gradient stimulates the diffusion of charge carriers through the material starting from the hot side to the cold one.
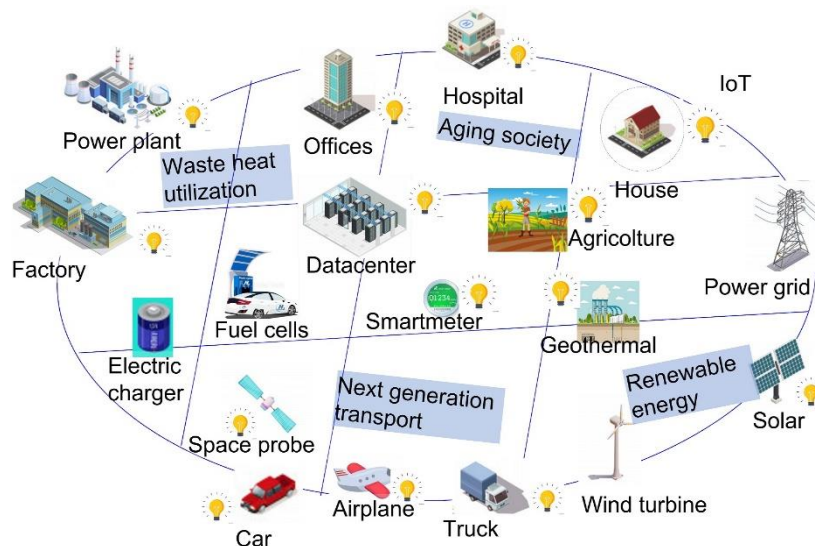

Figure 2 - Ubiquitous employment of waste heat recycling by thermoelectrics in future society. Locations where thermoelectric harvesting is feasible are marked with 💡.

The extensive adoption of highly efficient and sustainable novel TE materials and harvesters based on them would be hugely beneficial for society, realizing the improvement of energy efficiency, the reduction of the overall CO_2 emissions, the extensive adoption of battery- and electric-grid free devices and sensors for IoT, the implementation of wearable electronics, and so on (Figure 2).To realize that we need efficient TEs working at different temperature regions depending on the waste heat source. They can be employed for a wide spectrum of purposes, for example as radioisotope heat sources for space applications, or as power supplies in remote areas, or in the automotive field [9,10].

Besides the commendable environmental aspect, many other advantages come with these generators, such as little to no maintenance required, zero emissions of harmful gases while operating, the absence of moving parts and a long-life span, quiet, silent, and also, they are usefully scalable, making them ideal for different power levels when necessary [11,12,13].

2021 marks the 200-anniversary of the discovery of the Seebeck effect by Thomas Johann Seebeck [14]. The TE performance of a material is expressed by means of the concept of the figure of merit, Z, defined by E. Altenkirch at the beginning of the XX century [15]. Seeing that Z differs with absolute temperature T, an advantageous way to display the efficiency is the non-dimensional figure-of-merit ZT. Commonly, ZT values of both the n-type and p-type TE materials contribute to the definition of the efficiency of a TE device. In order to have high
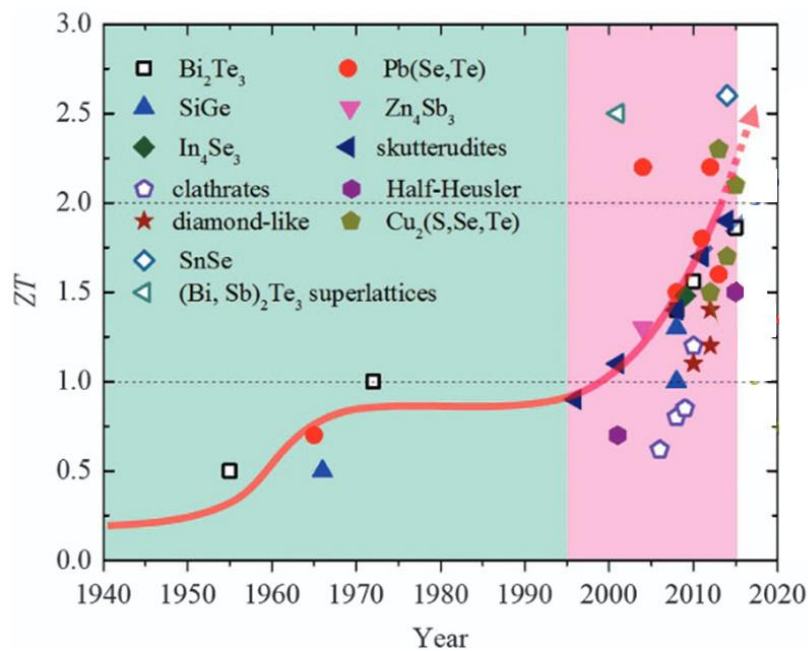

Figure 3 - The chronological evolution of ZT values in various thermoelectric materials. Adapted from [17].

efficiency, high *ZT*s are required. For this reason, modern research efforts are focusing on developing strategies leading to materials with high *ZT* [16,17].

The discovery of the thermoelectric effect was made on the junction of metallic materials. For this reason, this effect was ignored in the pioneering period of the discovery because of the very low efficiency of the metals: most of them possess a generating efficiency much lower than the 1%, making them an inefficient resource of electrical power. Consequently, the only possible practical application of the TE effect at that time was to take advantage of the slight difference of potential created in order to measure the temperature, the familiar thermocouple [18]. An improved attraction in thermoelectricity arose in the late 1930s thanks to the development of synthetic semiconductors with a much higher TE performance than metallic materials. Nevertheless, the complex parameter mutuality makes the tactic of tuning carrier concentration alone inefficient for enhancing *ZT*. The highest *ZT* of TE materials had values below 1 for a protracted period of time, and the TE devices ran at a low power conversion efficiency close to ~2 %.

As displayed in Figure 3, which summarizes the reported *ZT* values per publishing year, no considerable improvements have been done between the early 1970s and the late 1990s and the TE technique was ineffective and not cost-effective for most applications. Great advancements have been made in the TE field after the 1990s, especially thanks to newly developed strategies to improve the power factor and to lower the thermal conductivity, and so boosting *ZT*, particularly with an independent control of the lattice thermal conductivity. In this sense, the most common technique consists in the introduction of scattering centres, for instance through density enhancement [19], porosity control [20], nanostructuring [21], mesostructuring [22], or precipitation of nano-sized secondary phases [23]. A further method, consisting of the introduction of substitutional and/or interstitial atoms, underlies the optimization of skutterudites. This strategy can result in *ZT* being pushed to over 1.5, leading to a power conversion efficiency that can be considered equal to 11 % - 15 %. Various novel approaches and new technologies have pushed *ZT* to over 2.5 [24,25] in recent years driving to a conversion efficiency close to 20 %. Although significant advancements have been made in recent years at the laboratory scale, the performance of a thermoelectric energy converter remains moderate if compared to conventional processes. Several materials have been studied in the last century with the aim of finding new compounds able to have high efficiency of conversion with reduced cost. New goals in the TE field are now based on the choice of affordable, abundant and low

toxic materials, all linked with the final target of obtaining high efficiencies with *ZT* over 2.0.

The figure of merit, which will be introduced more in detail in Section 2.3.3, is directly proportional to the so-called power factor $S^2\sigma$, and inversely proportional to the thermal conductivity κ. The PGEC (Phonon Glass Electron Crystal) concept [26] rules the search for materials with high thermoelectric properties. The manipulation of σ and S aimed at the enhancement of the power factor, with the intention to improve the figure of merit *ZT* usually requires a deep knowledge of the band structure of the material and its proper tuning is a challenging approach. Yet, the most commonly pursued phenomenological approach directed toward the search for good thermoelectric materials consists in the depression of thermal conductivity through the reduction of the phonon mean free path, which can be accomplished by introducing into the void of the hosting structure an ion of proper size, disturbing the transmission of vibration quanta through its rattling movement. In this framework, Heusler [27, 28] and half-Heusler phases [29], clathrates [30,31] and filled skutterudites [32, 33] are currently studied as promising thermoelectrics among intermetallic materials. Furthermore, filled skutterudites play a relevant role due to the possibility to obtain *n*- and *p*-conducting materials just by changing the doping ions amount [34].

Skutterudites MX_3 [32,35] (M ≡ transition metal, X ≡ pnictogen atom) crystallize in a body-centred cubic cell. Such material is characterized by a too high value of κ to be exploited for thermoelectric applications [36], but if a proper R atom (R ≡ rare earth or alkaline-earth element) enters the cavity of the structure, the phononic or lattice term of the thermal conductivity κ_{ph} is significantly lowered thanks to the vibrational modes of the vibrating guest, which hinder the propagation of heat-carrying phonons [37], and *ZT* is enhanced. In this respect, filled skutterudites RM_4X_{12} follow the Phonon Glass Electron Crystal (PGEC) concept [38] and some examples of high-quality outcomes are the *n*-type $(Sr,Ba,Yb)Co_4Sb_{12}$ with $ZT \approx$ 2.0 at 835 K [39] and the *p*-type $DD_{0.7}Fe_3CoSb_{12}$ with $ZT > 1.3$ at 856 K [40]. In the majority of filled skutterudite systems, both *p*- and *n*-type compounds can be synthesized from the same parent compound by tuning the filling ratio of the R atom and the partial substitution of M atom, thus originating a lot of different compounds, such as Fe/Ni- [41,42] and Fe/Co- [43,44] based ones. At the same time, the insertion of two different M atoms, similarly to the doping by two different rare earths [41] or the partial substitution of Sb by Sn [45] or Ge [46], is responsible for the creation of additional scattering centres, thus for a further lowering of κ_{ph}. The effect of low dimensionality and the presence of interfaces, moreover, make thin films particularly

interesting as a source of further phonon scattering [47,48]. Nevertheless, in spite of the relevance of this issue, very few literature works are devoted to the deposition of skutterudite thin films and to their characterization, and almost all of them deal with $CoSb_3$ [49,50] and $CoSb_3$-derived compounds [47,51,52].

Oxides have been recognised as respectable candidates for concrete use as TE materials, especially due to their stability at high relative humidity and high temperature. Moreover, they are reasonably priced and environmentally friendly compared to inter-metallic materials. Consequently, many efforts of modern research are focused on the fabrication of stable, eco-friendly, abundant and cost-effective TE materials based on bulk oxides materials. Yet, the best reachable figure of merit of the available oxide materials at this time at high temperature (1000 °C) are still lower than 1: $ZT \sim 0.64$ for *n*-type observed by Ohtaki et.al [53] and 0.74 for *p*-type by Saini et.al [54]. Most of the reports available in literature regard bulk oxides, which depict some main disadvantages such as the laborious and timewasting sintering and shaping processes required to fabricate the *n*-type and *p*-type elements, contact resistance of pillars in fabricated modules, not even mentioning the mechanical fragility. On the other hand, oxide thin films offer substantial advantages compared to bulk oxide materials, for instance, quick fabrication, flexibility and control of defects at the nano-scale range.

Many oxide thin films such as CdO, ZnO, SnO_2, TiO_2, etc, are available for various device fabrications. Though, ZnO thin film can reveal a better thermoelectric behaviour than other oxide films due to its superior environmental and thermal stability, up to 2000 °C. Zinc Oxide (ZnO) is a notorious *n*-type semiconducting metal oxide, and it possesses a pronounced bandgap (~3.36 eV) with high binding energy (~60 meV). Lately, Al-doped ZnO (AZO) thin films have been specially found to possess a higher ZT value than the corresponding bulk materials, attributable to the effect of natural nano-defects (dislocations, grain boundaries) [55,56]. Besides, an additional positive advantage of this material is given by the fact that the Al^{3+} doping distributes donor electrons to the Zn^{2+} sites consequently increasing film carrier concentration with a resulting enhancement of the electrical conductivity. Although, the thermal conductivity could be diminished by enhancing the phonon scattering given by grain boundaries and nano-precipitates in Al-doped ZnO structure [57].

In recent years, the necessity for employing micro-TE devices as a substitute power source for small electric devices and systems is increasing and the research in the micro-TE device is attracting more and more attention. Conventional TE device production methods are

not adequate for such miniaturized devices, and, for this reason, small apparatuses based on thin films are one of the most extensively studied research topics for this purpose. TE thin films could be an amazing power source as TEG for wearable [58] or biomedical devices [59] or coolers as TEC for microchip applications [60]. Nanostructuration is a typical property of thin films, which lead to a positive enhancement of TE characteristics of a material. Low dimensional thermoelectric materials, such as thin films, are considered a revolutionary way to decouple electrical and thermal transport properties, enhancing the overall TE efficiency [61].

To this purpose, my PhD project is focused on the synthesis and characterization of TE thin films using a pulsed laser deposition (PLD) technique. The reason for choosing thin films is that their intrinsic properties offer significant advantages for developing TE: flexibility, low dimensionality, rapid fabrication, control of strain at the interface with substrates. This project is focused on the synthesis and characterization of thin films of skutterudites and oxides.

2 THERMOELECTRICITY

Thermoelectricity is one of the oldest phenomena to be observed in semiconductors, with the discovery of the various thermoelectric effects dating back to the early part of the 19th century. These effects manifest themselves as the appearance of a voltage in a circuit comprised of two different conductors due to a temperature difference (Seebeck effect) or as the absorption and evolution of heat at the junction of two different materials under electrical current excitation (Peltier effect). These effects can be utilized in devices to generate electrical power from waste heat or to provide solid-state cooling, respectively (Figure 4). In particular, electricity can be generated by applying a thermal gradient, and then utilize in those fields where there is a considerable waste of heat (i.e. industry, photovoltaic, motor vehicles), or else, obtain a cooling effect by simply applying a voltage.

Thermoelectric effects involve the electronic and thermal properties of a system through mutual influence. In general, all materials show thermoelectric properties, although in most cases these are absolutely irrelevant phenomena. Few compounds, however, can be considered promising thermoelectric materials. The latter are characterized by a strong difference between the values of electrical and thermal conductivity, as well as a high Seebeck coefficient.
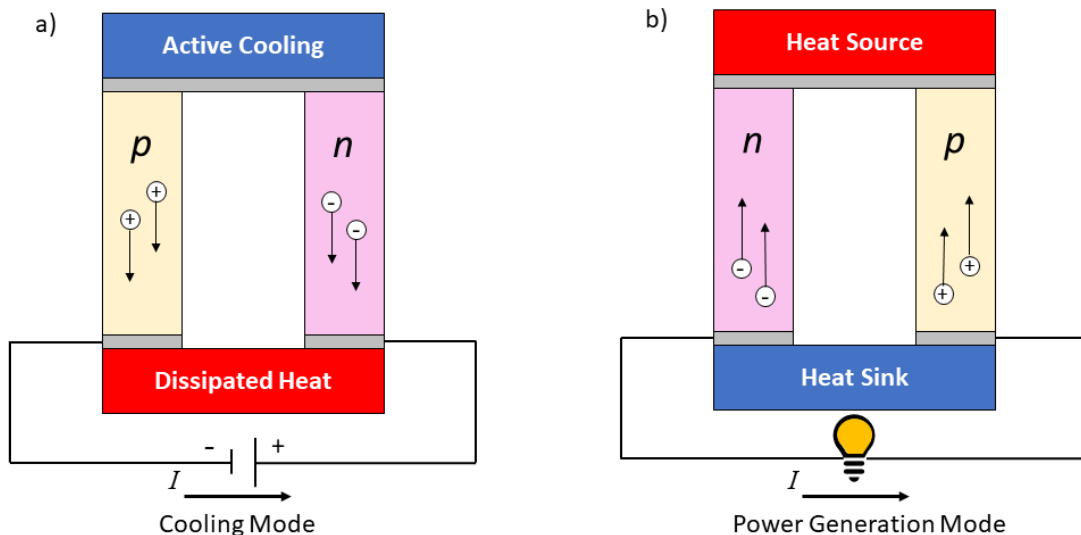

Figure 4 - a) Example of a cooling device mode, b) and a power generation device mode.

2.1   Seebeck Effect and Seebeck Coefficient

Thermoelectric effects allow direct conversion of heat into electricity and vice versa. The first of the effects to be rationalized was the Seebeck effect, discovered in 1821 by the German physicist Thomas Seebeck (1770-1831) [62]. Seebeck discovered that a circuit made of different metals, with junctions placed at two different temperatures, deflects a magnetic needle. However, the Danish physicist Hans Christian Ørsted subsequently realized that the temperature difference produces a voltage that allows the passage of an electrical current, causing the deflection of the needle because of the Ampere law [14].

The Seebeck effect is the development of an electromotive force (EMF) across a material in response to the application of a temperature differential in dissimilar electrical conductors or semiconductors and the magnitude of the produced EFM massively differs depending on the nature of the material. It is a bulk property and does not depend on either the specific arrangement of the leads or the material or the specific method of joining them. In open-circuit conditions, the electromotive force can be measured as a potential difference ΔV, which is proportional to the thermal gradient ΔT through the following equation [63]:

$$\Delta V = S\Delta T \tag{1}$$

which can also be written as:

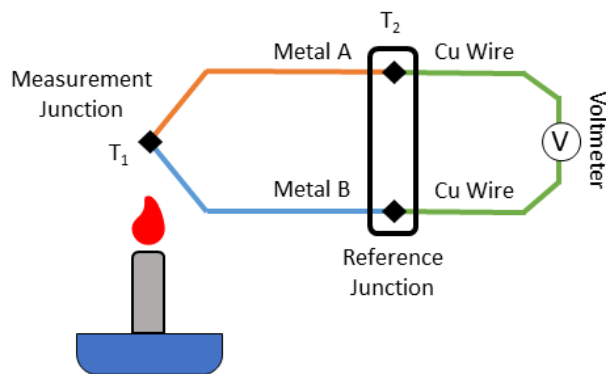$$S = \frac{\Delta V}{\Delta T} \tag{2}$$

Figure 5 - A scheme representing a thermocouple principle.

where S is the Seebeck coefficient and it is expressed in units of volts per Kelvin (V/K), although it is more often given in microvolts per kelvin (μV/K), and it gauges the magnitude of this effect.

The Seebeck effect is at the base of the functioning of thermocouples, where the S is used to measure temperatures, and for increasing accuracy, it is desirable to use materials with a Seebeck coefficient that is stable over time. They are constituted by two wires of two dissimilar metals, coupled at one end, called the measurement junction (usually the hot one). The junction is put at the measuring temperature, while the other ends (of the wires that are not physically in contact) are kept at a constant and precisely known temperature and attached to the voltmeter. The junction between the two thermocouple wires and the copper traces is called reference junction (usually the cold one). When the measurement junction is heated, a potential is created within the wires and detected by the voltmeter (Figure 5). Such voltage is proportional to the temperature difference between the hot and the cold junctions, as in Equation 1. In view of the fact that the thermocouple is a differential device, it is essential to know the reference junction temperature to get an accurate absolute temperature evaluation. The resulting Seebeck coefficient is the difference between the Seebeck coefficients of the two materials, S_A and S_B. If the measuring temperature range is narrow enough, the Seebeck coefficients can be considered constant and the relationship between ΔV and ΔT is approximated to the following equation:

$$\Delta V = (S_A - S_B)(T_1 - T_2) \tag{3}$$

All materials have a non-zero value for S. Generally, good conductors such as metals have a small value for Seebeck, while poor conductors such as insulators have a large value. The Seebeck coefficient depends upon temperature, vanishing at the absolute zero $T = 0$ K, and it is the entropy of the charge carriers divided by the electrical charge [64].

The coefficient measures the entropy per carrier, and its magnitude is related to the average energy at which the current flows (E_J) with respect to the Fermi level energy (E_F) [72]. In the case of metals, the Fermi level is deep within the conduction band, so, the energy of the states carrying current and the Fermi energy are very similar, leading to a low Seebeck coefficient. However, for semiconductors, the Fermi level is quite distant from the energy at which the current flows, resulting in a high magnitude of the Seebeck coefficient. For heavily doped semiconductors the value of the Seebeck coefficient diminishes. The sign of the

coefficient depends on the type of the majority carriers, a negative and a positive Seebeck coefficient is found for, respectively, *n*-type and *p*-type semiconductors.

Conventionally, the crossover from the *p*- to the *n*-conduction regime occurs at the composition where the Seebeck coefficient changes its sign. Nevertheless, it has to be considered that in the crossover region the Seebeck coefficient of a multiband semiconductor, such as the present one, is characterized by a complex dependence on two factors originating from both holes and electrons, according to the following expression [26]:

$$S = \frac{\sum_i \sigma_i S_i}{\sum_i \sigma_i} = \frac{n_e \mu_e S_e + n_h \mu_h S_h}{n_e \mu_e + n_h \mu_h} \qquad (4)$$

being *S*, S_e and S_h the overall, electron and hole Seebeck coefficient, respectively, σ the electrical conductivity, n_e and n_h the negative and positive charge carriers, respectively, and μ_e and μ_h the mobility of electrons and holes, respectively. This means that not only the charge carrier amount but also the carrier mobility contributes to *S*, which in principle does not allow to easily locate the position of the *p/n* crossover. On the other hand, the Seebeck coefficient is inversely proportional to the number of charge carriers, as described by the following equation [12]:

$$S = \frac{\pi^2 \, k_B^2 \, 2 \, m^*}{|e| \hbar^2 (3n\pi^2)^{2/3}} T \qquad (5)$$

where m^* is the effective mass and *n* the number of charge carriers. For this reason, the *p/n* crossover is generally identified at the composition where the Seebeck coefficient assumes the maximum value.

2.2 Peltier Effect

In 1834, a French watchmaker and physicist, Jean Charles Athanase Peltier, discovered that the passage of an electric current produces heating or cooling at the junction of two different metals.

Peltier effect, therefore, implies a difference in temperature between the ends of different jointed conductive materials, when they are crossed by a current flow: one junction produces thermal energy and the other one absorbs it. The amount of generated or absorbed thermal energy is proportional to the current I which flows through the circuit up to a proportionality constant, said Peltier coefficient, and indicated by the symbol Π. This represents the amount of thermal energy that flows per unit of charge through a given material. The heat absorbed per unit of time $\dot{Q}$ is equal to:

$$\dot{Q} = \Pi_{AB} I = (\Pi_A - \Pi_B) I \tag{6}$$

where Π_{AB} is the Peltier coefficient for materials A and B, which varies with the temperature and nature of the material and I is the applied current.

2.3 Thermoelectric Parameters and Performance

The thermoelectric performance of a generator or a cooling system depends on the configuration of the module, the quality of connections, the temperature gradient across the module and the thermoelectric properties of the material, *i.e.,* electrical and thermal conductivity, and Seebeck coefficient, which has been described in the previous section [65].

2.3.1 Electrical Conductivity

The electrical conductivity (σ, $[\Omega^{-1}m^{-1}]$) measures the ability of a material to conduct electric current and it is described by the following equation:

$$\sigma = ne\mu \tag{7}$$

where n is the carrier concentration, e is the electron charge and μ is the mobility of carriers. Electrical conductivity strongly depends on the nature of the conductor and temperature. In the case of metals, the carriers' concentration remains pretty much constant upon changing the temperature, however, the mobility of carriers diminishes because of the reduced electronic mean free path, as a result of interactions with thermal vibrations. For semiconductors, the electrical resistivity of which falls in an intermediate-range between insulators and metals, the conductivity increases with temperature because of the promotion of carriers into the conduction band; this event enhances the carriers' concentration and rules over the phonon-electron scattering, thus σ increases. Since thermoelectrics often belong to the latter category, their efficiency increases with rising temperature.

σ is related to resistivity ρ through the relationship:

$$\sigma = \frac{1}{\rho} \tag{8}$$

The main problem in measuring the electrical resistance of the materials is associated with the thermoelectric effects that are always present unless isothermal conditions are maintained. If there is a temperature difference between the two ends, this will give rise to a Seebeck voltage that augments or opposes the resistive voltage. The flow of current causes a

temperature difference to be established by means of the Peltier effect, but the problem may be overcome simply by inverting the current flow. When the current is reversed, the Peltier heating and cooling are also switched and there is an increase in the potential difference above the resistive value whichever way the current flows. This effect may be used in determining the thermoelectric figure of merit but, when only the electrical conductivity is of interest, it is a source of error that has to be eliminated.

2.3.2   Thermal Conductivity

The thermal conductivity (κ, [W/m·K]) is the ability of a substance to transfer energy, in the form of heat, when it is subjected to a temperature gradient. The conductivity is given by the sum of different contributions, reducible to the two most relevant terms:

$$\kappa = \kappa_e + \kappa_{ph} \tag{9}$$

where κ_e is the electronic contribution due to the transport of thermal energy by electrons and vacancies, and κ_{ph} is the phonon contribution, due to the transport of thermal energy by phonons through the crystal lattice [63].

The electronic component is related to the electrical conductivity through the Wiedemann-Franz law:

$$\kappa_e = L_0 \sigma T \tag{10}$$

where L_0 is the Lorenz number (2.45 x 10^{-8} W/S·K^2), σ is the electronic conductivity and T is the temperature. The constraint given by Equation 8 prevents the independent manipulation of the two conductivities, thermal and electrical, making it impossible to minimize κ_e and maximize σ at the same time. Thus, one possible strategy to minimize κ is to work on the phonon-lattice component κ_{ph} [66]:

$$\kappa_{ph} = \frac{1}{3} C_v v \Lambda \tag{11}$$

where C_v is the specific heat at constant volume, v the sound velocity, and Λ the phonon mean free path. The phonon component κ_{ph} is due to the atomic vibrations about their equilibrium positions, named phonons, that propagate within the solid as acoustic waves when

the material is subjected to a temperature gradient. Unlike κ_e, the contribution of the phonons to thermal conduction does not depend on the electronic properties of the material, hence, it can be separately manipulated.

2.3.3 Figure of Merit and Efficiency

The efficiency of a thermoelectric device depends only on the properties of the material and it is linked to these through the figure of merit Z [67]:

$$Z = \frac{S^2\,\sigma}{\kappa} \tag{12}$$

where S is the Seebeck coefficient, σ the electrical conductivity and κ the thermal conductivity. Because the figure of merit varies with temperature, a more meaningful measure of performance is the dimensionless figure of merit ZT (where T is the absolute temperature):

$$ZT = \frac{S^2\,\sigma}{\kappa}T \tag{13}$$

The larger is the value of ZT, the higher is the efficiency of the TE generator or cooler. Conventionally, it is assumed that to be applicable a thermoelectric material should possess a $ZT = 1$ or higher. The $S^2\sigma$ quantity, known as power factor (PF), is also used to express the efficiency if no thermal conductivity measurements are available. A large PF means that a large voltage and a high current are generated. During the last decades, new materials have been developed to increase ZT, though it is not an easy task, since S, σ and κ show a strong interdependence [68].

The efficiency of a thermoelectric device depends on factors other than the maximum ZT of a material, primarily due to the temperature dependence of all the materials properties, such as S, σ and κ, that make up $ZT(T)$.

For a Peltier cooler, the device ZT is most straightforwardly measured from the maximum temperature drop obtained (ΔT_{max}).

$$\Delta T_{max} = \frac{ZT_c^2}{2} \tag{14}$$

For a TE generator, besides the material performance, the maximum power-generation efficiency is thermodynamically limited by the Carnot efficiency ($\Delta T/T_H$) (black solid line in Figure 6). Since TE devices are indeed thermal engines, their efficiency (η) is related to the difference in temperature between the hot and cold end, through the following equation:

$$\eta = \frac{T_H - T_C}{T_H} \frac{\sqrt{1 + ZT} - 1}{\sqrt{1 - ZT} + \frac{T_C}{T_H}} \tag{15}$$

where T_H and T_C are the hot and cold temperatures, respectively. In order to maximize the efficiency, it is imperative to maximize the device ZT or ($T_H - T_C$) [12].
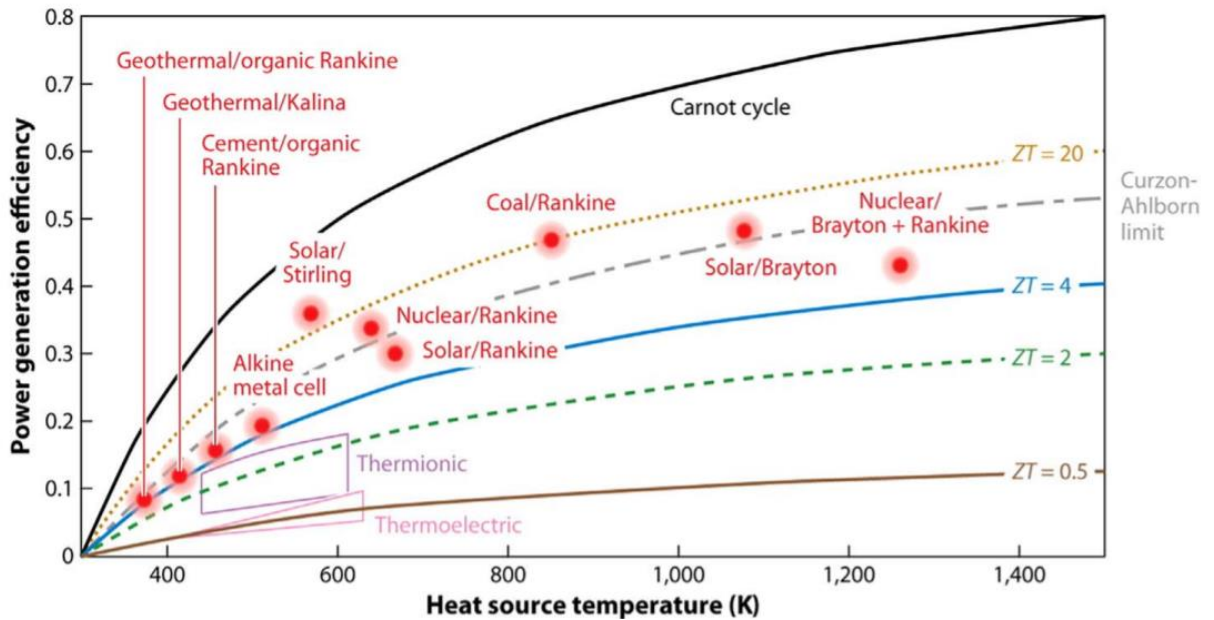
Figure 6 - The efficiency comparison of thermoelectrics and other energy-conversion technologies as a function of the heat-source temperature. The ZT values are assumed to be temperature independent, and the heat-sink temperature is set at room temperature. Reproduced from [16].

2.3.4 Strategies to Improve *ZT*

Therefore, the challenge, in order to improve the materials' performance, is to create high *ZT* thermoelectric materials and, as aforementioned, it lies in achieving simultaneously high electronic conductivity, high thermoelectric power and low thermal conductivity in the same solid. Concerning the charge carriers' contribution, these parameters are determined by the details of the electronic structure; since both the electrical and the electron-thermal

conductivity depend on conducting electrons, they are not independently controllable (Equation 10).

Following Equation 11, it is apparent that if Λ is reduced, also κ_{ph} will decrease and eventually ZT can be improved. This approach can be realized by the effect of natural nanodefects, like grain boundaries, interstitial atoms, dislocations etc., or introducing nanostructured defects into the material as schematically represented in Figure 7.
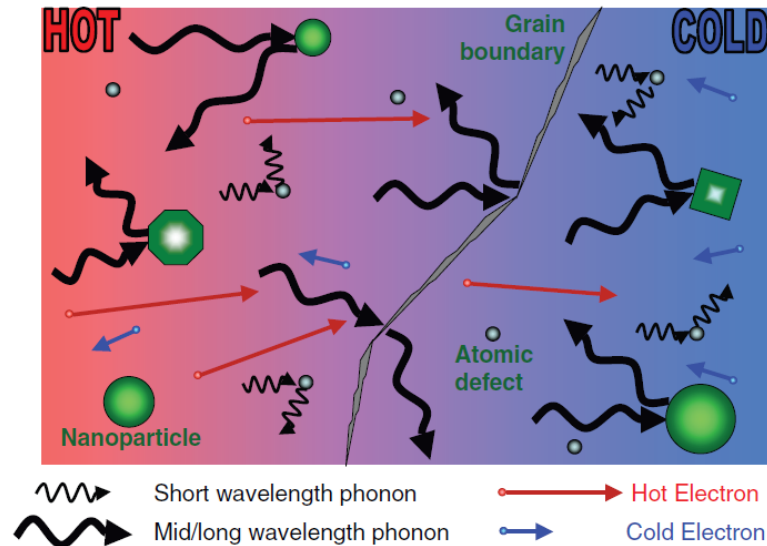

Figure 7 - Effect of nanodefects on the phonon movement in a thermoelectric material [69].

In more detail, a recent widespread strategy exploited to reduce the phonon contribution to thermal conductivity is the introduction of filler atoms in materials with free interstitial sites: skutterudites and inorganic clathrates are included in this class of materials. Hence, with the aim of increasing ZT, κ_{ph} can be reduced using sufficiently small atoms that oscillate locally at a frequency that interferes with the phonon transmission, thus creating dynamic disorder while not disturbing the electronic transport. The ideal thermoelectric material can therefore be considered as a crystal in which the high mobility electrons are free to carry charge and heat, but the transport of the latter by phonons is interrupted at the atomic scale. Combining the filling of the voids with appropriate doping of the lattice, an optimal result can be reached, consisting of a strong increase of σ and S, and a significant reduction of κ_{ph}.

Attempts are also being made to improve the competitiveness of thermoelectric material in directions other than the improvement of the figure of merit. Efforts have focused for example on decreasing cost, and developing environmentally friendly materials.
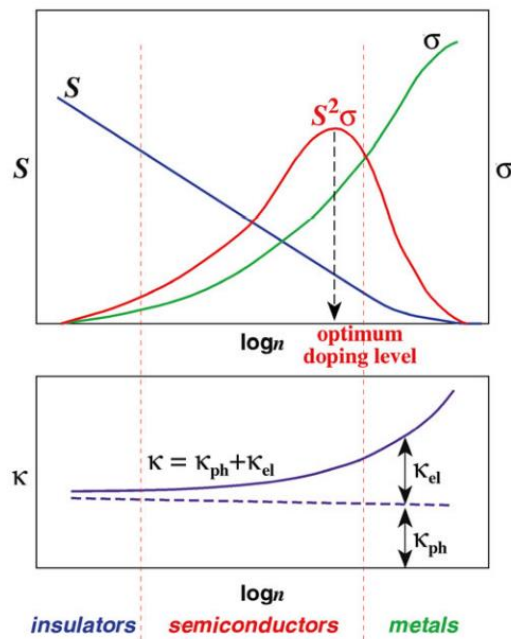
Maximizing the efficiency of a thermoelectric involves a compromise of thermal conductivity and Seebeck coefficient with electrical conductivity.

Taking into account these requirements, the most efficient thermoelectric materials can be found among semiconductors for two main reasons:

1. Differently from metals, they show an increasing electric conductivity with increasing temperature, and the *PF* has a maximum within the carrier density range proper of semiconductors, as summarized in Figure 8. Good thermoelectric materials are typically heavily doped semiconductors with a carrier concentration between 10^{19} and 10^{21} carriers per cm^3. The thermoelectric Power Factor maximizes at higher carrier concentration than *ZT*;

2. In semiconductors, κ_{ph} prevails over κ_{el} so that it is possible to separately act on thermal and electric conductivity. In this respect, filled skutterudites represent an example of easily tuneable thermoelectric materials.

Figure 8 - Maximizing the efficiency of a thermoelectric involves a compromise of thermal conductivity and Seebeck coefficient with electrical conductivity [70].

2.3.4.1   Strategies to increase the Power Factor

As already mentioned before, semiconductors make up the best candidates for thermoelectric applications because of their high power factor, resulting from both a high Seebeck coefficient and high electrical conductivity.

However, the thermoelectric properties can be further improved by tuning the carrier concentration with doping. Generally, the behaviour of S and σ upon changing carrier concentration is opposite, meaning that the Seebeck coefficient will decrease, and electrical conductivity will increase with the enhancement of the carrier concentration. The maximum value for power factor is found for a high content of dopant, ranging between 10^{19} and 10^{21} carriers per cm^3 [66].

The semiconducting regime covers a wide range of values of carrier concentration and the boundary between other regimes (insulating and metallic) is not strictly delimited. The electrical conduction only occurs thanks to the movement of electrons between different energy states; this means that conduction will not happen for an empty or completely filled band, whereas no electrons are present or no available states for the electron to occupy are present, respectively. For a metal, electrons are located in a partially empty band, so that they can freely move between other states inside the band. For an insulator, electrons are located in a filled band and have no possibility to be promoted into other bands, due to the large energy gap. For an intrinsic semiconductor, electrons are positioned in a filled band, named valence band, but the energy gap is small enough to be overcome so that the electrons can be promoted into an empty band, named conduction band, and contribute to electrical conduction (Figure 9). The number of electrons that possess enough energy to enter the conduction band is a function of temperature. In addition, the holes left behind by the transitioned electrons also contribute to conduction. Nonetheless, at the working temperatures of a TE device, the electrical conductivity is still too small. However, it can be improved by inserting (doping) in the structure donor or accepting atoms, that increase the number of electrons in the conduction band (*n*-type) or holes in the valence band (*p*-type), respectively (Figure 9). The materials resulting from the doping process are extrinsic semiconductors.
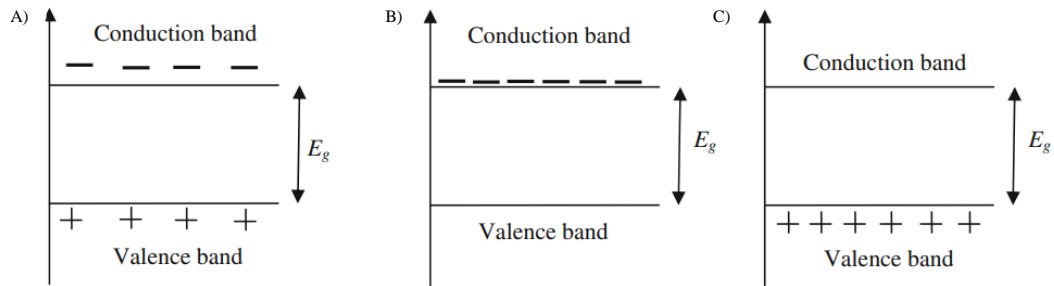
Figure 9 - Schematic energy diagrams for an intrinsic semiconductor (A), an n-type semiconductor (B) and p-type semiconductor (C) [71].

Despite the use of doped semiconductors being the right strategy to increase the power factor, since the optimum combination of electrical conductivity and Seebeck coefficient is achieved only for these materials, with the advancements of research it was found that further optimization is possible by tuning the electronic structure of the bands. As a matter of fact, it was discovered that the more complex is the band structure near the Fermi level, the larger is the produced power factor. Electronic-bands complexity is intuitively achieved by synthesizing compounds with complex structures and compositions, like skutterudites. In Figure 10, the hypothetical band structures for a simple and a complex semiconductor are reported. The terms E_F and E_F' refer to the energy of the Fermi levels for an intrinsic and an *n*-doped semiconductor, respectively.
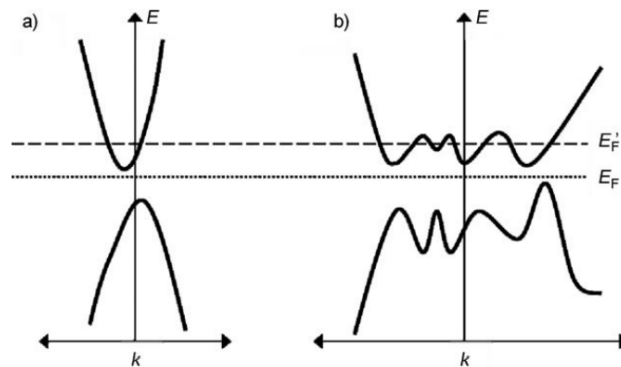
Figure 10 - Hypothetical band structures of a simple semiconductor (a) and of a multiband semiconductor (b) [72].

21

2.3.4.2   Strategies to reduce the thermal conductivity

The constraint given the Wiedemann-Franz law (Equation 10), which directly correlates the electronic component of κ to the σ, prevents the independent manipulation of the two conductivities, making it impossible to minimize κ_e and maximize σ at the same time.

Anyway, phonons carry most of the heat and the total thermal conductivity is given by the contribution of a spectrum of wavelengths and mean free paths (MFP), described as the distance travelled by phonons between two scattering events. As described in Equation 11, κ_{ph} is proportional to the heat capacity C_v (approximately constant), to the phonons' velocity v and to the MFP length Λ. When the dimensions of inclusions or defects are comparable to the MFP, phonons with that particular Λ will be scattered. As a consequence of the aforementioned statement, structures that contain all-scale hierarchical heterogeneities on multiple length scales (from nano- to micro) are highly desired to potentially reduce the thermal conductivity and improve *ZT*. This panoscopic (multiscale) approach is summarized in Figure 11 and it was successfully experimentally applied by Kanatzidis et al. [69] on PbTe.
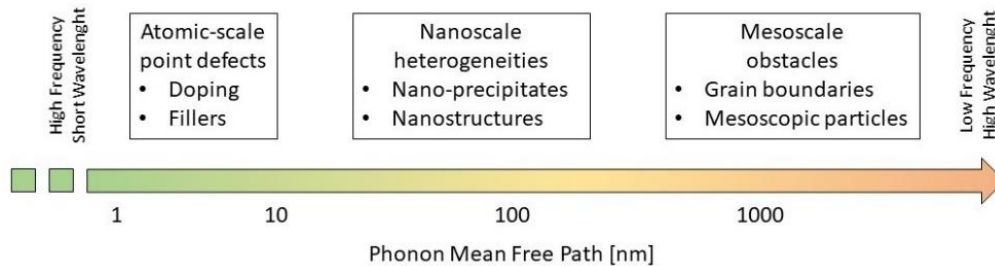

Figure 11 - Panoscopic (multiscale) approach to TE materials to reduce κ_{ph} at different MFPs.

The intent of minimizing the free path is achieved by increasing the number of scattering effects, but many strategies can be employed to aim at this goal. For example, the insertion of impurities, defects, grain boundaries and crystal imperfections within the structure has proved to successfully disrupt the phonons propagation, because of the scattering caused by the interaction between the phonon and change in mass of the defect [73]. Another strategy is to synthesize materials with complex structures, that include loosely bound atoms, whose anharmonic oscillation interfere with the phonons travel. This strategy is successfully employed in filled skutterudites. Finally, another novel approach is to exploit low-dimensional systems, like thin films or nanostructured materials, to further suppress the thermal conductivity [41,66].
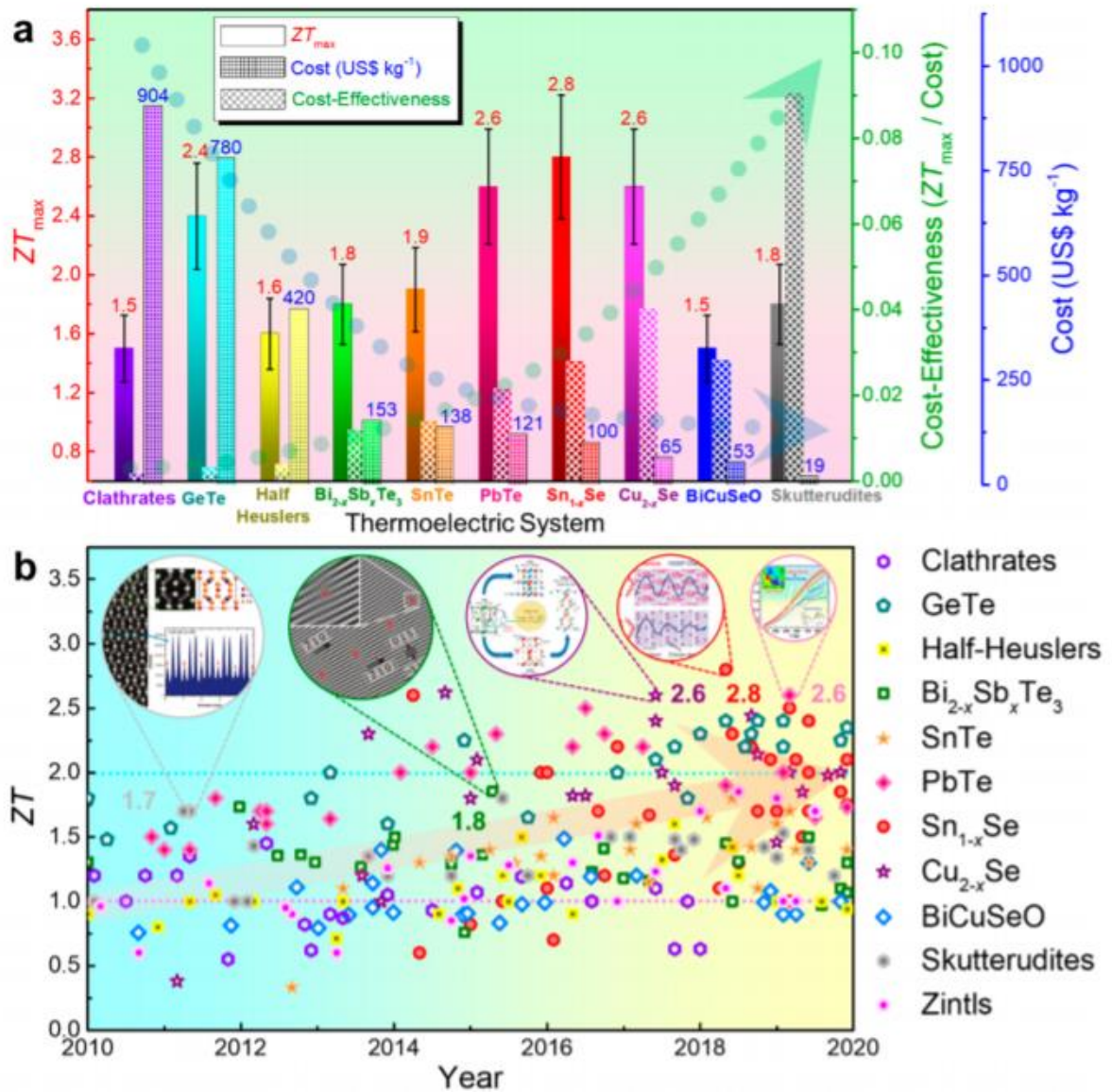
Figure 12 - ZT values for state-of-the-art thermoelectric materials in the last 10 years. (a) Reported maximum ZT values (ZT_{max}) with error bars, calculated cost, and calculated cost-effectiveness (ZT_{max}/cost), and (b) timeline for the state-of-the-art thermoelectric materials (bulks), including $Bi_{2-x}Sb_xTe_3$ (BST), BiCuSeO, clathrates, $Cu_{2-x}Se$, GeTe, half-Heuslers, $Sn_{1-x}Se$, PbTe, skutterudites, SnTe, and Zintls [74].

Thanks to the new material's design routes, noticeable progress was made in term of efficiency, almost doubling *ZT* values in the past 10 years (Figure 12). Zhang et al. [75] reported *ZT* for nanowires of Bi_2Te_3 up to 2.5 at 350 K. The carbon-reinforced Cu_2Se exhibits an ultra-high thermoelectric figure of merit of 2.44 at 870 K [76]. Xu et al. [77] present a *ZT* value close to 2.4 at 773 K for *p*-type pseudo-layered $Sb_2Te_3(GeTe)_{17}$ by synergistically optimizing its TE properties via vacancy engineering.

Regarding skutterudites, nice improvements are reported by Zhou et al [78], who published about a maximum figure of merit of 1.42 at 850 K with also greatly improved mechanical properties for Yb-filled Co- based skutterudite with ultrafine dispersed SiC. One of the most promising skutterudites is presented by Rogl et al. [79] with a high power factor (4.4 mW/m·K^{-2} at 730 K) and a very low thermal conductivity leading to a remarkable high $ZT = 1.8$ at 823 K for an In,Sr,Ba,Yb-filled CoSb$_3$.

Oxide-based thermoelectric materials generally exhibit an inferior ZT compared to the aforementioned materials. Regarding a p-type oxide, a record ZT of 0.74 at 800 K was observed for Tb doped Ca$_3$Co$_4$O$_9$ by Saini et al [54], while for n-type materials, a figure of merit 0.44 at 1000 K was found for Al-Doped Zinc Oxide Nanocomposites [80].

2.4 Thermoelectric Materials

The use of a given material is strictly bounded to the availability of raw materials and the relative environmental repercussions during the extraction, processing, operational and disposal phases. In addition, some materials with high ZT are made of elements that are not only rare in the Earth crust (such as tellurium) but also quite expensive. A wide variety of new thermoelectric materials have been developed during the last years, aiming at the common goal of reaching high ZT values. Historically, the search for thermoelectric materials started with simple metals, then conventional semiconductors and group V tellurides were approached (e.g., SiGe, InSb, Bi_2Te_3), arriving at the relatively newly developed materials, such as half-Heusler compounds, clathrates and skutterudites for the intermetallics' family and oxides for the ceramics counterpart, also, in the last ten years, organic thermoelectric made their appearance, showing good, yet improvable, TE qualities. A brief summary will be given for these materials.

The PGEC (Phonon Glass Electron Crystal) concept [26] rules the search for materials with high thermoelectric properties. The manipulation of σ and especially S, aimed at the enhancement of the power factor ($PF = S^2\sigma$), requires a deep knowledge regarding the band structure of the material. Yet, the most commonly pursued phenomenological approach directed toward the search for good thermoelectric materials consists in the depression of thermal conductivity through the reduction of the phonon mean free path, which can be accomplished by introducing into the void of the hosting structure an ion of proper size, disturbing the transmission of vibration quanta through its rattling movement. In this framework, Heusler [27] and half-Heusler phases [29], clathrates [30] and filled skutterudites [32] are currently studied as promising thermoelectrics among intermetallic materials.

2.4.1   Tellurides

Among all the studied thermoelectric materials, tellurides are a family of materials operating at a medium-low temperature, famous for their amazing efficiency [81]. Bi_2Te_3 is one of the earliest studied and it is used for refrigerating purposes since the 1950s as the most efficient thermoelectric compounds for Peltier cells. Its efficiency is quite high at the moment, and researches are being conducted with the aim of further enhancing it. It was found that alloying this material with Sb, Sn and Pb greatly reduces thermal conductivity, increasing *ZT*. The best thermoelectric performance found in literature reached a *ZT* of 2.4 for a *p*-type alloy of Bi_2Te_3/Sb_2Te_3 at 300K [82,83]. Its structure is depicted in Figure 13 [84].
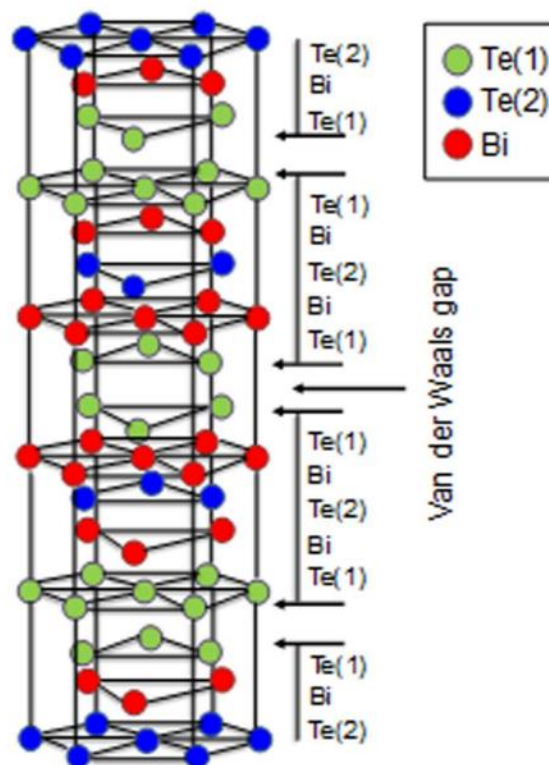
Figure 13 - Schematic structure of bismuth telluride [84].

Another material belonging to the telluride family is PbTe; unfortunately, if doped, it does not present good mechanical properties and is difficult to weld. The search for new materials led to the discovery of TAGS $(AgSbTe_2)_{1-x}(GeTe)_x$. Their figure of merit is one of the highest known, which is why they are widely used in the thermoelectric field.

2.4.2 Half Heusler
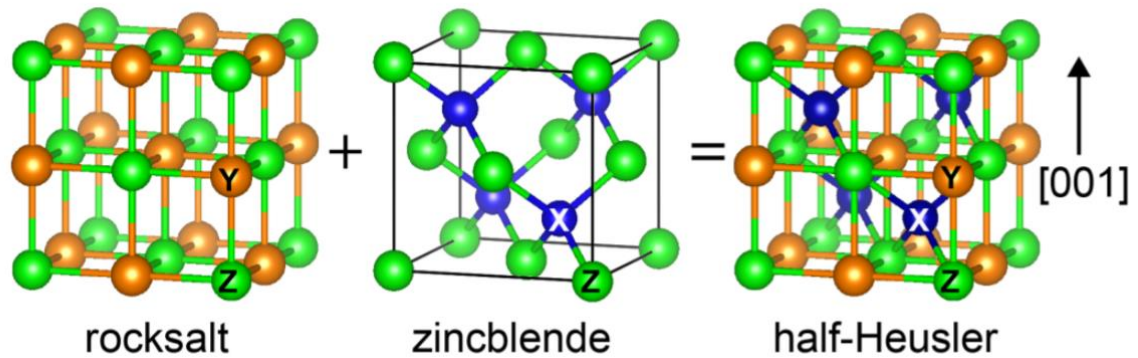
Figure 14 - Crystal structure of a Half-Heusler alloy. The structure is an interpenetration of a rocksalt sublattice and a zincblende sublattice [85].

Half-Heusler alloys find their place in high-temperature thermoelectric applications. The general stoichiometry is XYZ, with X and Y as transition metals and Z as a p-group element, such as Ti, Ni, Sn. The structure is described as the interpenetration of three sublattices, with X and Z occupying a NaCl lattice and Y an FCC lattice (Figure 14) [85].

Each element can be substituted, giving rise to different effects: doping on the Z site affects the carrier concentration while doping on X, Y sites reduces thermal conductivity. The Half-Heusler's thermoelectric performance is very high, reaching *ZT* values around 1 [72]. In Figure 14, the structure for a Half-Heusler compound can be seen [85].

2.4.3 Zintl Phases

Zintl phases are a wide class of compounds consisting of an electropositive metallic component (usually alkaline, alkaline-earthy, lanthanide) combined with non-metals or metalloids able of forming polyanions [86] formed by elements of moderate electronegativity belonging to the *p*-block (for example NaTl). The more electropositive element donates its valence electrons to the more electronegative element; the bonding and structure of the polyanions is understood in terms of the octet rule. These compounds are not ionic, and even if they have some metallic properties, they are neither ductile nor fragile. Moreover, being semiconductors, they are considered promising thermoelectric materials, since they can be doped, and consequently show a low thermal conductivity. They are a typical example of PGEC materials with values of *ZT* ~ 1. Zn_4Sb_3 is a promising thermoelectric material, it has a low cost

due to the abundant presence of zinc, and for these reasons, researchers have already published a number of studies in regards, after having synthesized it with several different procedures [87,88].

2.4.4   Clathrates

Clathrates are another novel large class of compounds, generally with low thermal conductivity, with a large and complex cage structure, in which other elements can be enclosed during crystallization [89,90]; the trapped atom is not able to escape unless the crystal breaks. They can be thought of as periodic solids in which tetrahedrally bonded atoms (typically Al, Ga, Si, or Sn) form a framework of cages that enclose relatively large metal atoms, named guest atoms.

The generic formula is $X_xY_yE_{46-y}$ for type I and $X_xY_yE_{136}$-y for type II, X and Y being the guest atoms, and E the main element. A lot of combinations in elements can be made, resulting in a variety of different materials.

Clathrates have demonstrated interesting properties that are rare in condensed-matter physics. From a thermoelectric point of view, it is interesting to observe that the host atom is not a contributor to the increase of electrical conductivity, while it plays a significant role in the phonon movement of the main structure, thus improving the thermoelectric efficiency. One of the most interesting of these properties for thermoelectric applications is a very low "glass-like" thermal conductivity in Type I clathrates [91].
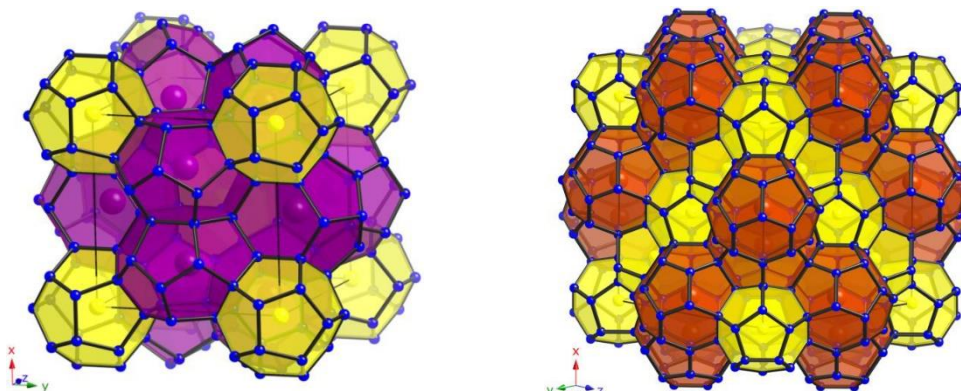
Figure 15 - Crystal structures of type I and type II clathrates [94].

It is worth mentioning the impressive result achieved for the *n*-type $Ba_8Ga_{16}Ge_{30}$, which reached an astonishing 1.4 value for *ZT* [92,93]. In Figure 15, the crystal structures for the type I and type II clathrates are reported [94].

2.4.5 Skutterudites

Skutterudites are a very fascinating class of intermetallic materials; they form one of the most studied families in the last decade due to their promising thermoelectric characteristics.

They can be found in nature as opaque minerals with a metallic gloss; they come from a hydrothermal genesis and they are normally used for the extraction of cobalt. Their name derives from a small Norwegian mining town, Skutterud. In broader terms, they are a family of binary compounds with MX_3 composition, where M is a transition metal element (IX Group), such as Co, Rh or Ir, and X represents a pnictogen element such as P, As or Sb [35], one well-known class of Zintl compounds.

The structure consists of a body-centred cubic cell crystallizing in the $Im\overline{3}$ space group and having $CoAs_3$ as the isotypic crystal [35]: transition metal atoms M are positioned at the vertices of eight cubes, six of them containing pseudo-squared units of pnictogen (Figure 16 - Structure of the $CoSb_3$ skutterudite.). They crystallize in a cubic cell belonging to the $Im\overline{3}$ space
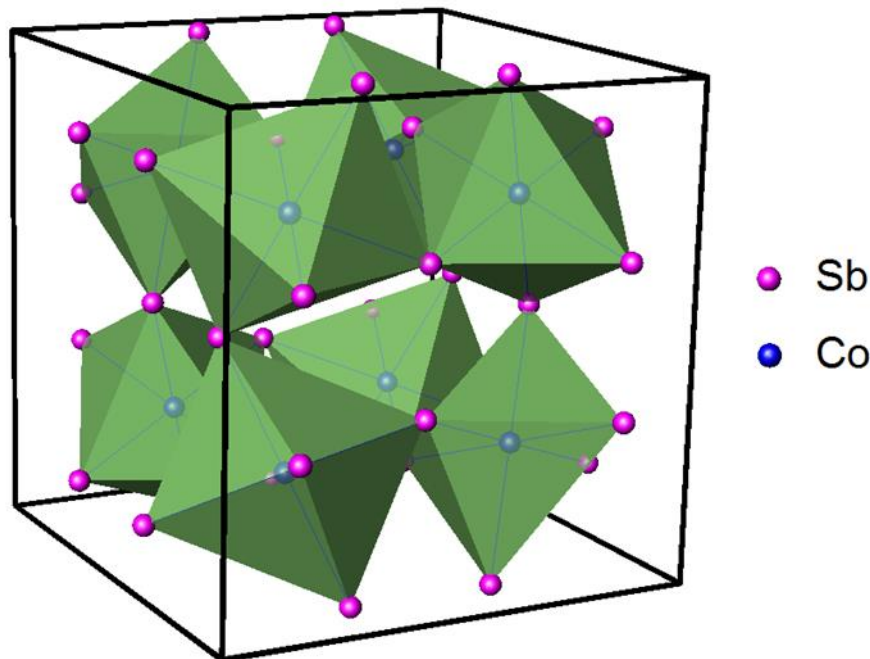
Figure 16 - Structure of the CoSb₃ skutterudite.

group (Pearson symbol $cI32$, isotypic crystal: CoAs$_3$), having three atomic sites: $8c$ (¼, ¼, ¼), $24g$ (0, y, z) and $2a$ position (0, 0, 0) occupied by M and X, respectively. The X$_{12}$ icosahedral cage built around the $2a$ site is of the utmost importance, inasmuch as thermoelectric properties can be enhanced by making a filling, usually with rare-earth ions in order to obtain filled skutterudites. The M-M distance is too large to form a bond, and the relevant links are limited to the interaction between pnictogen ions of the X$_4$ ring and the metallic ions. The bonds pattern causes a rather rigid constriction for compounds that can crystallize with the structure of the skutterudite. As a consequence of this, for example, the impossibility of forming the binary skutterudite completely replacing cobalt with iron or nickel is shown, while it is possible to partially substitute cobalt with a metal of its own group. Moreover, it is possible to symmetrically replace Co with Fe and Ni, in order to preserve the total number of electrons. Skutterudites have high electrical, but also high thermal conductivity; their open structure can host filler ions which not only lower the phonon thermal conductivity but also adjust the electronic count generally turning a metal (the skutterudite) into a semiconductor (the filled skutterudite).

The physical properties of skutterudites depend considerably on their composition. This compositional dependence not only provides a means to investigate the structure-property relationships in this material but also allows the optimization of transport properties for thermoelectric applications. The diversity of potential compositional variants allows for a rich variation in physical properties and it is one of the key reasons why this material continues to be investigated by many research groups. As aforementioned, one approach for optimizing these materials is void-filling [91].

Skutterudites are solids with an open crystalline structure showing excellent electronic properties; filling the voids with different species can modify, and in particular lower the reticular thermal conductivity. Filled skutterudites have the general stoichiometry $X^{4+}[M_4Z_{12}]^4$, where X is an electropositive filler ion, M is a metal belonging to the VIII Group, such as Fe, Ru and Os, which replaces the metal of the IX Group of the binary skutterudite; Z is the pnictogen atom (Figure 17). While the binary skutterudite with the sole metal M does not form due to electronic instability, the filler X can compensate for the lack of electrons.
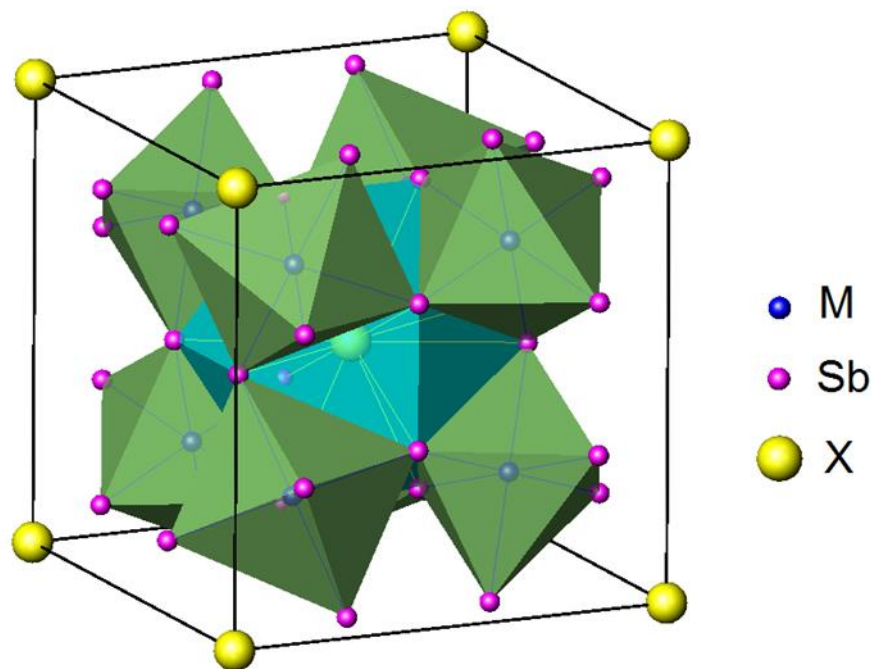
Figure 17 - Structure of the XM_4Sb_{12} filled skutterudite.

The electronic structure of the filled skutterudite can be changed by replacing the atom M of the IX Group with a mixture of electron-deficient atoms T of the VIII Group and electron-rich T' atoms of the X Group, following the stoichiometry $X'_y(T_xT'_{1-x})_4X_{12}$, where X' is an electropositive ion, usually a rare earth or an alkaline-earth.

The first type of skutterudites synthesized during the present work are Fe,Ni-based compounds (elements are enlightened in Figure 18) and present different conducting behaviours: the compound goes in fact from a *p*-type to an *n*-type semiconductor by varying the relative content of Fe (T) and Ni (T'). The filler is necessarily chosen to modify the electronic and phonon properties in order to improve the thermoelectric properties. The variety of possible fillers will allow tuning the electronic structure of these compounds, providing materials characterized by different and interesting properties [42].
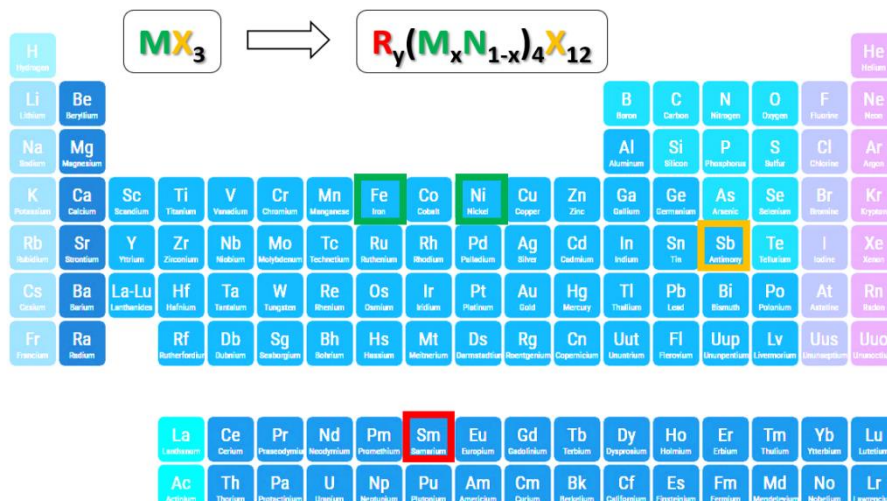
Figure 18 – Periodic table and skutterudite formula. Highlighted elements are the one in use for the Fe,Ni-based filled skutterudite under investigation in this work.

The filler atom content is a key parameter when discussing the electronic properties of filled skutterudites and the correlations with the structural features of the phase; therefore, the Sm occupancy factor of the 2*a* position as resulting from Rietveld refinements performed on the system $Sm_y(Fe_xNi_{1-x})_4Sb_{12}$, is shown in Figure 19 as a function of the Fe amount [42]. As expected, a decreasing linear behaviour is observed with increasing the Fe substitution by Ni, due to the increasing negative charge provided by the latter. The thick black line represents the Sm amount theoretically necessary to exactly reproduce the electronic count of the parent compound $CoSb_3$, while the thin one is the regression line interpolating experimental data; the crossing point of the two lines, located at x ≈ 0.63 and y ≈ 0.30, represents the boundary composition between *p*- and *n*-type skutterudites.
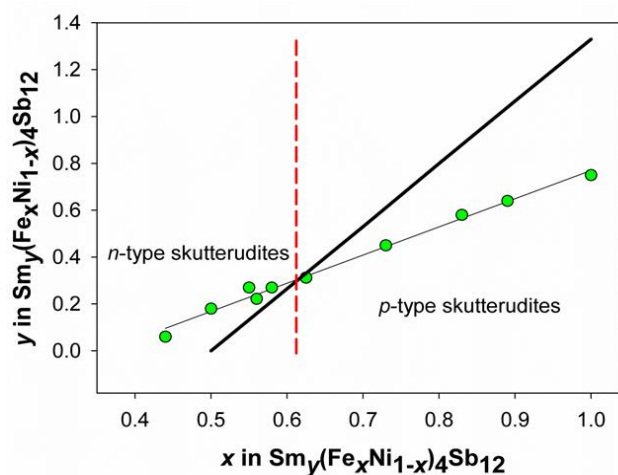
Figure 19 - Sm occupancy factor as resulting from Rietveld refinements. The black thick line represents the amount of Sm needed to obtain an intrinsic semiconductor, while the red dotted line interpolates experimental data [42].

The filling element must satisfy steric and also electronegativity requirements. The fillers are weakly bound to the atoms that form the voids in the structure: this allows us to see them as independent ions that vibrate within their cavity, thus reducing the thermal conductivity of the system. The PGEC theory, developed by Slack [26], explains why filled skutterudites have a value of the merit figure *ZT* higher than normal binary skutterudites.

Best thermoelectric performances of bulk skutterudites are reported in Figure 20 [43, 95,96,97,142,138]. As it is visible, literature regarding *p*-type is quite scarce, while more promising and numerous data for *n*-type ones are available. Some examples of excellent results are the *n*-type $(Sr,Ba,Yb)Co_4Sb_{12}$ with $ZT \approx 2.0$ at 835 K [39] and the *p*-type $DD_{0.7}Fe_3CoSb_{12}$ with $ZT > 1.3$ at 856 K [40].

Since each type of ion has its characteristic frequency of vibration that reflects its mass and size, some studies have been done for a possible multiple filling; to maximize the impact on the phonon component, ions of significantly different sizes and masses can be chosen [98,99,100].
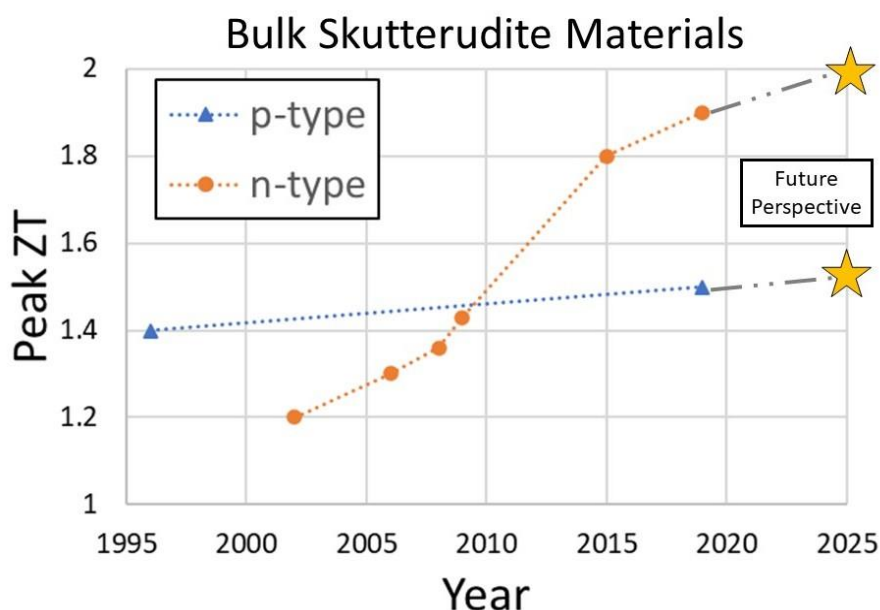
Figure 20 - Best bulk skutterudite figures of merit in literature for both p- and n-type materials. Future perspective is shown in the right side of the graph.

2.4.6   Metal Oxides

Metal oxides are ionic compounds of metal cations and oxygen anions alternately packed by the Coulombic attracting interaction between them. Regarding their characteristics

of interest for TE applications, they typically have large carrier mobility, which is a positive feature to enhance the power factor, but they also present high values of thermal conductivity because of the strong bonding in the metal oxides and the small atomic mass of the oxygen. Furthermore, the bond between the metal and the oxygen is extremely polarized, localizing electrons on the positive cation. Nonetheless, overlapping of orbitals is lower than covalent compounds [70]. Due to the aforementioned reasons, oxides were not considered for thermoelectric applications until 30 years ago. Despite their not so competitive TE properties at low-medium temperatures, metal oxides are of interest in the field of thermoelectrics thanks to their mechanical, chemical and electrical properties. They are stable and suitable at high range temperatures, where other materials can melt, decompose or oxidize. Moreover, they are eco-friendly and manufacturing cost is generally low [101].

Best representative materials for p-type metal oxides we find layered cobaltites [102,103] and oxyselenides [104,105], allowing decoupling of transport properties. The finest compounds of the layered cobaltites family are $Na_{0.75}CoO_2$ and $Ca_3Co_4O_9$, and the structure is stacked [106] (Figure 21), with the electrical transport mainly favoured by CoO_2 layers while a thermal conductivity of layered materials is likely to be considerably low thanks to phonon scattering at the interfaces between the layers.
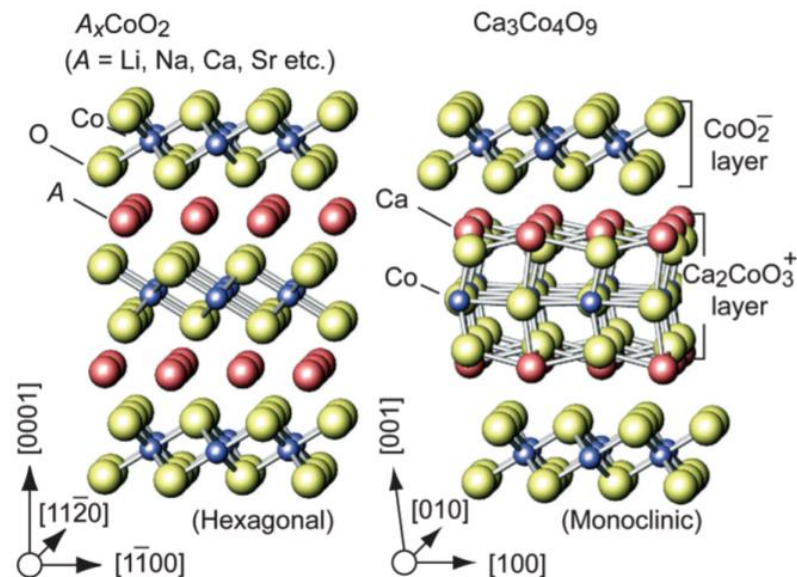
Figure 21 - Crystal structure of cobalt oxides [106].

The n-type materials present lower properties at the present day, and their main exponents are Ruddlesden-Popper phases [107,108] and zinc oxides [56,57,109]. Zinc oxide (Figure 22), of interest in this thesis work, is a wide band gap semiconductor with a direct band

gap of 3.2-3.5 eV. Both Zn and O are low-priced and abundant, and the material itself shows a high power factor at room temperature, unfortunately, paired with the typical low thermal conductivity of metal oxides. Though, a trivial amount of Al-doping boosts the electrical conductivity of more than 3 orders of magnitude at room temperature and changes the conduction behaviour from semiconducting to metallic [70]. Samples containing a 2% of Al dopant are considered the best composition so far for TE applications, and they showed significant power factors of $10\text{-}18\cdot 10^{-4}$ W/m$\cdot$K^2 over a wide temperature range [110].

Another remarkable well studied *n*-type metal oxide for TE purposes is crystalline SrTiO$_3$. Having a melting point of 2080°C, it finds particular interest for high-temperature applications [111].
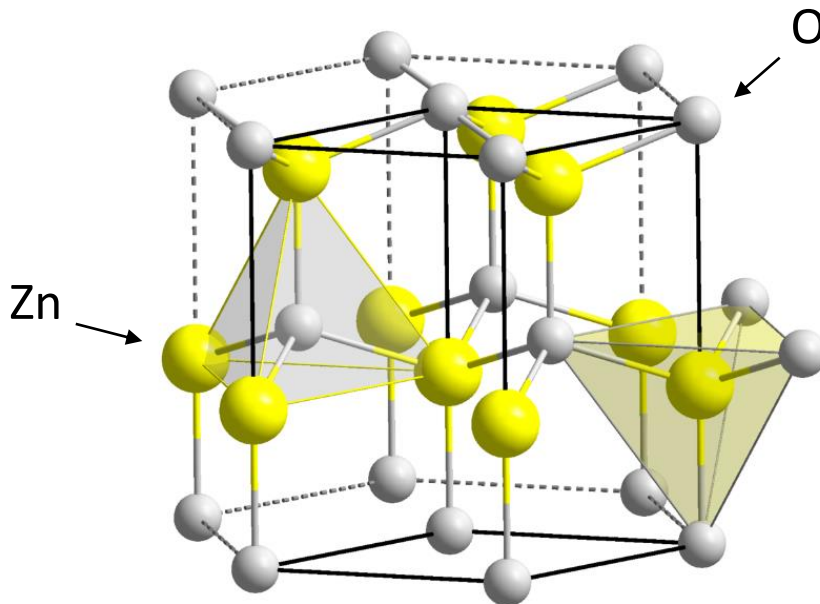
Figure 22 - ZnO crystal structure [109].

2.4.7 Thermoelectric Thin Films

As aforesaid, the efficiency of thermoelectric materials is controlled by the indicator *ZT*, which should be as high as possible in order to have a respectable thermoelectric performance. Filled skutterudites are one the most promising materials since they exhibit legitimately good values for the figure of merit *ZT*. As illustrated in the former section, filler atoms contribute to the diminution of thermal conductivity, leading to the enhancement of *ZT*. Nonetheless, other factors can be manipulated to further improve the performance, for example, synthesizing low-
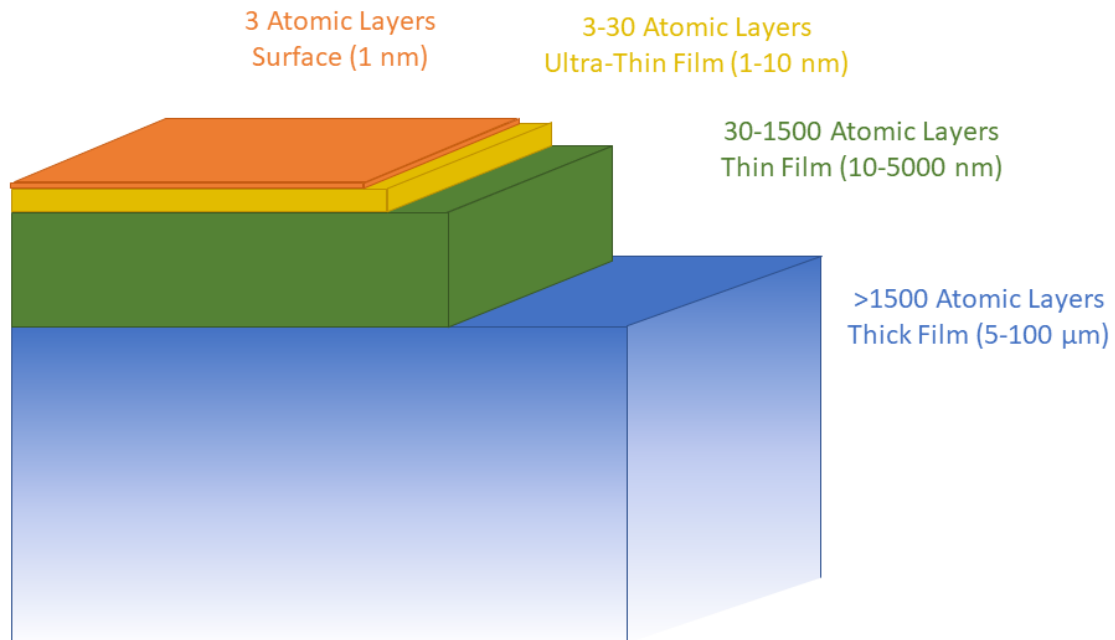
Figure 23 - Visual representation of the thickness of various types of films.

dimensional systems to make the most of the presence of grain boundaries and surface boundaries as supplementary phonon scattering points. One example of low-dimensional systems are thin films [112].

Thin films are material layers whose thickness scales between few nm to 5 µm. For thicknesses between 5 and 100 µm, we refer to thick films (Figure 23). Both thin and thick films cannot stand alone (free-stand configuration); they are deposited on substrates with a much larger thickness. The research on thin films is of uttermost importance because of the variation in properties that take place in such low-dimensional systems; the surface to volume ratio in thin films is extremely large, meaning that surface features intensely affect the film characteristics.

The fabrication of TE thin films absolutely fits the need for small-volume power

generators, which have been gaining vast significance in the last years, because the applicative possibilities as thermoelectric energy harvesting to power Internet of Things (IoT) sensors and devices are important [113,114,115,116]. The chase of an extensive network of communicating devices enhanced the research for micro-generators, and thermoelectrics could play their part in this emerging field. Among the many benefits coming with the TE technology, the fact that thermoelectric devices need little to no maintenance is of particular importance. Today's main power generation systems for portable devices are batteries and their lifespan is very limited: they need to be recharged at some point, implicating that some labour force will be required to do maintenance. Clearly, the power output conceded by a battery is larger than that of a thermoelectric device, and in no way TEGs aim to replace other and more efficient technologies, though, in some occurrences, thermoelectrics could be a cost-effective replacement or they may be coupled to other technologies as well, like to photovoltaic cells [117]. One important example is the build-up of the Wireless Sensors Networks (WSNs) [118,119,120,121].

Given that fabricating low-dimension systems is convenient in terms of performance and applicability, skutterudite thin films were prepared as one of the main topics of this doctoral project.

Not so many skutterudites have been deposited as thin films through the PLD technique so far. For example, Suzuki et al. prepared thin films of unfilled skutterudite $CoSb_3$ by ArF excimer laser (λ=193 nm) on silicon substrates and reported the successful growth of single-phase $CoSb_3$ films for a 70°C deposition, while other temperatures deposition led to the formation of Co-rich and Sb-rich phases on the films [122]. Dauscher et al. instead prepared thin films of the filled skutterudite $Ca_{0.1}Co_4Sb_{12}$ on silicon substrates, using a Nd:YAG laser and tested two different wavelengths ($\lambda = 355$ nm, $\lambda = 532$ nm) and several different deposition conditions. They achieved the best results using the 532 nm wavelength, despite further improvements on the film crystallinity must be done [123]. A more recent example of deposition of Co-based skutterudites is reported by Kumar et al., who grew thin films of $In_{0.2}Yb_{0.2}Co_4Sb_{12}$ on quartz substrates using a KrF excimer laser (λ=268 nm). They reported not so successful results for the thermoelectric properties, which are blamed by the authors on the polycrystalline nature of the films [112]. A Fe/Co-based filled skutterudite $LaFe_3CoSb_{12}$ was used as a target in another work of Suzuki et al. where an ArF excimer laser (λ=193 nm) was employed to grow films on glass substrates. From thermoelectric measurements, they found

smaller values for the Seebeck coefficient compared to the bulk values, probably due to the numerous grain borders present on the sample [122]. One more interesting work found in literature regards the deposition of the filled skutterudite $PrFe_4Sb_{12}$ performed by Baumbach et al. using a KrF excimer laser ($\lambda = 248$ nm). For this work many substrates materials were tested: YSZ, MgF_2, MgO, Al_2O_3, $SrTiO_3$ and silicon. Also, the depositions were performed at high temperatures, ranging from 300 to 500°C. They obtained high-quality films and concluded that the type of substrate does not affect the film crystallinity, which is far more dependent on the deposition conditions [124].

Especially, the attention of researchers has been focused on the development of stable, environmentally benign, abundant, and cost-effective TE materials based on oxides. In the 1990s extensive research on bulk oxide flourished with common effort focused to enhance the TE performance by atomic substitutions and improved grain connection [70,125]. To date, the best TE performance of the currently available oxide materials is $ZT = 0.64$ for n-type $Zn_{0.96}Al_{0.02}Ga_{0.02}O$ [53] and 0.74 for p-type $Ca_{2.5}Tb_{0.5}Co_4O_9$ [54] at 1000 K. The ZT of oxides is not yet up to the level of the best conventional TE materials and requires to be drastically improved to reach a level acceptable for practical applications. The bulk oxides also have the main disadvantages of the requirement of a long time for sintering and fabrication of the n- and p- elements, and their assembling in module shape, and mechanical fragility. All these drawbacks can be overcome by using oxide thin films. Thin-film materials offer significant advantages to developing oxide TE with high performance: low dimensionality, rapid fabrication, control of strain at the interface with substrates, and the possibility to insert artificial nano-defects to improve the phonon scattering.

Recently, our group afforded research on oxide thin films for thermoelectric applications and encouraging preliminary results have been obtained. At first, epitaxial thin films of AZO were fabricated by pulsed laser deposition (PLD) on several single crystals ($SrTiO_3$, Al_2O_3) and amorphous silica substrates. Independently on the substrate, films always show higher values of ZT in comparison with corresponding bulk AZO: for example, at T = 600 K, $(ZT)_{AZO\text{-}on\text{-}STO} = 0.03$ [56,126]. The superior performance of films is due to their lower thermal conductivity: $\kappa_{AZO\text{-}on\text{-}STO}$ (300 K) = 6.5 W/m·K [56,126] while κ_{BULK} (300 K) = 34 W/m·K. In these series, the grain boundaries can be considered as natural nanodefects for the enhanced scattering of phonons and consequent depression of κ respect to the bulk material. As a demonstration of this effect, the film on fused silica, showing additional grain boundaries at

the seed layer on the substrate, had even lower thermal conductivity: κ_{silica} (300 K) = 4.89 W/m·K and larger ZT: ZT_{silica} (600 K) = 0.045 [126].

The insertion of artificial nanodefects has been subsequently considered with the purpose of further depressing κ and enhancing ZT. Several approaches have been tried by our group, as reported in Figure 24: insertion of hydroquinone nanolayers in AZO films prepared by atomic layer deposition (ALD): κ_{ALD} (300 K) = 3.56 W/m·K [127]; addition of polymethylmethacrylate (PMMA) particles to AZO films prepared by multi-beam multi-target matrix-assisted PLD (MBMT/MAPLE-PLD): κ_{MAPLE} (300 K) = 5.9 W/m·K and ZT_{MAPLE} (600 K) = 0.07 [128]; formation of nanopores in AZO films prepared by Mist-Chemical Vapor Deposition (Mist-CVD): κ_{porous} (300 K) = 0.60 W/m·K and ZT_{porous} (300 K) = 0.06 [129]; dispersion of Al_2O_3 nanoparticulate in AZO films prepared by surface-modified target PLD: $\kappa_{nanoAl2O3}$ (300 K) = 3.98 W/m·K and $ZT_{nanoAl2O3}$ (600 K) = 0.0007 [130]. AZO thin films deposited by PLD in vacuum reached a figure of merit of ZT_{PLDvac} (600 K) = 0.07 [131]. Several groups worldwide had recently obtained marvellous results with different kinds of dopants, like the κ (300 K) =1.19 W/m·K and ZT (300 K) = 0.1 of magnetron sputtered AZO films by Loureiro et al. [132], the κ (323 K) = 3.37 W/m·K and ZT (423 K) = 0.05 of CNT-added evaporated porous AZO films by Liu et al. [133], the κ (300 K) = 1.1 W/m·K and ZT (300 K) = 0.042 of amorphous ZnO_xN_y PLD films by Hirose et al. [134], the κ (300 K) = 1.8 W/m·K and ZT (383 K) = 0.019 of dual doped InGaZnO PLD films by Nguyen et al. [135], just to cite the most impressive ones. All these successful examples highlight the promise of nanostructured doped ZnO films for future energy harvesting applications. In Figure 24 best

results on AZO are reported, including the point enlightened with the green star which shows the value obtained in the study presented in this thesis in Chapter 5.
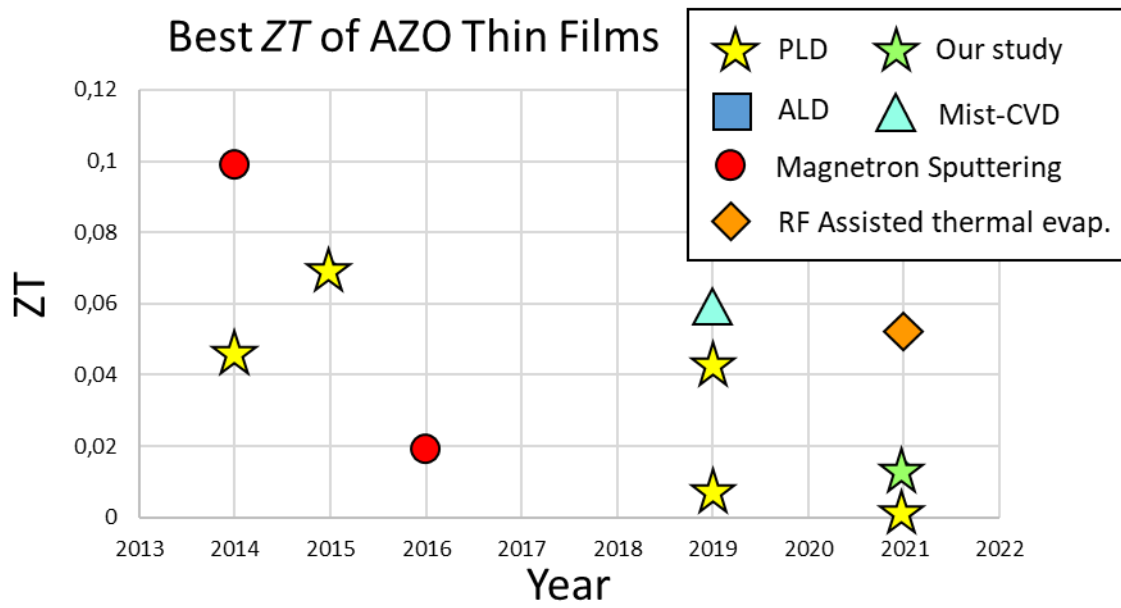
Figure 24 - Best performances of AZO thin films deposited by means of different techniques [126,128,129,130,131,132,133,134,135].

2.5 Thermoelectric Modules and Applications

A thermoelectric generator is a useful and environment-friendly device for direct energy conversion. TE devices are semiconductor devices that have the ability to either generate a voltage when exposed to a temperature gradient, exploiting the Seebeck effect, or produce a temperature gradient when supplied by electricity, exploiting the Peltier effect

Two blocks of semiconductor, one *p*-type (P) and the other *n*-type (N), are joined by a metal interconnect at one end and connected in series to a voltage source or load at the other end. The two blocks share a common temperature at each end and thus are thermally in parallel across a temperature difference $\Delta T = T_h - T_c$.
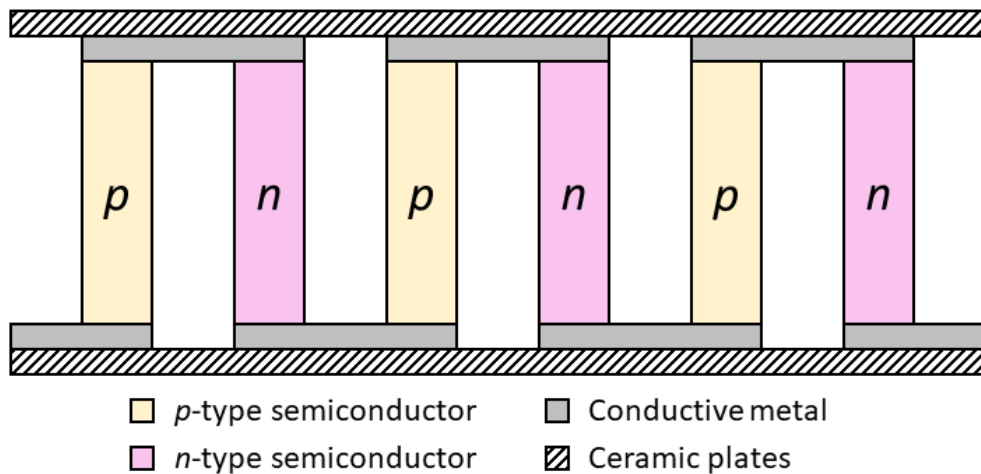
Figure 25 - Schematic representation or the section of a thermoelectric device.

The connections are realized with a good electrical conductor, while the structure is held together with the help of an electrical insulator. A schematic representation of the thermoelements' connection is shown in Figure 25.

In the power generation mode, the applied temperature gradient is opposed by a concentration gradient of the mobile carriers. This is the Seebeck effect, and the Seebeck voltage places the hot junctions in reverse bias and the cold junctions in forwarding bias. By convention, *p* materials have positive *S*, while *n* materials show a negative value of it, and the overall Seebeck coefficient of the couple is $S = S_p - S_n$ [136].

Recently, with the development of microelectronics and increasing demand for sustainable energy harvesting, high power density TE devices that are micro-sized and

lightweight have become the subject of rapidly growing interest. Compared with traditional brittle and rigid TE devices, a micro-TE device is essential to obtain low temperatures such as that of the human body or flexible electronic devices, thus, minimizing heat loss and achieving highly efficient energy conversion. Additionally, the integration of a TE device into the micro-system can act as the self-powered source, cooler, or sensor, and has significant potential for practical application. Thus, motivated by these intriguing prospects, considerable effort has been devoted to exploring micro-TE devices in the past decade.

3 EXPERIMENTAL DETAILS

3.1 Fabrication of Skutterudite's Targets

3.1.1 Synthesis Methods

Skutterudites' synthesis is difficult to set up because of the numerous variables that contribute to the fabrication process. The methodically and careful understanding of the diagram phase of a system is of the utmost importance in order to obtain a successful synthesis. In general, thermoelectric materials, including skutterudites, are constituted by a lot of atoms (acting as fillers or dopants), giving origin to a complex mishmash of chemical-physical characteristics belonging to each of them, i.e. melting points and vapour pressures. Nonetheless, the literature regarding phase stability in skutterudites is relatively meagre and the involved diagrams are often quite complicated [137]. In Figure 26, an isopleth section of the ternary phase diagram for the Fe/Ni/Sb system is reported [138,139,140].
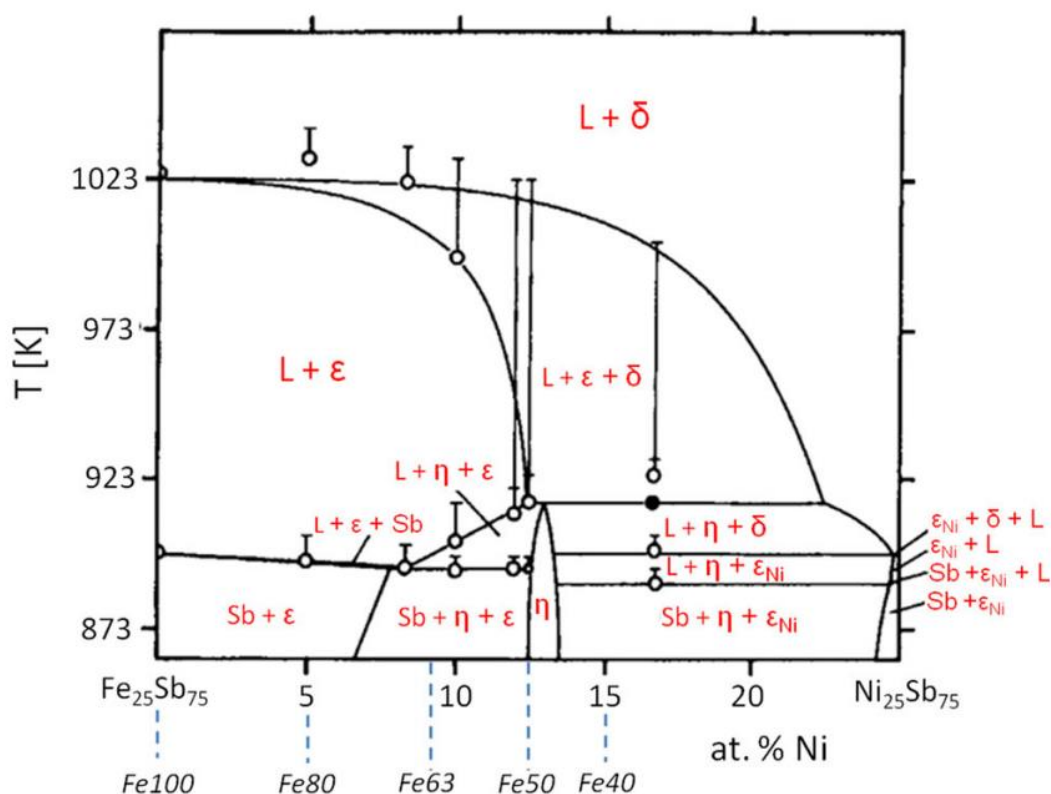
Figure 26 - Isopleth section of the phase diagram for a Fe-Ni based skutterudite [138].
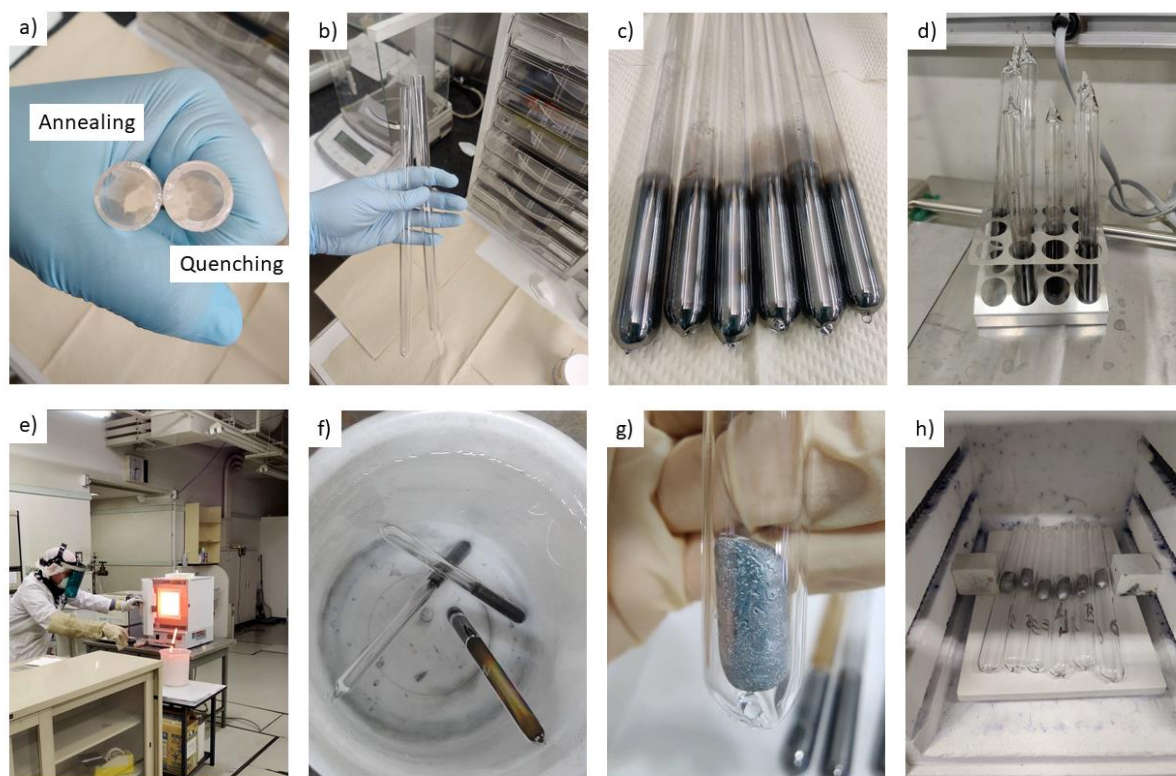
Figure 27 - Pictures from the melting-sintering-quenching synthesis of filed skutterudites. a) Difference in thickness for quartz tubes: 1mm wall is used for the annealing while the more resistant 2mm wall tube is used for the quenching. b) One sided sealed tubes. c)carbon coating in the lower part of the quartz tube with the aim to limit the reactivity between elements of the material and the wall of the tube. d) Tubes containing pure elements sealed under vacuum. e) Quenching of the tube after melting process. f) Quenched tubes in a bucket of water. g) Clean skutterudite sealed under vacuum for the annealing process. h) Samples in the furnace for the annealing process.

Together with my current and previous research groups (Paolo Mele in Japan and Cristina Artini et al. in Italy), we carried out an important number of studies in the field of skutterudites, investigating the properties of several compounds, ranging from *p*- to *n*-type compositions [34,41,42,45,138,141,142,143,144,145]. The main synthesis technique used is the traditional melting-quenching-annealing process, originally proposed by Sales et al. [146,147]. The process consists of three steps: first, the elements in stoichiometric quantity are melted together in a vacuum environment; second, the molten cast is quenched in air or water; third, the cast is annealed for about seven days. The annealing process is needed for the formation of skutterudite.

In the case of Fe-Ni based skutterudite, pictures of the synthesis are displayed in Figure 27. Small pieces of pure elements Fe (Alfa-Aesar, 99.99 wt.%), Ni (Alfa-Aesar, 99.99 wt.%), Sm (NewMet, 99.9 wt.%) and Sb (Mateck, 99.99 wt.%) are polished in order to eliminate any

surface oxide layer, which could alter the composition of the sample, and they are weighed on an analytical scale in due amounts and placed into a quartz tube subsequently sealed under vacuum, with the aim to limit oxidation and avoid unwanted reactions. The starting mixture is then reacted at 1223 K for 3 hours and quenching in a salted iced water bath follows. The Sm amount to be employed is calculated by considering results obtained by Artini et al. [42]. A slight excess of Sb is used too, in order to compensate for its non-negligible vapour pressure (10^{-3} mm Hg at 873 K [148]). As-cast samples are then annealed in vacuum at 873 K for 7 days.

The conventional melting-annealing-quenching method is not the only procedure to prepare skutterudite material, further synthesis routes have been explored over the years. An example of a substitute preparation technique is given by mechanical alloying, developed in the mid-1960s for superalloys, and it is based on the solid-state reaction that takes place during the ball-milling process. Undoubtedly, additional annealing is required to achieve a pure material because it is not possible to obtain ready skutterudite with powders milling itself. Many successful attempts of skutterudite fabrication with ball milling can be found in the literature [149,150,151]. Mechanical alloying is a valid alternative; however, the possibility of sample contamination is large if the jar and balls are not cleaned with extreme care. Moreover, the size and number of spheres, as well as their material, must be chosen with care, taking into consideration the ball to powder volume ratio and interactions between materials.

An additional example of a fabrication path for skutterudites is the Selective Laser Melting (SLM). This technique, developed in 1995, involves a high-energy laser that locally melts elemental powders and allows the reaction to form the desired skutterudite structure. The melting/solidification process is responsible for the formation of dense skutterudites, indicating that no supplementary annealing is strictly essential. Some interesting results for SLM-prepared skutterudites can be found in the literature, showing comparable performances to the ones of samples prepared by the melting-quenching-annealing method [149,152].

Besides the traditional preparation approaches which include some kind of melting, other synthesis routes exist, categorized as chemical methods. One example is the hydrothermal (HT) synthesis, which relies on the chemical reactions taking place at high temperature and high pressure in a precursor aqueous solution. The crystalline material grows upon a single crystal located in the reactor [153]. Although the hydrothermal process is a deep-rooted fabrication route for inorganic materials, it is not found very fruitful for the preparation of skutterudites, as samples prepared via HT synthesis reveal poor TE performances [149].

Analogous negative outcomes are reported for the other chemical syntheses, i.e. sol-gel and co-precipitation methods, making them not competitive compared to traditional fabrication routes.

For the purpose of my PhD project, the melting-quenching-annealing process was selected over others due to the respectable results showed during previous works of the research group. A negative point of this technique is the long time needed, especially due to the annealing process, but, as a result, the quality of the samples is noticeable. Additionally, it does not require any particular equipment, apart from a furnace and a torch to seal quartz with a paired vacuum system.

3.1.2 Densification of the Material

3.1.2.1 Spark Plasma Sintering

Furthermore, a supplementary step of material densification is required to improve grain connection, and hence the electrical conductivity. In the case of the present work, densification was compulsory since the skutterudite was needed in form of a dense target for films preparation. An established way to achieve high-density pellets for the Pulsed Laser Deposition (PLD) is the Spark Plasma Sintering (SPS) technique, also known as Pulsed Current Electrical Sintering (PCES), Field Assisted Sintering Technique (FAST) or Electric Current Activated Sintering (ECAS) whose asset is to use plasma to effectively sinter and consolidate powders, allowing the densification at significantly lower temperatures than other sintering techniques. This technology started in the late 1920s when a sintering process using electrical energizing was introduced in the USA. In the meantime, in Japan, ongoing research on the process of pulsed current activated sintering intensified and was patented in the 1960s [154,155]. This method seems to be characterized by technical and economic advantages over conventional sintering methods such as Hot Uniaxial Pressing (HUP), Hot Isostatic Pressing (HIP), etc.

SPS is a newly developed process that makes it possible to sintering at low temperatures and for short periods by charging the voids between powder particles with electrical energy and effectively applying high-temperature spark plasma rapidly generated. It is regarded as a rapid sintering method similar to microwave sintering. Therefore, it is capable of sintering ceramic powders quickly to a high density at a relatively lower temperature, compared to the conventional sintering method. Due to the applied electric field, the diffusion rate increases and therefore, the powder can be densified at a much lower temperature with a shorter holding time (only a few minutes). In SPS, mechanical uniaxial pressure is applied to the sample placed in a die by a vertical piston while the system is being heated. Graphite is the most common die material because it is relatively inexpensive, is easily machined, and has excellent creep resistance at high temperatures. The rate of densification can be deduced by following the piston displacement. Its main characteristic is that a pulsed DC current is directly passed through the graphite die while uniaxial pressure is applied. The characteristics include high heating rate, the application of pressure, and the effect of the current. The main advantage in comparison with other sintering techniques is the high heating rates that can be applied during sample sintering.

Figure 28 - Detail of the inside of the SPS – 511S, Fuji Electronic Industrial located at NIMS (Tsukuba, Japan).

The extremely short processing times allow obtaining special microstructures in the final material that are unattainable by other sintering techniques [156]. Thus, it is possible to fabricate a dense material with an average grain size similar to starting powders. Nowadays,

one of the challenges related to this technique is the scaling-up in order to obtain large samples or complex shape components.

The SPS method was successfully used for the densification of Fe-Ni in previous works of my research group [41,141,143].

3.1.2.2   Open Die Pressing

Another viable way to obtain densified materials is the Open Die Pressing (ODP) technique which was performed during the present work.

Open Die Pressing is a newly developed technique that allows the sintering of thermoelectric materials in a fast and easy way. Previous works of the research group that performed the ODP on the skutterudite (Fanciulli et al., CNR Lecco, Italy) showed the potential of this technique [157,158], for which two main benefits can be accounted over other densification methods: the rapidity of the process, that inhibits undesired grain growth and the low operating temperature, that prevents diffusion or reactions of the powders. On the other hand, to execute this sintering technique, very good manual skills of the operator are required, since the incandescent sample is rapidly moved from the furnace to the pressing machine. Moreover, the final shape of the densified piece is a dog-bone shape (Figure 29), which could not be compatible with many applications.

Figure 29 - Skutterudite sample after ODP pressing (≈ 3 cm long). It is noticeable the dog-bone shape of the resulting dense sample.

Working inside an Ar-filled glovebox, the ODP process starts from powders of the sample introduced in a cylindrical metallic sheath as mechanical support for the process. The Fe sheath's internal surface is covered with a thin layer of boron nitride, used as an insulating material to prevent the sample core's sticking to the internal metallic walls. The sheath is closed

with a Fe plug (2 mm thick) with a small hole inside, which is necessary to allow Ar's outflow and protect the material from oxidation during the pressing process. The encapsulated powders are manually consolidated using a percussor and a hammer, reaching at least 80% of the theoretical density value.
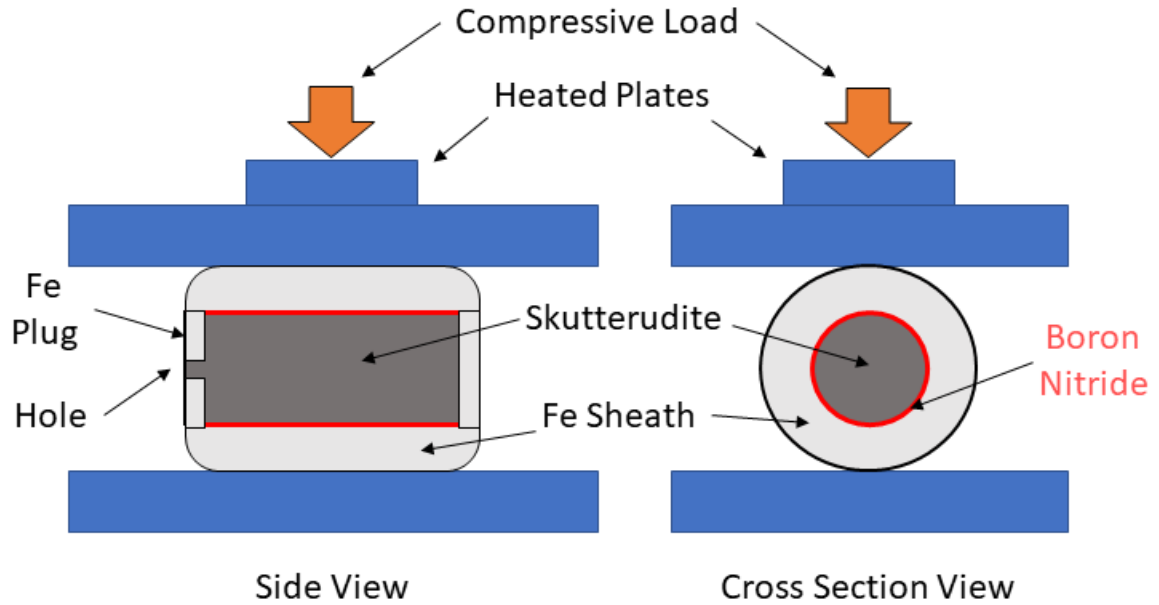
Figure 30 - Scheme of Open Die Pressing.

Afterwards, the cylindrical composite is taken out from the glove box and preheated at the processing temperature in a static furnace. Powders' temperature is measured with a thermocouple inserted in the stopper's hole of the sheath. After the fast preheating, the sheath is pressed longitudinally while the two plates of the press are heated up to the temperature required for sintering the sample.

3.2   Thin Films Deposition

A variety of different methods can be used to fabricate thermoelectric thin films (Figure 31); a brief summary will be given in this section.
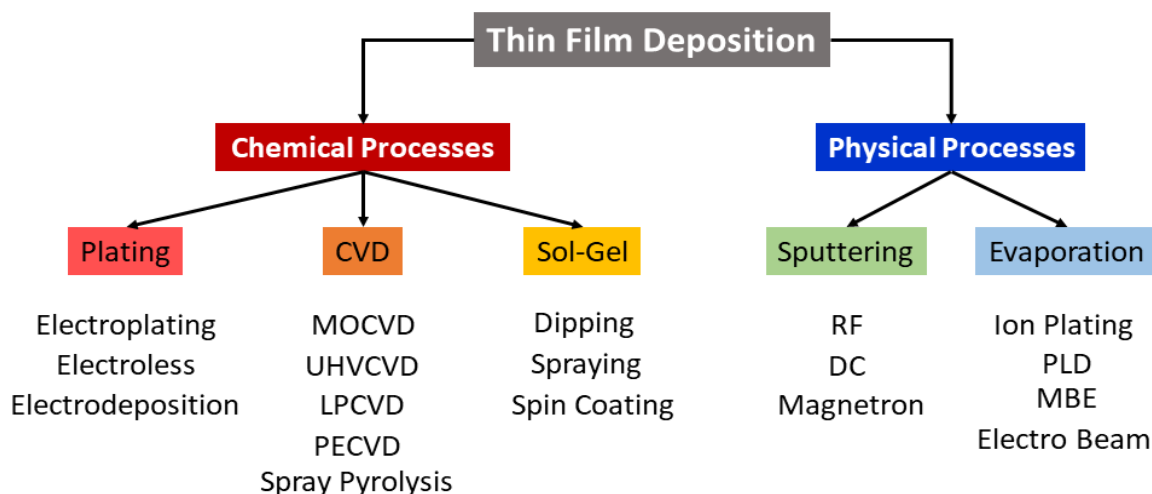
Figure 31 - Thin films deposition techniques divided in chemical and physical processes.

Chemical Vapor Deposition (CVD) is one of the most ancient films preparation techniques: the first application dates back to the 1800s when it was employed for the deposition of metallic coatings. During the 1900s, the technique was methodically refined and, at the present time, it is one of the most well-known materials' fabrication procedures. It is classified as a chemical method since it includes chemical reactions in the vapour phase. In general terms, films are grown on a substrate after the exposition to chemical vapours of a precursor compound. Films from a lot of different materials can be prepared, varying from metallic coatings to insulator films. Contingent on the deposition's conditions and the nature of the precursor, numerous CVD variants can be identified; the most common are Metal-Organic CVD (MOCVD), Ultra-High Vacuum CVD (UHVCVD), Low-Pressure CVD (LPCVD) and Plasma-Enhanced CVD (PECVD) [159,160]. Another chemical method is electrodeposition, a relatively new type of deposition that relies on the reaction occurring in an electrolytic cell. The potential of this technique lies in its cost-effectiveness, rapidity and simplicity and feasibility at low temperature; however, it is very difficult to control all the variables that come into play during deposition: the ionic strength and pH of the electrolyte solution, the voltage and current applied to the circuit, temperature and other factors significantly influence the quality of the film and affect reproducibility [159].

Moving on from the chemical methods, we find the physical vapour deposition (PVD) techniques, which do not strictly involve a chemical reaction but rely on the vaporization and condensation process. Typically, the setup for a physical film deposition consists of a target, from which material is evaporated, and a substrate, on which material is deposited in order to grow a thin film. Different vaporization systems can be used, each one corresponding to a specific physical vapour deposition technique. For example, if the material ejection from the target is caused by the interaction with a high-energy ionic or electronic beam, we refer to sputtering methods, instead, if the evaporation occurs after heating of the target, we refer to thermal evaporation [159,161].

3.2.1   Pulsed Laser Deposition (PLD)
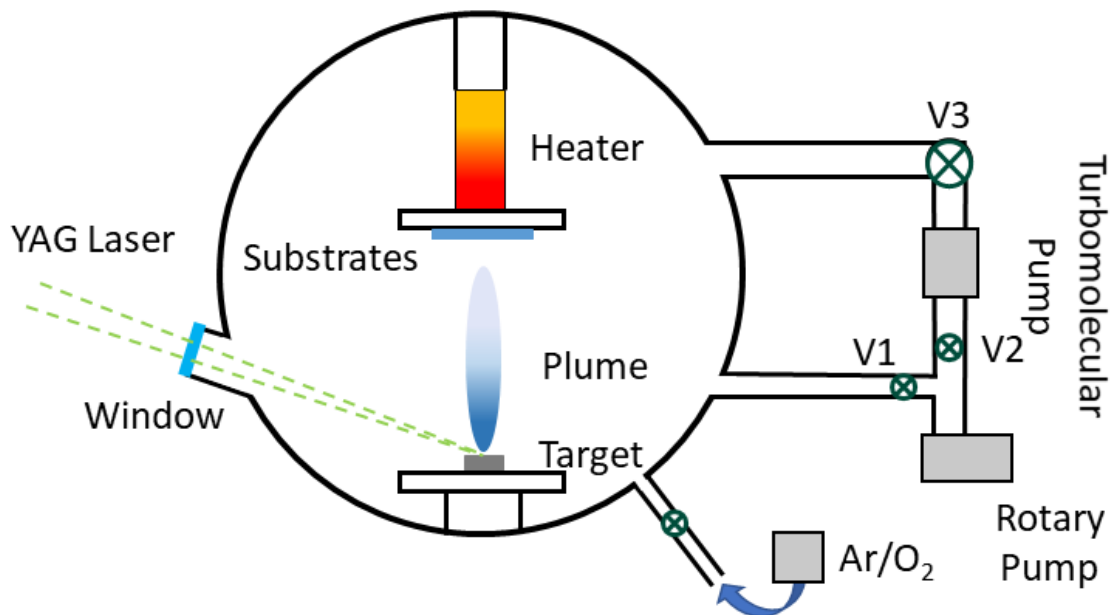
Figure 32 - Scheme of the apparatus for PLD deposition.

During the last thirty years, Pulsed Laser Deposition (PLD) has become a vastly widespread thin films fabrication technique. The main constituents that form the experimental apparatus (Figure 32) are the laser source that provides the energy to ablate the material, the optical system that focuses the laser beam, the vacuum chamber inside which the deposition is performed, the vacuum pumps through which the required vacuum environment is achieved, a

heating system to raise the temperature inside the chamber and an optional gas-line to perform depositions in specific atmospheres, typically O_2 or Ar environments.
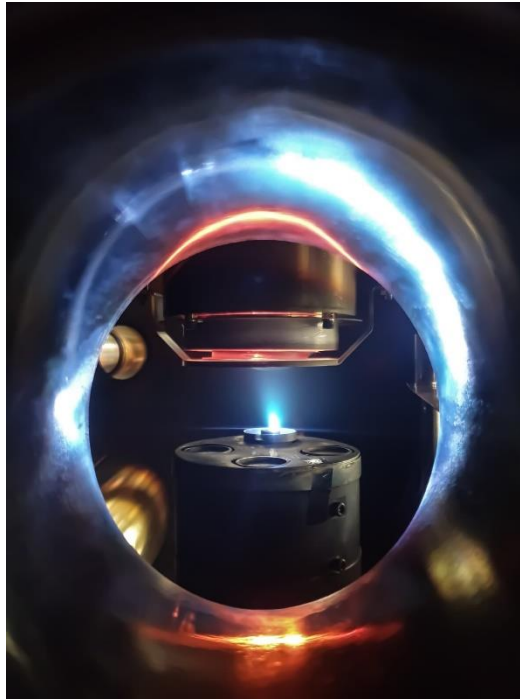
Figure 33 - Picture of the chamber used to deposit skutterudites at Shibaura IT. The blue light at the center is the plume and the red light above it is produced by the heater placed over the substrates.

Its appeal is due to the great adaptability and procedure simplicity; over the years thin films of many different materials, from oxides to intermetallics, have been prepared thanks to PLD. Along with other PVD methods, the apparatus involves a dense target from which material is ablated and a substrate, on which thin films are deposited and grow. The interaction between the laser's photon energy and the target removes materials from the bulk's surface. Significant removal of material occurs at a precise power density that depends on the laser wavelength, pulse duration and the target's absorption properties [162]. One of the biggest benefits that make PLD very useful for complex structures deposition, is that the composition is maintained from the target to the film since it produces a stoichiometric transfer of material. The stoichiometric deposition occurs thanks to the complex physical processes happening during the ablation and this characteristic is rarely found for other deposition techniques. The ejected material turns into a plasma and forms a bright ablation plume directed to a substrate where it re-condenses, forming a thin film with the same stoichiometry as the target material. It's possible to carry out the process in an ultra-vacuum atmosphere or in the presence of a background gas such as oxygen, which is commonly used to deposit oxides. The crucial step is the plasma generation generated by the interaction with the laser; plasma forms with the typical

feather-shape, and it is called plume. Inside the plume, the just-ablated material is found in form of single atoms, that are collectively and simultaneously removed from the target surface, regardless of the physical-chemical properties of the individual elements, allowing a stoichiometric deposition.

3.2.1.1   LASER

Figure 34 - Laser types with distinct laser lines are shown above the wavelength bar, while below are shown lasers that can emit in a wavelength range. The height of the lines and bars gives an indication of the maximal power/pulse energy commercially available, while the colour codifies the type of laser material. For semiconductor lasers a solid fill shows the powers achievable with a single emitter, while horizontal lines indicate bars or stacks of bars [163].

LASER stands for Light Amplification by Stimulated Emission of Radiation. It is a device that emits a coherent and convergent monochromatic beam of light with a wavelength ranging from UV to IR through the process of stimulated emission. All the existing types of lasers can be classified either by the emission wavelength or by the active medium that produces light amplification (Figure 34 [163]). For PLD applications, the typical wavelength range is between 200 and 400 nm, since most compounds exhibit strong absorption in the UV spectrum. The most common lasers for PLD are gas excimer (typically KrF and ArF) and Nd:YAG (Neodymium doped-Yttrium-Aluminum-Garnet) solid-state types.

A laser can produce a focused power ranging from a few mW to 100 kW with a precise spot size and interaction/pulse time of 10^{-3}- 10^{-15} s on a wide range of materials and through any medium [164]. Its coherence, spectral purity, and ability to propagate in a straight line are distinctive properties with respect to other electromagnetic radiations. Lasers are classified according to the lasing medium in gas lasers (excimer), solid-state lasers (Nd:YAG, neodymium-doped yttrium aluminium garnet), liquid lasers and semiconductors lasers (e.g. diode laser).

Since their discovery in the 1960s, lasers are widely used in an extraordinary variety of fields, from routine applications such as bar code scanners or printers to life-saving (surgery) and purely scientific (spectroscopy). During the 1990s, lasers were explored for surface applications such as alloying, cladding and thin film deposition.

The laser instrumentation in usage at Shibaura IT is a *Lotis TII Nd:YAG LS-2145N* . The stimulated emission from the excited energy levels of the Nd^{3+} ions in the YAG crystal rod is at the basis of the radiation's generation. The source pump is a *Heraeus Noblelight* lamp. A UV radiation is needed to obtain a sufficient absorption from the target material since the absorption peaks fall within the range of 200-400 nm, so, even if the radiation wavelength related to the concerned transition of the laser corresponds to 1064 nm, named Fundamental Frequency (FF), that is not used for PLD purposes. To obtain an effective radiation that can interact with the material, we need to quadruplicate the frequency of the fundamental transition, with the resulting radiation being named Fourth Harmonic (FH). The fourth harmonic generation can be accomplished by locating a Non-Linear-Optic crystal (NLO) along the optic path of the photons. By interacting with the NLO crystal, two photons with λ=1064 nm combine into one photon with half of the original wavelength λ=532 nm. The resulting doubled-frequency radiation, Secondary Harmonic (SH), enters another NLO crystal, where the other two photons combine

into one with λ=266 nm, generating the fourth harmonic radiation. After the frequency generation element, a wavelength separator is needed to select the desired radiation [165,166]. In the aforementioned laser equipment, a Potassium Titanyl Phospate (KPT) crystal and a Barium Borate (BBO) crystal were used for the SH and FH generation, respectively [167].
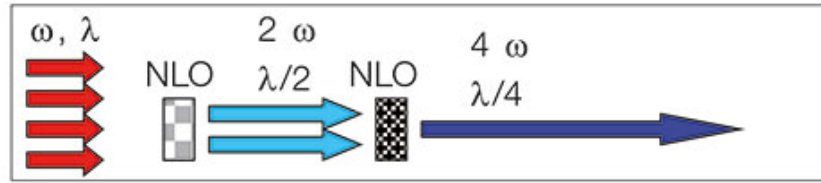
Figure 35 - Fourth Harmonic generation mechanism through NLO crystals [165].

Apart from the main components that grant the laser radiation production, another element is strictly required in the laser equipment: the pulse generation system. PLD technique, as the name suggests, relies on laser pulses, which must be short and powerful to ablate material from the target surface. If the laser operated in constant wave conditions, the power output would be too low to favourably interact with the material. The common strategy to obtain short pulses is the so-called Q-switching technique. In the case of the present laser equipment, a KDP (Potassium-dihydrogen-phosphate) Pockels cell provides the Q-switching mode, acting like an optic switch [167, 168]. Pockels cells are optical-electronic devices that convert the light polarization, from linear to circular, using a potential difference.
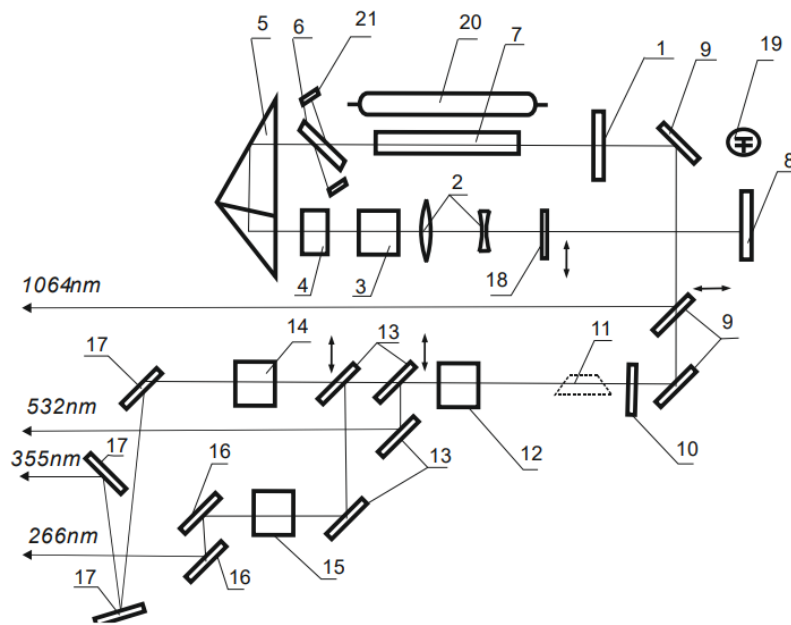
Figure 36 - Optical diagram of the laser cavity [167].

To finely regulate the laser path inside the laser head, a very complex system of mirrors, lenses and wave separators is used. The optical system inside the laser is displayed in Figure 36. The straight lines represent the different paths of the laser beams, depending on the selected wavelength, since, as described before, four different frequencies can be generated with this kind of equipment. The main components are the flash lamp (20), the active element (7), the Q-switching element (12), the mirrors (9, 10) and the wave separators (13, 16, 17).

After the selection of the required wavelength, the beam exits from the laser head. Then, its path can be changed by means of a mirror in order to choose the selected vacuum chamber. In Figure 37, the laser path is reported.
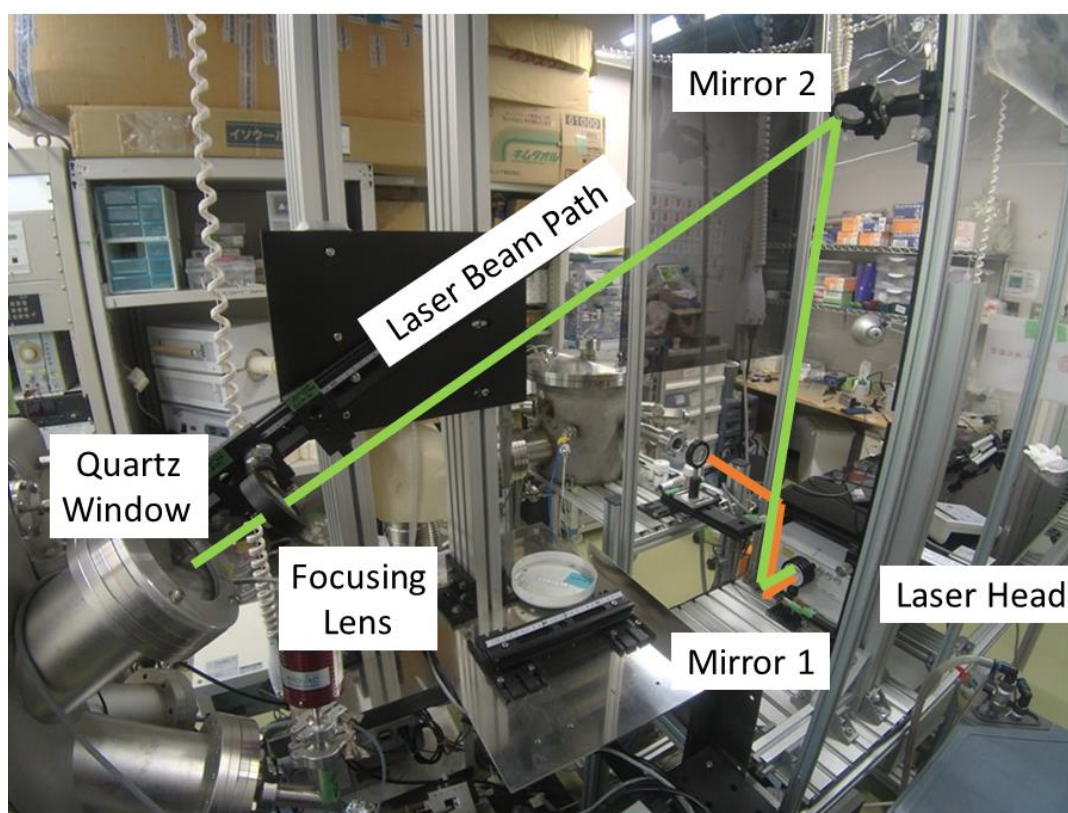
Figure 37 - Laser beam paths. orange) to the small chamber dedicated to oxides' deposition; green) the big chamber dedicated to skutterudites.

3.2.2 Growth Mechanism of a Thin Film

Many properties of a thin film, such as optical, electronic, mechanical performances, are enormously affected by the microstructure features of the sample, such as texture, grain size, thickness, grain orientations, and so on. Physical properties of a solid are also majorly

influenced by defects, intrinsic (caused by atoms that are not changing the stoichiometry of the crystal) or extrinsic ones (that produce non-stoichiometry) [169]. Thus, understanding the different mechanisms influencing the growth mode is necessary to control the surface morphology during thin film growth.

The growth of thin films by physical vapour deposition is an exceptional nonequilibrium procedure and, therefore, the number of defects in thin film material might surpass that in bulk solids up to 5 orders of magnitude more. The motivation why film properties differ significantly from bulk ones rises from the fact that, because the real structure of thin films is far away from its energetic minimum, it usually involves crystals full of defects divided by grain boundaries rich in impurities, as visible in Figure 38 [169].
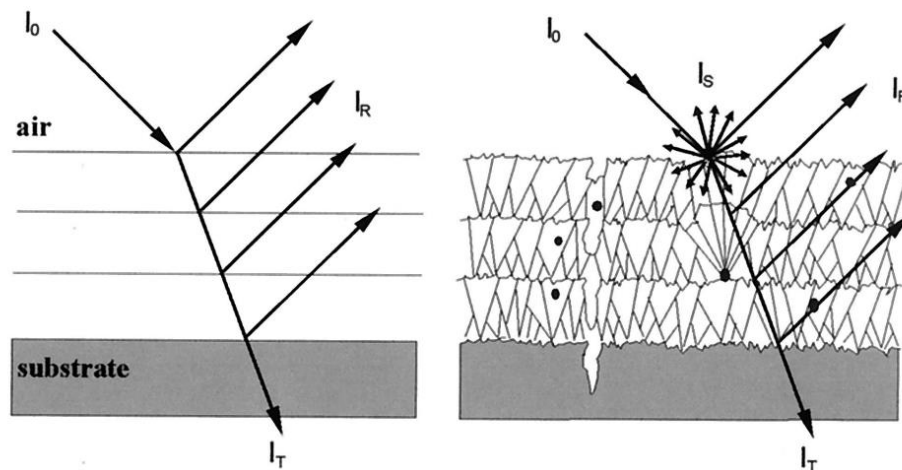
Figure 38 – On the left, the ideal single-crystal film grown on a single-crystal substrate. On the right, a more realistic situation full of defects. A representation of reflection and transmittance of the light is shown through the black arrows [169].

During the initial phase of film deposition, an adequate number of vapour atoms from a supersaturated gas-phase condenses and permanently set up on the substrate. This process is the so-called nucleation stage and from this point onwards the nuclei will grow and crystallization will take place. Afterwards, the exposure of the substrate to the incident vapour or plasma, a uniform distribution of tiny but extremely mobile clusters or islands takes place. The next stage involves the unification of the islands by a coalescence event that can be liquid-like, especially at high substrate temperatures [170,171].

The consequent film formation is ruled by two main factors, which are bondings between atoms of the materials together and with the substrate and the lattice mismatch between
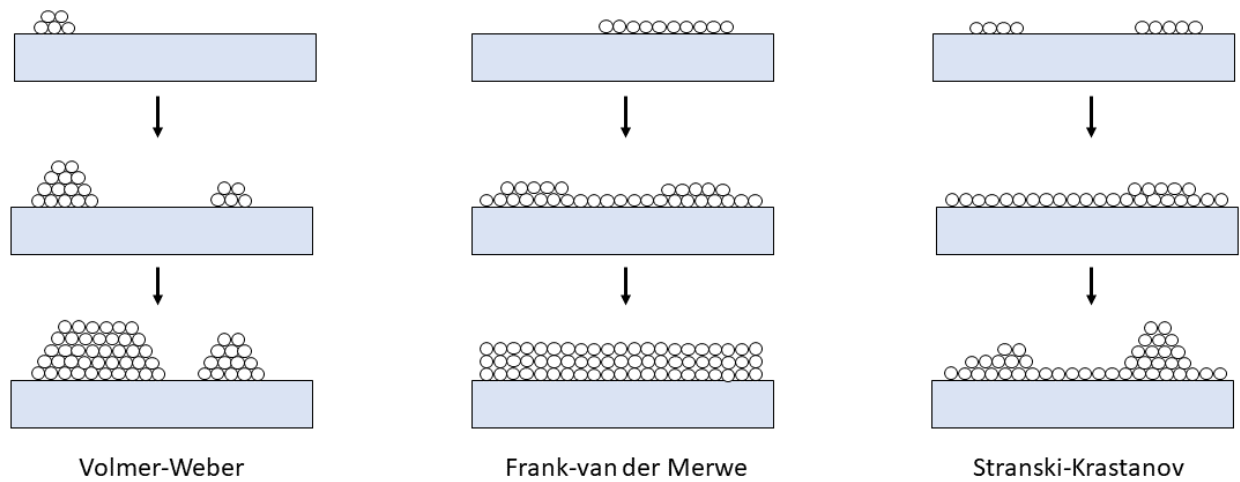
Figure 39 - The three basic thin film growth mechanisms.

the two of them. Three main different growing mechanisms were categorized (Figure 39) [170,172]:

1 – The Volmer-Weber process or islands growth occurs when the small stable clusters nucleate on the substrate and grow in three dimensions to create islands. This occurs when atoms of the deposited material bond more strongly with each other rather than with the substrates. Surface tension is high and the noticeable lattice mismatch of these films in the initial stage make this process undesirable for epitaxial films. Anyway, it can be of interest for the synthesis of self-organized zero-dimensional quantum dots. Metals and semiconductors on oxide substrates usually follow this route;

2 – The Frank-Van der Merwe process or layer growth is the opposite mechanism. In this case, the atoms bond to the substrate more strongly than to each other. The enlargement of the smallest stable nuclei takes place all over in two dimensions, giving rise to the formation of planar sheets. The stress from lattice mismatch is low, resulting in the growth of smooth films layer by layer. The first complete monolayer is then covered by a less bounded second one. The most recognized and significant example for this process is the single-crystal epitaxial growth of semiconductor thin films;

3 – The Stranski-Krastanov process or layer plus islands growth is an intermediate mechanism of the aforementioned two modes. It takes place when surface tension and lattice mismatch are in between the ones for Volmer-Weber and Frank-Van der Merwe progressions. In the first step, one or more monolayers are formed, and consequently, this route becomes unfavourable. The strain energy will decrease giving rise to the formation of islands. Such a

growth process gives origin to polycrystalline films if the film exceeds the critical limit. It is quite common and it has been observed in metal-metal and metal-semiconductor couples.

3.3 Measurement of Thermoelectric Properties

3.3.1 Electrical Conductivity and Seebeck Coefficient

The ULVAC ZEM-3 system is based on the simultaneous measurement of the electrical resistivity and the Seebeck coefficient. The analysis of the thermoelectric properties was carried out in the laboratories of the National Institute of Material Science (NIMS), Tsukuba (Japan), in the laboratory of Professor Takao Mori.
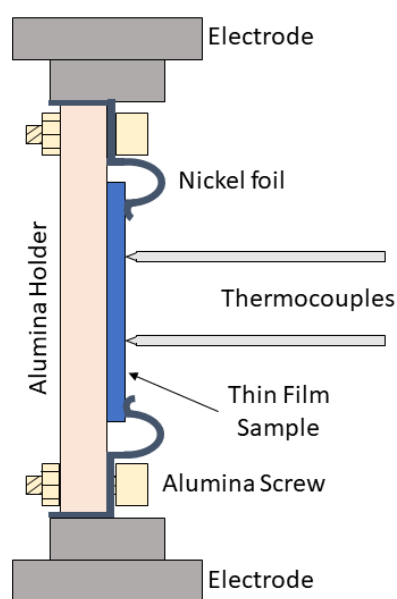
Figure 40 - On the left, side view of the experimental custom-made set-up for the thermoelectric properties' measurement of thin films. On the right, a picture of skutterudite thin film on the special holder is shown.

Typically, the ZEM-3 device is used for bulk materials, hence, some modifications to the experimental apparatus were necessary to make it compatible with the measurements of the thin films. In Figure 40, a schematic representation of the rearranged set-up and a real photo is reported.

The thin film is set up on the alumina holder by means of two nickel foils, which electrically connect the skutterudite to the electrodes. Moreover, two thermocouples are pressed against the surface of the film with manual control, and they work both as temperature detectors and electrodes. The sample holder uses a distinctive balance contact mechanism, permitting measurement of high reproducibility. *V-I* plot measurement can be made to judge if all the contacts are stable. The system automatically examines whether the contact of the two probes with a sample ohmic or not, and finds and uses the best value of electric current to determine

the resistivity of the sample without the influence of heat transfer. Measurement is controlled by a computer, permitting automatic measurement with each temperature difference at a specified temperature. The whole system is located in a furnace which is evacuated by a rotary pump and filled in with a partial pressure of helium, which is found to stabilize the measurement.

The electrical resistivity is measured by the four-probes method, where a constant electrical current I is applied within the sample through the Ni foils, and the voltage drop dV is measured between the same wires of the thermocouples, used as electrodes, subtracting the thermo-electromotive force between leads. The resistivity ρ is then automatically calculated by the software, which was previously required to insert the dimensions of the sample, by means of the Ohm's Law:

$$\rho = \frac{V \cdot w \cdot t}{I \cdot l} \tag{16}$$

where V is the voltage, w is the film's width, t is the film's thickness, I is the imposed current and l is the film's length.

The Seebeck coefficient is measured by applying a temperature gradient by means of one of the two bulk electrodes, working as a heater. The temperature is measured by both thermocouples and, when the ΔT is stabilized, the voltage induced by the thermal gradient is measured. Measures are repeated four times (both ρ and S) at different precise ΔT decided by the user, and the software will automatically calculate the average of values and display the output data on a file. The Seebeck coefficient can be expressed as the previous Equation 2, reported here again for sake of clarity:

$$S = \frac{\Delta V}{\Delta T} \tag{2}$$

3.3.2   Time-Domain ThermoReflectance (TDTR)

Measuring the thermal conductivity of materials is of practical importance in developing innovative materials with required thermal properties for numerous applications, including energy conversion and storage, electronics, and photonic systems. Over the past two decades, ultrafast laser-based time-domain thermoreflectance (TDTR) has been developed and advanced

as a reliable, powerful, and adaptable technique to measure the thermal properties of an extensive range of bulk and thin film materials [173].

The apparatus used to measure cross plane thermal conductivity for the purpose of this doctoral thesis is described by T. Baba et al [174] and belongs to Professor Takao Mori's laboratory at the National Institute of Material Science (NIMS), Tsukuba (Japan). Principles are also described by G. Latronico et al [175,176]. In addition, its geometrical configuration is shown in Figure 41.
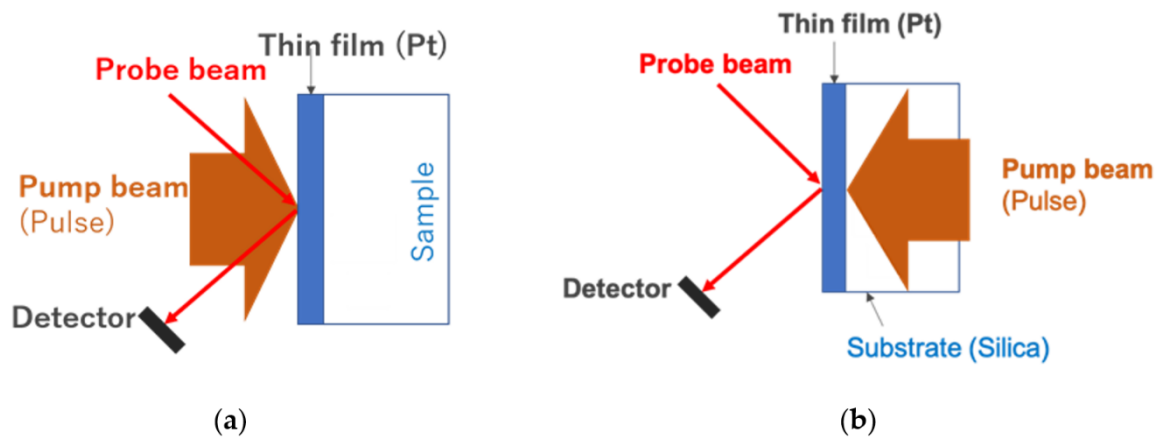
Figure 41 - Diagram of thermo-reflectance measurement with (a) front heat-front detect (FF) configuration and (b) rear heat-front detect (RF) configuration [175].

The reflection of the laser beam incident on the surface of the sample is detected in order to measure its temperature. A second laser beam is directed on the film to heat up its surface. Two configurations are possible. In the case of the rear heat-front detect (RF) configuration (Figure 41b), the probe beam hits the anterior surface of the thin film, while the pulsed pump beam is directed onto the opposite face of the thin film across the transparent substrate. The thickness has to be known and the heat diffusion time across the film is measured in the RF configuration. Then, the thermal diffusivity of the film is directly calculated from the heat diffusion time and the film thickness. In the other configuration, called front heat-front detect (FF) configuration, is the fundamental difference from the front heat-front detect (FF) configuration, the temperature cooling is observed after pulse heating, which is mainly dominated by the thermal effusivity of the film and the substrate.

For this work, T. Baba from NIMS, Tsukuba (Japan) measured thin films deposited on the transparent substrate with a custom-made picosecond pulse light heating thermo-reflectance apparatus (PicoTR, PicoTherm Corporation) and the block diagram on the system is shown in Figure 42. The equipment consists of a fiber laser for the pump beam and another one for the

probe beam. The wavelength of the pump beam is 1550 nm and that of the probe beam is 775 nm, which is generated by a second harmonic generator (SHG).

Regarding the complex calculation part for the treatment of data, the Fourier expansion analysis was applied to the thermo-reflectance signals by taking into account the periodicity of pulse laser heating, which is not possible by conventional methods.

By a mathematical model called mirror image method, it is possible to determine the thermal effusivity of the sample b_s. thus, it is possible to find the thermal conductivity of the samples κ_s using the following equation:

$$\kappa_s = \frac{b_s^2}{c_s \rho_s} \tag{17}$$

where c_S and ρ_S are the specific heat capacity and density of the sample layer, respectively.
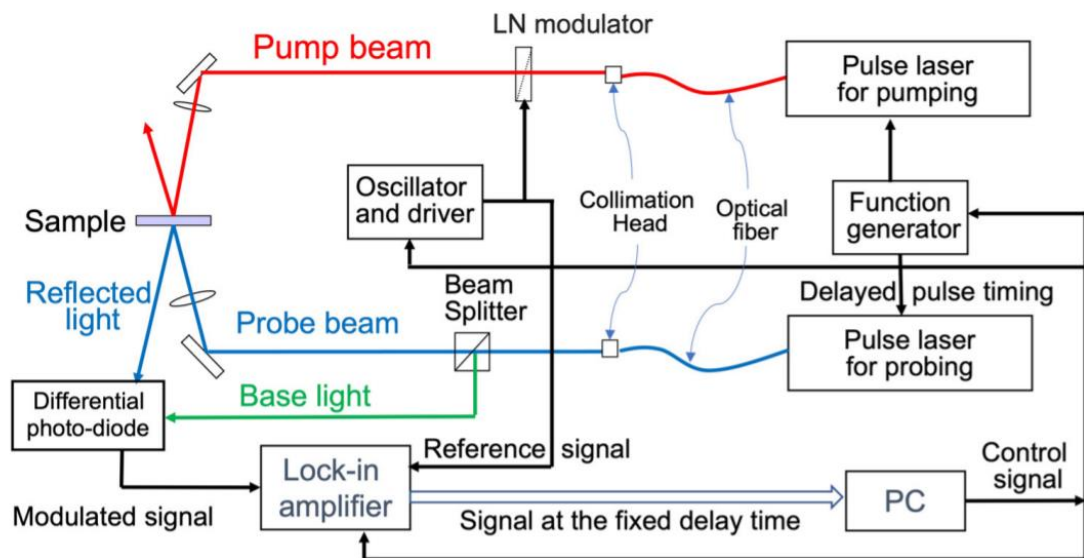
Figure 42 - Block diagram of the picosecond thermo-reflectance measurement system [176].

4   FILLED SKUTTERUDITES THIN FILMS

4.1 Investigation on the Power Factor of Skutterudite $Sm_y(Fe_xNi_{1-x})_4Sb_{12}$ Thin Films: Effects of Deposition and Annealing Temperature

Filled skutterudites are currently studied as promising thermoelectric materials due to their high power factor and low thermal conductivity. The latter property, in particular, can be enhanced by adding scattering centres, such as the ones deriving from low dimensionality and the presence of interfaces. This study focused on the synthesis and characterization of thin films belonging to the $Sm_y(Fe_xNi_{1-x})_4Sb_{12}$ filled skutterudite system. Films were deposited under vacuum conditions by the Pulsed Laser Deposition (PLD) method on fused silica substrates, and varying the deposition temperature. The effect of the annealing process was studied by subjecting a set of films to thermal treatment for 1 h at 423 K. Electrical conductivity σ and Seebeck coefficient S were acquired by the four-probe method using a ZEM-3 apparatus performing cycles in the 348-523 K temperature range, recording both heating and cooling processes. Films deposited at room temperature required three cycles up to 523 K before being stabilized, thus revealing the importance of a proper annealing process in order to obtain reliable physical data. XRD analyses confirm the previous result, as only annealed films present a highly crystalline skutterudite not accompanied by extra phases. The power factor of annealed films results to be lower than in the corresponding bulk samples due to the lower Seebeck coefficients occurring in films. Room temperature thermal conductivity, on the contrary, shows values comparable to the ones of doubly-doped bulk samples, thus highlighting the positive effect of interfaces on the introduction of scattering centres, and therefore on the reduction of thermal conductivity.

The reasons behind the study of skutterudite thin films are therefore two-fold: on one hand, a basic science motivation leads us to investigate the effect of low dimensionality and the presence of interfaces, which make thin films particularly interesting as a source of further phonon scattering [47,48]. On the other hand, from a technological point of view, it is desirable to produce flexible and robust TE devices, able to harvest heat from curved or irregularly shaped surfaces, overcoming the flat, bulky, and fragile commercial TE devices. Nevertheless, in spite of the relevance of these issues, very few literature works are devoted to the deposition of

skutterudite thin films and to their characterization, and almost all of them deal with $CoSb_3$ [49,50] and $CoSb_3$-deriving compounds [47,51,52].

4.1.1   Materials and Methods

4.1.1.1   Preparation of porous samples and dense targets

Two compositions of the $Sm_y(Fe_xNi_{1-x})_4Sb_{12}$ filled skutterudite system were prepared by the conventional melting-quenching-annealing technique with nominal (x = 0.63; y = 0.20) and (x = 0.70 y = 0.40), being the former at the n/p crossover, and the latter p-conducting, respectively [142]. The Sm content was chosen based on the results described in [42]. Besides, Sb was added in a slight excess compared to the stoichiometric quantity in order to compensate for the possible loss caused by its non-negligible vapour pressure (0.133 Pa at 873 K [177]). Small pieces of pure elements (Fe, Alfa-Aesar, 99.99 wt.%; Ni, Alfa-Aesar, 99.99 wt.%; Sm, NewMet; 99.9 wt.%; and Sb, Mateck, 99.99 wt.%) were weighted in due amount and placed under vacuum in quartz tubes. The mixtures were then thermally treated at 1223 K for 1 hour to ensure the homogenization of the liquid phase, and then hastily cooled in a water bath to improve microcrystallinity and facilitate the subsequent annealing process. As-cast samples were then annealed in a vacuum at 873 K for 7 days in order to promote the formation of the desired phase and subsequently ground in a mortar operating within an Ar-filled glovebox in order to prevent oxidation.

The sample with x = 0.63 was densified by spark plasma sintering (SPS, home-made machine at the University of Pavia, Italy) at 773 K for 5 minutes under a pressure of 50 MPa. Discs' diameters range between 1 and 1.5 cm, depending on the availability of the starting material. Targets of specimens with x = 0.70 were prepared by the open die pressing technique (ODP, at CNR-ICMATE in Lecco, Italy). Powders were encapsulated into an iron sleeve; the inner surface was covered with a layer of BN to prevent sticking and to facilitate the sample removal after the process. The specimen was preheated at 773 K for 3 minutes and pressed with its axis horizontally oriented between two heated plates of a hydraulic press. The dense sample is provided with a characteristic shape, giving the possibility to obtain two distinct targets. Samples are named Fe63 and Fe70, depending on Fe % amount with respect to the total (Fe + Ni) content.

4.1.1.2   Characterization of porous samples and dense targets

Morphology and composition of both porous and dense samples were studied by electron microscopy coupled to energy-dispersive x-ray spectroscopy (SEM-EDS, Oxford Instruments, Abingdon, UK, model 7353 with Oxford-INCA software v. 4.07, Link Analytical – Oxford Instruments, Abingdon-on-Thames, UK, working distance: 15 mm, live time: 40 s): to this purpose, small pieces were encapsulated in resin and micrographically polished prior to being analyzed. EDS analyses were performed on at least five points for each selected area. Microhardness of porous samples was measured by means of a Leica VMHT microhardness tester (Leica, Wetzlar, Germany) provided with Vickers indenter. A test load of 50 g was applied with a dwell time of 15 seconds; 10 tests were performed on each sample.

Powders obtained from grinding bulk porous samples were analyzed through x-ray diffraction by a Bragg-Brentano powder diffractometer (Philips PW1050/81, Amsterdam, The Netherlands, Fe-filtered Co Kα radiation, power settings: 30 mA, 40 kV) making use of a zero-background sample holder in the 20°-110° angular range.

4.1.1.3   Deposition of thin films

Filled skutterudite thin films were grown by the pulsed laser deposition (PLD) technique using a fourth harmonic of Nd:YAG (266 nm, 10 Hz) laser (LOTIS TII, Minsk, Belarus). Squared silica pieces were chosen as substrates, undergoing firstly a cleaning process at 773 K for 2 h, and being then glued by means of silver paint on an Inconel plate which was then inserted into the PLD chamber. The laser was shot on the dense Fe63 and Fe70 targets with an energy density of about 4.2 J/cm^2 for a deposition time of 60 minutes under a high vacuum (10^{-4} Pa). Films were deposited both at room temperature and at 423 K, and a set of the former batch was subjected to an annealing process at 423 K for 1 h under a flux of argon gas (200 cm^3/min). Films are named Fe63_RT, Fe70_RT, Fe63_423, Fe70_423, Fe63_ann, Fe70_ann according to the Fe amount, as previously elucidated, and to the process, the sample was subjected to: RT (deposition at room temperature), 423 (deposition at 423 K), ann (annealed). In Table 1 an overview of the experimental conditions of films deposition is reported.

Table 1- Experimental conditions of the thin films' depositions.

Sample	Deposition Temperature [K]	Deposition time [min]	Target-Substrate Distance [mm]	Annealing [min-K]
Fe63_RT	293	60	35	-
Fe63_423	423	60	35	-
Fe63_ann	293	60	35	60 - 423
Fe70_RT	293	60	35	-
Fe70_423	423	60	35	-
Fe70_ann	293	60	35	60 - 423

4.1.1.4   Characterization of thin films

Morphology and composition of thin films surfaces were studied by electron microscopy coupled to energy-dispersive X-ray spectroscopy (SEM-EDS, JEOL/JSM-7100F, Akishima, Japan) to this purpose, the surface of the films was coated with gold prior to being analyzed. EDS analyses were performed on at least five points for each selected area. The thermoelectric parameters, such as electrical conductivity σ and Seebeck coefficient S, were concurrently measured by the four-probe method between 348 and 523 K using a ZEM-3 (ULVAC Advance-Riko, Chigasaki, Japan) apparatus under a partial He pressure to assure the thermal transport between the heater and the sample. The thickness of samples was evaluated by means of a Dektak 6M Stylus profilometer (Bruker, Billerica, MA, USA).

All samples were subjected to the x-ray diffraction analysis, both before and after the thermoelectrical characterization by a Bragg-Brentano powder diffractometer (Smart Lab3 Rigaku Corporation, Tokyo, Japan) using the Cu Kα radiation in the 10° - 100° angular range with angular step 0.02° (power settings: 40 mA, 40 kV).

The picosecond Time-Domain ThermoReflectance (TD-TR) technique using a customized focused thermal analysis system based on PicoTR (PicoTherm, Tsukuba, Japan) was utilized to measure the thermal conductivity of the samples at room temperature in the cross-plane direction [178,179,180,181].

4.1.2 Results and Discussion

4.1.2.1 Morphological, compositional and structural properties of porous and dense samples

The surface of bulk annealed samples appears highly porous, as depicted in Figure 43, where microphotographs taken on both samples by secondary electrons (SE), are shown.
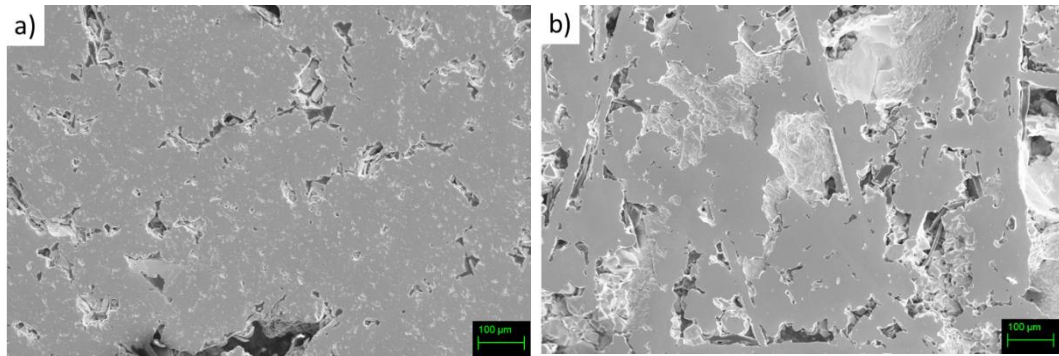
Figure 43 - SE-SEM microphotographs of the polished surface of bulk samples a) Fe63 and b) Fe70 [176].

Backscattered (BS) images and EDS analyses suggest that the main phase is the desired skutterudite, with composition $Sm_{0.17}(Fe_{0.60}Ni_{0.40})_{3.75}Sb_{12}$ and $Sm_{0.38}(Fe_{0.69}Ni_{0.21})_{3.75}Sb_{12}$ for samples Fe63 and Fe70, respectively. Nevertheless, the presence of the additional phase $SmSb_2$, which is commonly found in non-perfectly monophasic samples belonging to this system [182], can be observed too, as can be inferred from Figure 44.
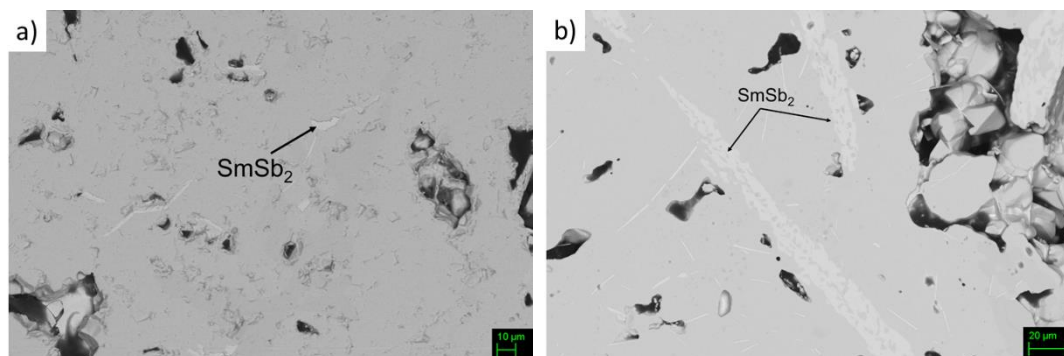
Figure 44 - BS-SEM microphotograph of the polished surface of sample a) Fe63 and b) Fe70 [176].

The presence of the aforementioned additional phase, as well as of a tiny amount of Sb, is confirmed by the results of X-ray acquisitions, as observable in Figure 45.
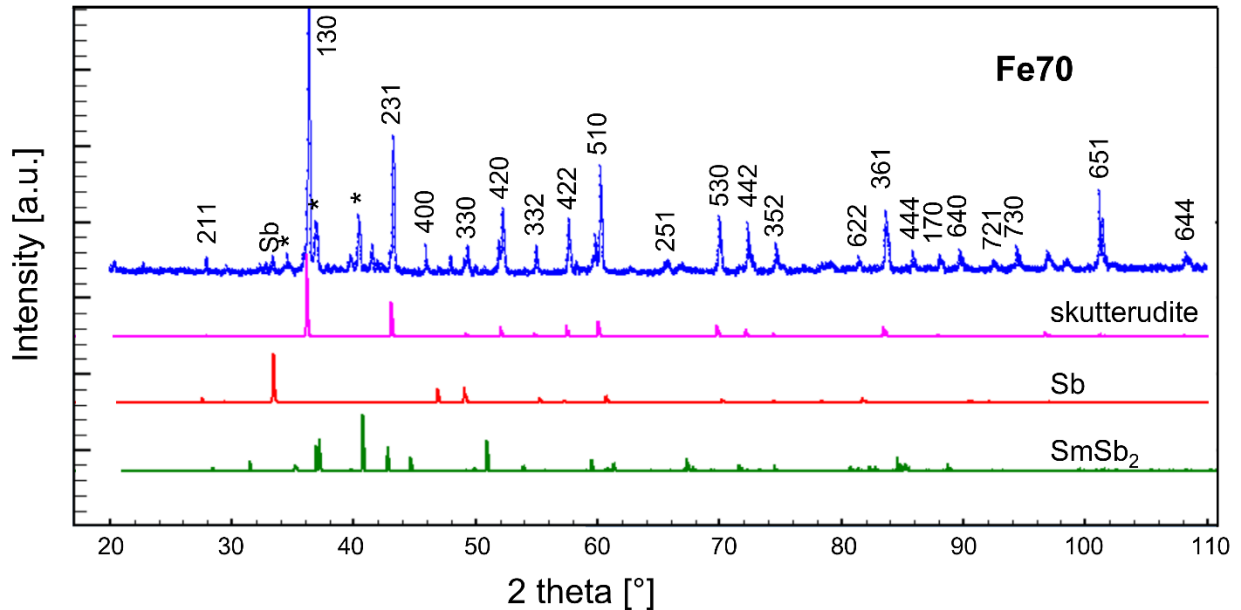
Figure 45 - X-ray diffraction pattern of sample Fe70 and calculated diffractograms of skutterudite, Sb and SmSb₂. In the experimental pattern, Miller indexes of the skutterudite phase are indicated, as well as the position of the main peaks of the additional phases Sb and SmSb₂ (asterisks) [176].

Microhardness was measured at several points of both phases on the Fe70 surface; results clearly show clustering of data around two values, namely 462(23) and 373(14) HV, being the former associated with skutterudite and the latter to the $SmSb_2$ extra phase. Such a value for skutterudite is in good agreement with the ones of samples belonging to the $(Sm,Gd)_y(Fe_xNi_{1-x})_4Sb_{12}$ system [41].
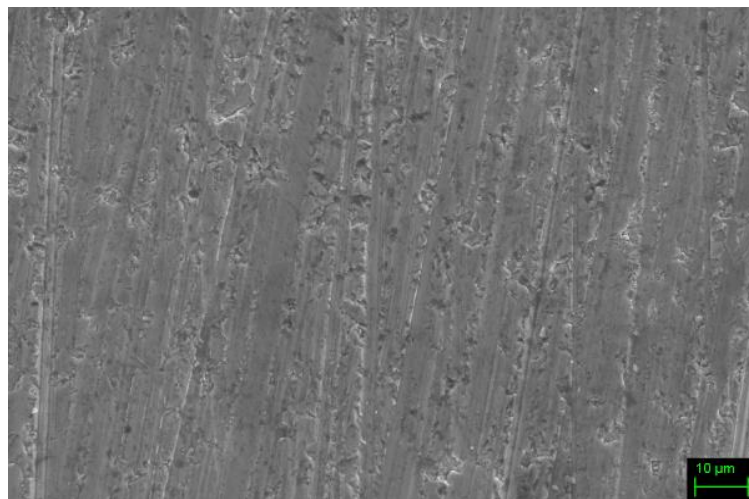
Figure 46 - SE-SEM microphotograph taken on dense Fe70 sample [176].

After the densification process, both compositions show a significant density enhancement, as clearly depicted in Figure 46, presenting the surface of targets as revealed by SE-SEM.

4.1.2.2 Morphological, structural and transport properties of thin films
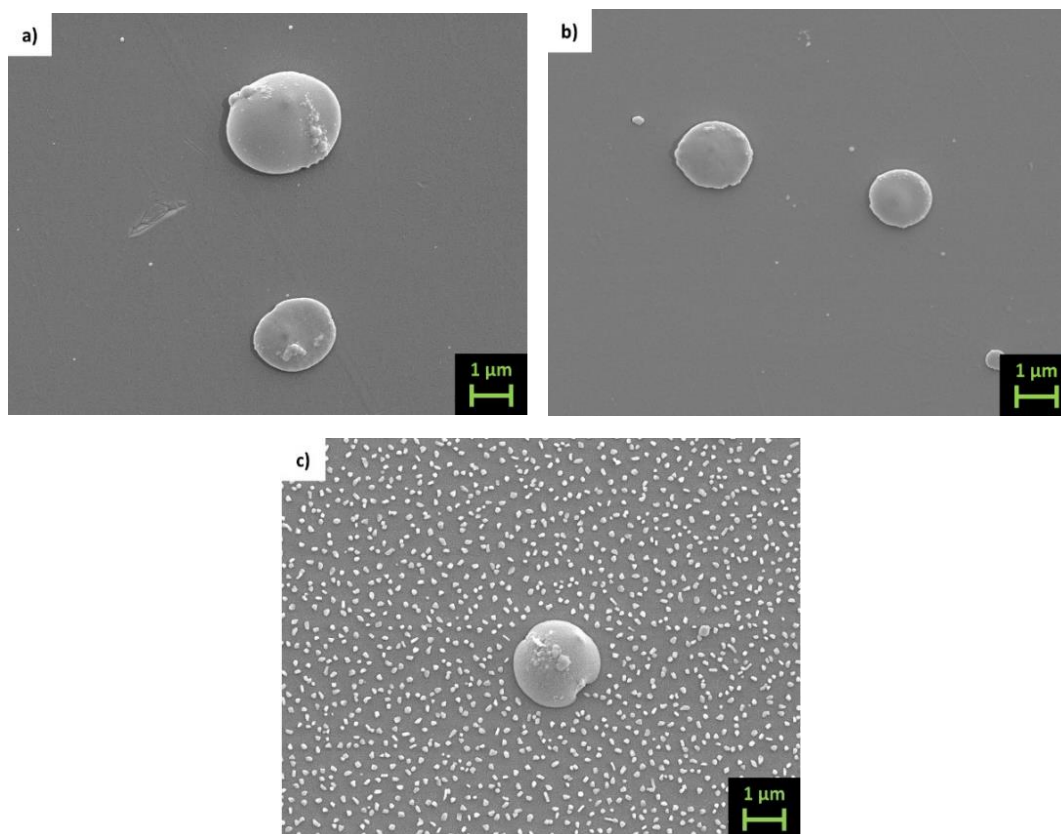
Figure 47 - Top view LED-SEM images of samples (a) Fe63_RT, (b) Fe63_ann and (c) Fe63_423 [176].

The morphology of thin films is shown in Figure 47 and Figure 48, which present LED-SEM photos of the surface of the film.

Films deposited at room and at high temperature present a large difference: while the former (Figure 47 a and b, Figure 48 a and b) show a very smooth texture, the latter (Figure 47c, Figure 48c) present uniformly distributed nanosized grains appearing on the surface of the film. Under a brief analysis with the EDS, they appear richer in Sb compared to the film. As can be inferred from the high magnification image taken on the sample Fe70_ann (Figure 49), the typical grain size of these films is around 20 nm. Analogous morphology can be observed on other samples of both series. On the surface of all films, it is noticeable the presence of drops

with sizes ranging from 1 to 2 μm, typical of films deposited via PLD [183]. In order to reduce this inconvenience as much as possible, a study regarding the dependence of the morphology from the laser energy density is required in the future.
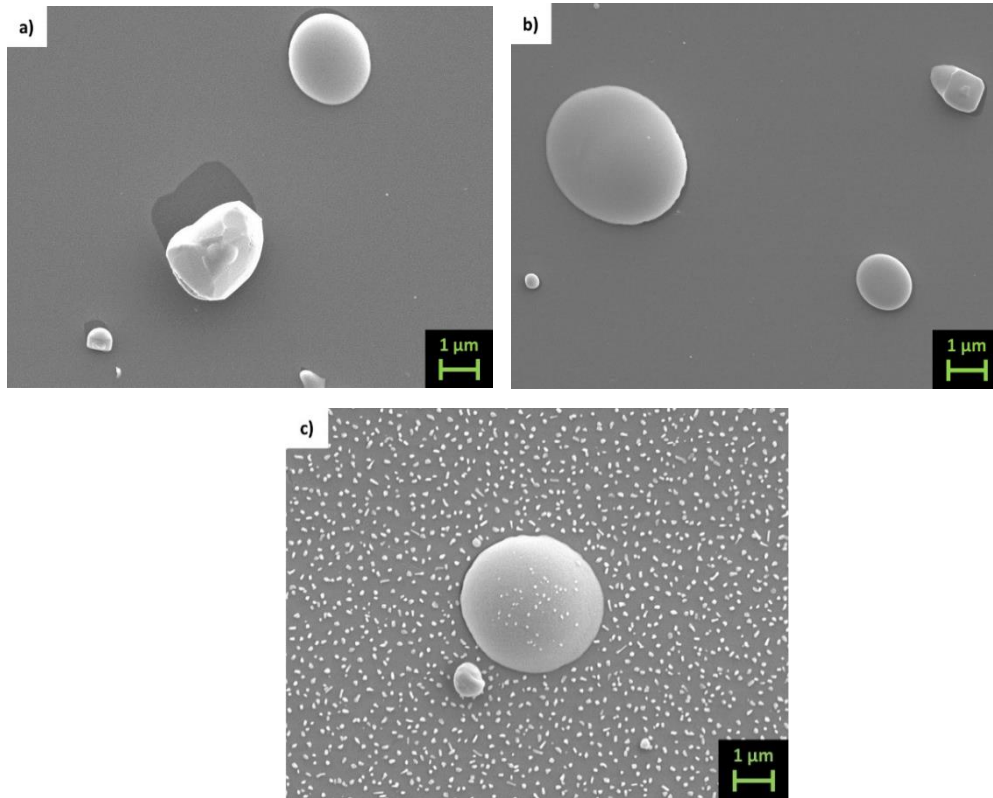
Figure 48 - Top view LED-SEM images of samples (a) Fe70_RT, (b) Fe70_ann and (c) Fe70_423 [176].
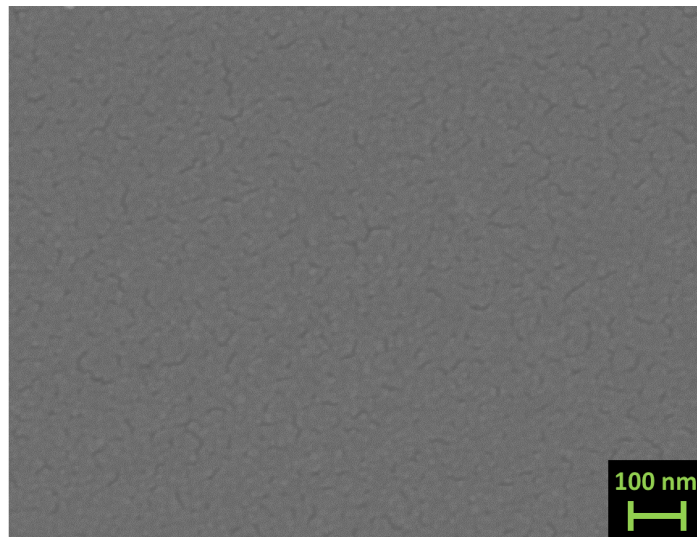
Figure 49 - Top view high magnification (x100k) LED-SEM images of sample Fe70_ann [176].

The X-ray diffraction (XRD) patterns collected on the three films belonging to the Fe70 series are presented in Figure 50; analogous behaviours are shown by the Fe63 series. Both

samples as-deposited at room temperature (Fe63_RT and Fe70_RT) result to be mostly amorphous. After undergoing the annealing process, both films (Fe63_ann and Fe70_ann) exhibit the peaks corresponding to the skutterudite structure, indicating the formation of a crystalline structure. It has to be noticed that, at variance with bulk samples, annealed films present only the desired skutterudite phase and not additional ones. Contrariwise, samples deposited at 423 K (Fe63_423 and Fe70_423) show both skutterudite and undesired additional phases, such as Fe-Ni antimonides, or residual free Sb, similarly to bulk samples.
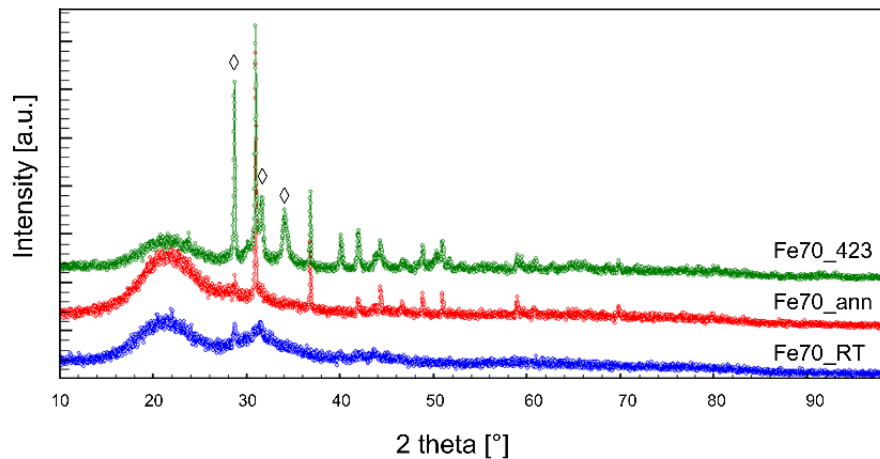
Figure 50 - X-ray diffraction patterns of films belonging to the Fe70 series (◊ refers to the secondary phases Sm and SmSb$_2$) [176].
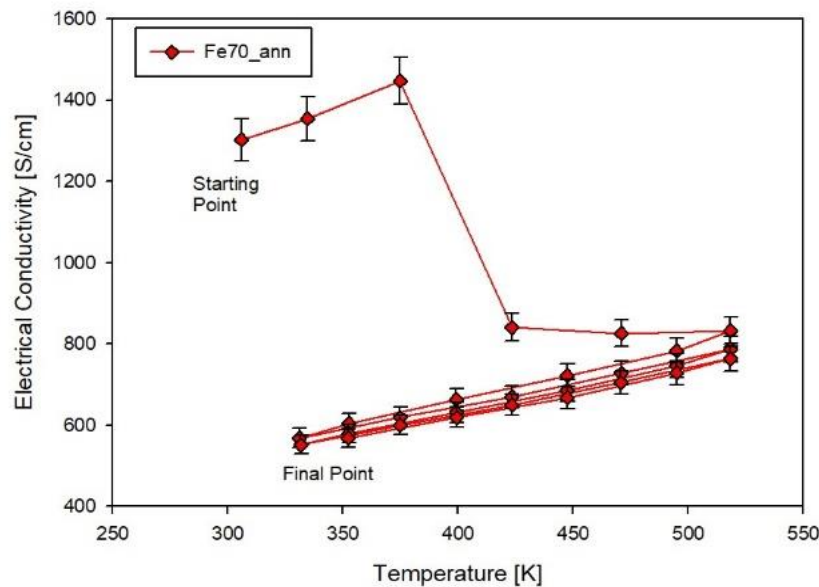
Figure 51 - Electrical conductivity measurement cycles performed on sample Fe70_ann. Lines are guides for the eye [176].

The importance of the annealing process is illustrated by the electrical conductivity measurements cycling. As depicted in Figure 51, representing the σ measurement of sample Fe70_ann, it is clearly visible that during the first heating up to 523 K, the σ drop suddenly
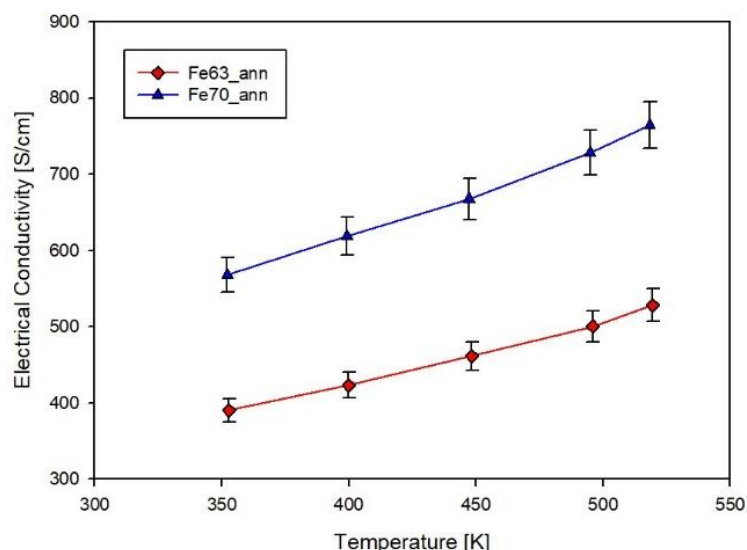
Figure 52 - Trend of the last cycle of the electrical conductivity as a function of temperature for samples Fe63_ann and Fe70_ann [176].

around 325-425K to a lower σ range attesting of a remain instability of the annealed films during the measurement. However, after the first heating cycle, the σ became perfectly reproducible; all samples follow this trend. It is highly likely that the first temperature cycle acts as a further annealing process, which promotes the obtainment of a higher crystallinity degree, even if the appearance of new phases was not observed. As a consequence, only results deriving from annealed films will be hereinafter considered.

Data reported in Figure 52, showing the trend of σ vs. temperature for both compositions of annealed films, confirm the semiconducting nature of the samples and the substantial
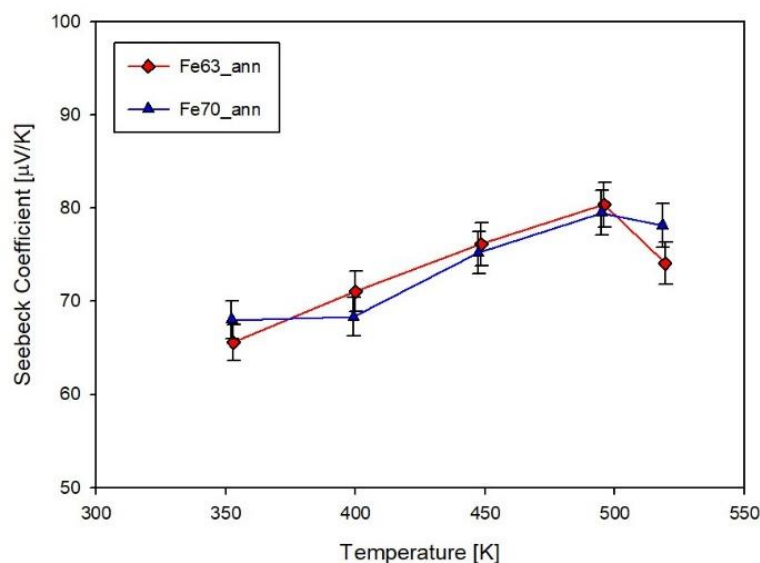
Figure 53 - Trend of the Seebeck coefficient as a function of temperature for samples Fe63_ann and Fe70_ann [176].

74

closeness of their electrical conductivity values. A comparison with data of the $(Sm,Gd)_y(Fe_xNi_{1-x})_4Sb_{12}$ skutterudite [41] indicates that the present σ values are not far from the ones of dense samples with x = 0.8, while they are significantly higher than those of Sm-filled bulk samples [184].

The Seebeck coefficient *S* is presented in Figure 53 as a function of temperature for both annealed films. The two compositions present very similar data and result to be p-conducting, with values remarkably lower than the ones of (Sm,Gd)-filled compositions [41] and of Sm-filled bulk samples [184]. In comparison with thin films, the Sm-filled skutterudite bulks present a larger size of the grains (72~307 nm), and lower density, (82%~97%) depending on composition and on the applied sintering pressure, according to the calculations reported in [142]. The larger size of the grains and relatively lower density of the bulks with respect to films could be responsible for a higher electron scattering, which conversely yields higher values of SAs a general remark, it can be observed that both samples exhibit a weak dependence on temperature. As already observed in the two aforementioned cases, even in the present one the trend of *S* vs. *T* shows a maximum at ~500 K, as the measurement extends over a sufficiently broad temperature range.

Table 2 - Thickness, RT and high-T Seebeck coefficient and thermal conductivity of samples Fe63_RT, Fe63_ann, Fe70_RT and Fe70_ann.

Sample	Thickness [nm]	S @ RT [μV/K]	S @ 523K [μV/K]	k [W/m·K]
Fe63_RT	490	71.6	72.7	-
Fe63_ann	300	65.6	74.1	1.91
Fe70_RT	520	1.30	3.68	-
Fe70_ann	200	68.0	78.2	2.21

Making use of the measured σ and *S* values, the power factor ($PF=\sigma S^2$) has been estimated for both compositions, as resulting in Figure 54. As a consequence of the aforementioned maximum in *S*, even in the trend of *PF* a maximum occurs roughly at the same temperature as in *S*. Regarding the absolute values of the two observed maxima, they are 323 $\mu W/m \cdot K^2$ and 466 $\mu W/m \cdot K^2$ for samples Fe63_ann and Fe70_ann, respectively, which are significantly lower than the corresponding data of the (Sm,Gd)-filled skutterudite [41]. The reason behind this behaviour can be found in the cited lower value of the Seebeck coefficient with respect to the dense doubly-doped system [41].

For sake of comparison, the power factor of our films is compared with other skutterudite thin films reported in the literature. It can be observed that our data are comparable with the ones of $Co_{15.82}Sb_{62.04}Te_{22.14}$ [51] and significantly higher than those of Ag-doped $CoSb_3$ [185].

A comparison with thermal conductivity data of (Sm,Gd)-doubly doped [41], even if limited to room temperature data, shows interesting implications. Values of κ of films reported in Table 2 are very close to the ones of the doubly-doped sample with x = 0.50 (κ = 2.16 W/m·K) and only slightly higher than the one of the samples with x = 0.80 (κ = 1.59 W/m·K), where the amount of filling ions and hence of scattering centres, is noticeably higher. This result is very encouraging, as it suggests that the presence of interfaces acts similarly to the introduction of two different filling ions in terms of the creation of scattering centres. It can be therefore hypothesized that better tailoring of the film composition, for instance by introducing more than one filler, or by partly substituting Sb by a proper atom, can lead toward a further reduction of thermal conductivity and an enhancement of *ZT*.

Table 3 shows the thermal properties at room temperature of annealed films. For our samples we considered c_s = 220 J/kg·K and ρ_s = 7360 kg/m^3.
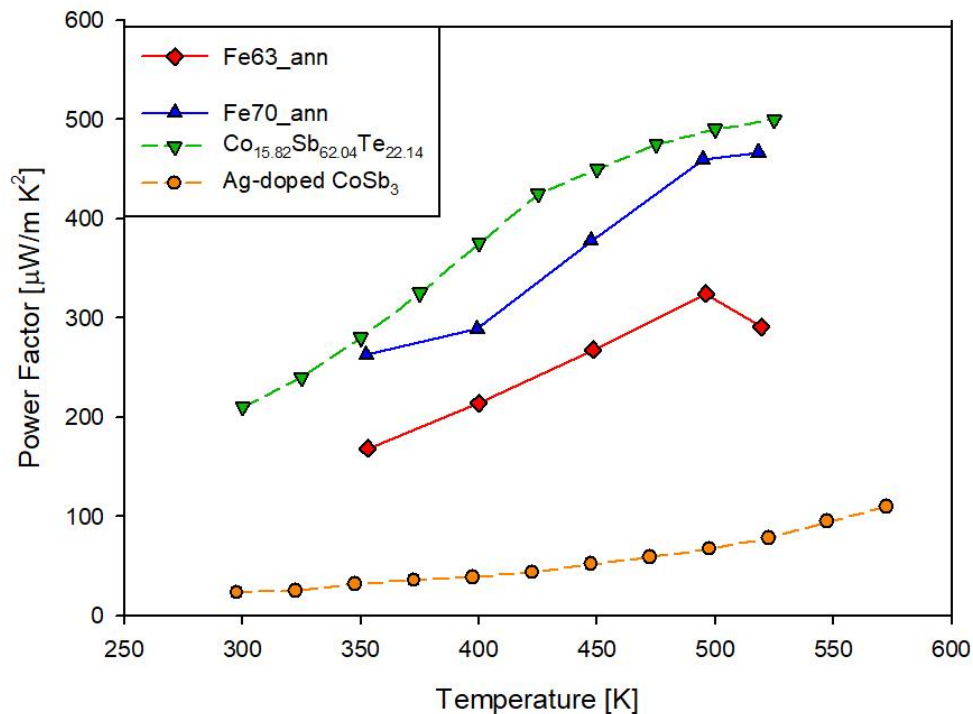
Figure 54 - Trend of the power factor as a function of temperature for samples Fe63_ann and Fe70_ann compared to other samples in literature, namely Co$_{15.82}$Sb$_{62.04}$Te$_{22.14}$ [51] and Ag-doped CoSb$_3$ [185]. [176].

Table 3 - Thermal properties of samples Fe63_ann and Fe70_ann.

Sample	Heat diffusion time τ_f [s]	γ	Thermal Effusivity b_s [J/(s$^{0.5}$m^{2}K)]	Thermal Conductivity κ_s [W/(m·K)]
Fe63_ann	55.5 x 10^{-10}	0.747	1757	1.91
Fe70_ann	6.21 x 10^{-10}	0.717	1890	2.21

4.1.3 Conclusions

In the framework of the optimization of the thermoelectric properties of Sb-based filled skutterudites, thin films of two compositions belonging to the $Sm_y(Fe_xNi_{1-x})_4Sb_{12}$ system were deposited by PLD. The system was chosen because of the promising thermoelectric performance exhibited by the corresponding bulk samples. The cited properties are expected to be improved by the introduction of further scattering centres represented by the low dimensionality and the presence of interfaces, which are typical features of films.

Depositions were performed both at room and at high (423 K) temperature; moreover, the former samples were annealed at 423 K. X-ray diffraction suggests the highest phase purity in annealed samples; accordingly, transport properties values become stable only after three cycles up to 523 K, thus highlighting the importance of the annealing process. Regarding the transport properties of annealed films, electrical conductivity assumes values comparable to the ones of bulk samples, while the Seebeck coefficient results to be strongly lower, which determines lower values of the power factor. Room temperature thermal conductivity is similar in Sm-doped films and in (Gd,Sm)-doped bulk samples, thus suggesting that the presence of interfaces in films acts similarly to the introduction of different filler ions in bulk samples.

4.2 Systematic Study About the Annealing of (Fe,Ni)-Based Skutterudites

As a consequence of the work described in Section 4.1, a systematic study of the annealing of the aforementioned thin films was carried out, in order to find the best conditions to obtain a stable high-performance material. To this purpose, *n*-, *p*- and *n/p* crossover-type samples were deposited via PLD and then underwent an annealing process under argon atmosphere varying temperature and time.

Thermoelectric properties were then measured, and XRD patterns were acquired as well. At the present day, only limited considerations regarding TE properties can be reported here. The calculation of cell parameters as a function of the annealing temperature is in process and Hall effect measurements will be performed soon, in order to have a complete set of data to accurately describe the influence of annealing of the structure and on carriers of the samples.

4.2.1 Materials and Methods

4.2.1.1 Preparation of the material and dense targets

Three compositions of the $Sm_y(Fe_xNi_{1-x})_4Sb_{12}$ filled skutterudite system were prepared by the conventional melting-quenching-annealing technique with nominal (x = 0.50, 0.63, 0.70), being *n*-type, *n/p* crossover, and *p*-conducting, respectively [42], and the Sm content was chosen accordingly. Furthermore, Sb amount has been considered in a slight excess than stoichiometrically necessary with the aim to compensate the possible loss caused by its quite significant vapour pressure (0.133 Pa at 873 K [177]). Small pieces of pure elements (Fe, Alfa-Aesar, 99.99 wt.%; Ni, Alfa-Aesar, 99.99 wt.%; Sm, NewMet; 99.9 wt.%; and Sb, Mateck, 99.99 wt.%) were weighted in due amount and placed under vacuum in quartz tubes. The melting process was carried out at 1223 K for 3 hours to guarantee the homogenization of the liquid phase, and then a rapid quenching in a water bath followed, in order to improve microcrystallinity and simplify the subsequent annealing process. The obtained bulks were then annealed in vacuum at 873 K for 7 days in order to promote the formation of the desired phase and afterwards ground in an agate mortar operating within an Ar-filled glovebox in order to prevent oxidation.

The sample with x = 0.63 was densified by spark plasma sintering (SPS, home-made machine at the University of Pavia, Italy) at 773 K for 5 minutes under a pressure of 50 MPa. Target with x = 0.50 was prepared under the same conditions but with another commercial SPS (Dr. Sinter Lab Jr. Series 322Lx, at NIMS, Tsukuba, Japan). Discs' diameters range between 1 and 1.5 cm, depending on the availability of the starting material. Targets of specimens with x = 0.70 were prepared by the open die pressing technique (ODP, at CNR-ICMATE in Lecco, Italy). Powders were closed into an iron sleeve; the internal surface was covered with a layer of BN to prevent sticking and to facilitate the sample removal after the process. The specimen was preheated at 773 K for 3 minutes and pressed with its axis horizontally oriented between two heated plates of a hydraulic press. The dense sample is provided with a characteristic shape, giving the possibility to obtain two distinct targets. Samples are named Fe50, Fe63 and Fe70, depending on Fe % amount with respect to the total (Fe + Ni) content.

The characterization of porous samples and dense targets were not performed, as targets were the same used for the previous chapter.

4.2.1.2 *Deposition of thin films*

Filled skutterudite thin films were prepared by the pulsed laser deposition (PLD) method using a Nd:YAG (266 nm, 10 Hz) laser. Substrates of silica in a squared shape (1x1 cm^2) underwent initially a cleaning process at 773 K for 2 h in air, and, thenceforward, they were secured to an Inconel plate with silver paint to be then inserted into the PLD chamber. One side of the sample was covered with Kapton tape in order to remove it and be able to measure the thickness later. The laser was shot on the dense targets with an energy density of about 4.2 J/cm^2 under a high vacuum (10^{-4} Pa). Films were deposited all at room temperature for a time of 30 minutes, and they were annealed following different parameters. For each composition, four temperatures (150, 200, 250 and 300 °C) and two times (3 h and 6 h) were investigated, all under a flux of argon gas equal to 200 cm^3/min. A third series was deposited, named series c, for the annealing from 150 to 250°C, with a doubled deposition time (60 minutes) but with a difference in the setting of the PLD holder. Three samples were deposited at the same time, rotating the substrate holder in order to have more homogeneous films. Films are named FeXX_YYYa and FeXX-YYYc if annealed for 3 hours, and FeXX_YYYb if the time was 6h. XX is related to the composition (50,63 or 70) of the target and YYY is the annealing temperature, as described above. For sake of simplicity due to the heavy amount of data, we

decided to keep used of Celsius instead of kelvin in this regarding annealing temperatures). In Table 4 an overview of the experimental conditions of films deposition is reported.

Table 4 - Deposition and annealing parameters and thin films' thickness.

Sample	Deposition T [K]	Deposition time [min]	Annealing T [°C]	Annealing time [h]	Thickness [nm]
Fe50_150a	300	30	150	3	229
Fe63_150a	300	30	150	3	265
Fe70_150a	300	30	150	3	253
Fe50_200a	300	30	200	3	244
Fe63_200a	300	30	200	3	237
Fe70_200a	300	30	200	3	226
Fe50_250a	300	30	250	3	319
Fe63_250a	300	30	250	3	226
Fe70_250a	300	30	250	3	350
Fe50_300a	300	30	300	3	318
Fe63_300a	300	30	300	3	238
Fe70_300a	300	30	300	3	335
Fe50_150b	300	30	150	6	372
Fe63_150b	300	30	150	6	287
Fe70_150b	300	30	150	6	325
Fe50_200b	300	30	200	6	347
Fe63_200b	300	30	200	6	241
Fe70_200b	300	30	200	6	319
Fe50_250b	300	30	250	6	437
Fe63_250b	300	30	250	6	274
Fe70_250b	300	30	250	6	208
Fe50_300b	300	30	300	6	463
Fe63_300b	300	30	300	6	222
Fe70_300b	300	30	300	6	244
Fe50_150c	300	60	150	3	220
Fe63_150c	300	60	150	3	319
Fe70_150c	300	60	150	3	247
Fe50_200c	300	60	200	3	220
Fe63_200c	300	60	200	3	319
Fe70_200c	300	60	200	3	247
Fe50_250c	300	60	250	3	220
Fe63_250c	300	60	250	3	319
Fe70_250c	300	60	250	3	247

Figure 55 - (on the left) Bottom view of the samples in the chamber. They are glued upside down. (on the right) Samples after the deposition. The Kapton tape and the position on the holder are visible.

4.2.1.3   Characterization of thin films

The electrical conductivity σ and Seebeck coefficient S of the a series were acquired by means of custom-made apparatuses (Toyota Technological Institute, Nagoya, Japan), with four-probe methods and steady-state method respectively while thermoelectric properties of the samples belonging to the b series were simultaneously measured by the four-probe method between 348 and 523 K using a ZEM-3 (ULVAC Advance-Riko) apparatus under a partial He pressure to assure the thermal transport between the heater and the sample. The thickness of samples belonging to the a series was evaluated by an optical profilometer Profilm3D (Filmetrics), which gives also the opportunity to obtain a 3D view of the surface of the sample, while the b series were analysed by a means of a Dektak 6M Stylus.

All samples were subjected to the x-ray diffraction analysis, both before and after the thermoelectrical characterization by a Bragg-Brentano powder diffractometer (Smart Lab Rigaku Corporation) using the Cu K_α radiation in the 10° - 100° angular range with an angular step of 0.02° (power settings: 50 mA, 40 kV). The series c underwent to x-ray diffraction analysis using the Cu K_α radiation in the 5° - 100° angular range with an angular step of 0.01° (power settings: 50 mA, 40 kV).

Hall coefficient determination at room temperature was performed on samples as-deposited and annealed at 200 °C of the series c through the usage of a standard 4-terminal method with a commercial PPMS instrument (Quantum Design, San Diego, CA, USA) using an electrical AC current of 5 mA.

4.2.2   Results and Discussion
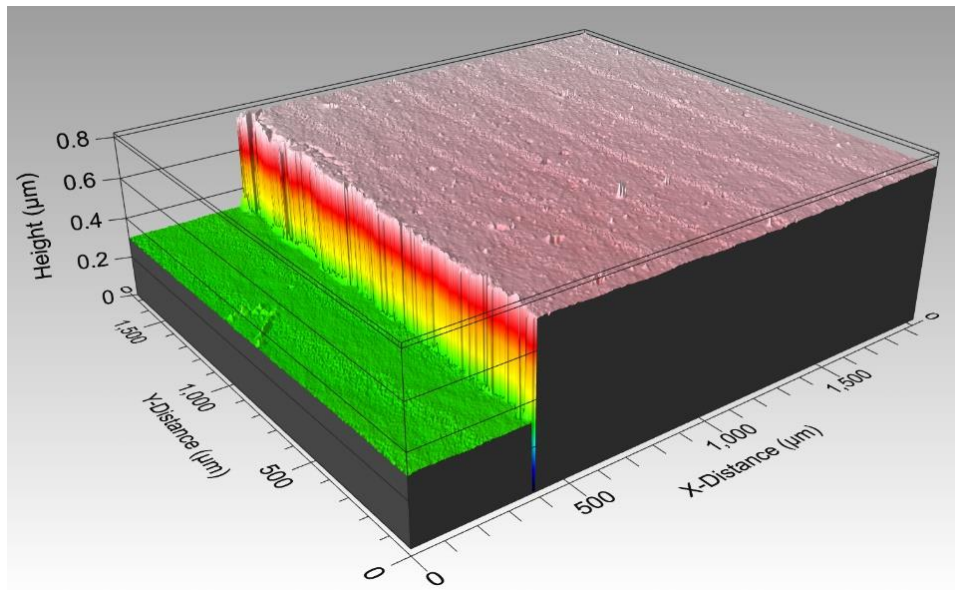
Figure 56 – 3D acquisition of a 2x2 mm² area of the sample Fe50_150a. The green surface is the silica substrate, the pink one the skutterudite thin film. Colour gradient only refers to the height of the sample.

From the data collection obtained by means of the optical profilometer (Figure 56 and Figure 57), it is possible to acquire some information. Thicknesses are found to be in the range between 226 and 463 nm, depending on the position on the substrate holder.
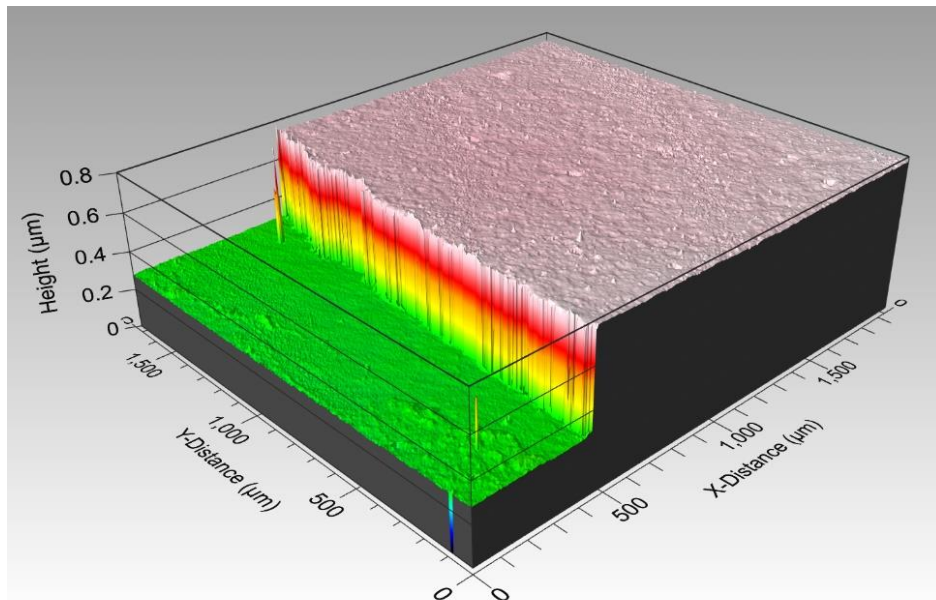
Figure 57 - 3D acquisition of a 2x2 mm² area of the sample Fe50_300a. The green surface is the silica substrate, the pink one the skutterudite thin film. Colour gradient only refers to the height of the sample.
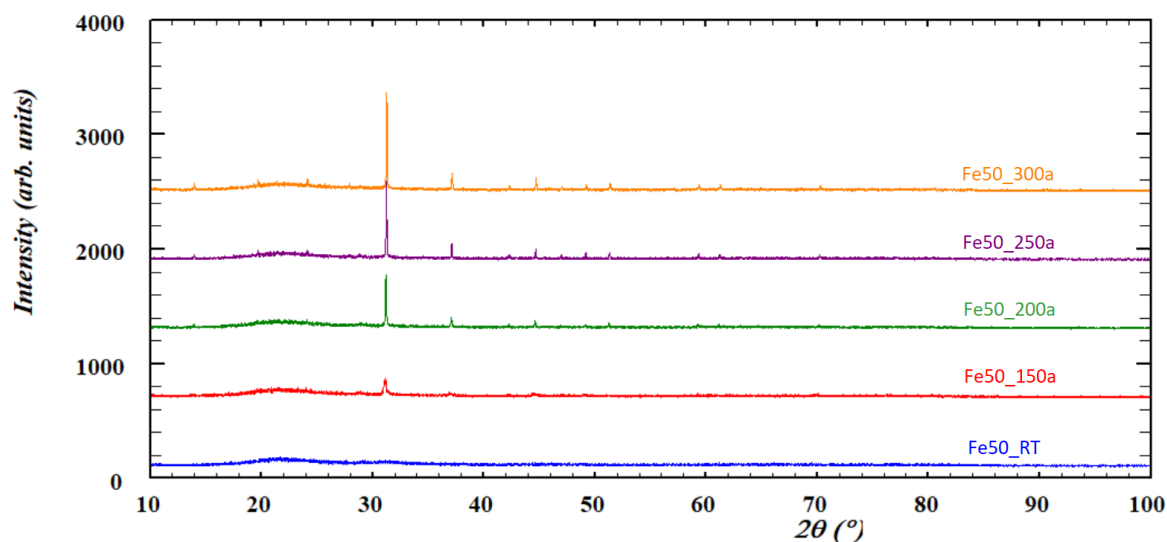
Figure 58 – Preliminary X-ray diffraction pattern of films belonging to the Fe50 series and annealed for 3 hours at different temperatures.

Samples annealed at 150 and 200 degrees are displaying a terraced surface morphology (Figure 56), already found in other films prepared by PLD, such as $YBa_2Cu_3O_{7-x}$ [186] and $SrTiO_3$ [187], while the surface appears flatter for samples annealed at higher temperatures (250 and 300 °C).

From the collected XRD diffraction patterns, performed before (FeXX_RT) and after the annealing process (FeXX_YYYa and FeXX_YYYb), it is noticeable the importance of the thermal treatment with the aim to obtain stable and crystalline samples. and same as the previous work, as-deposited samples clearly give origin to amorphous films, while, after the
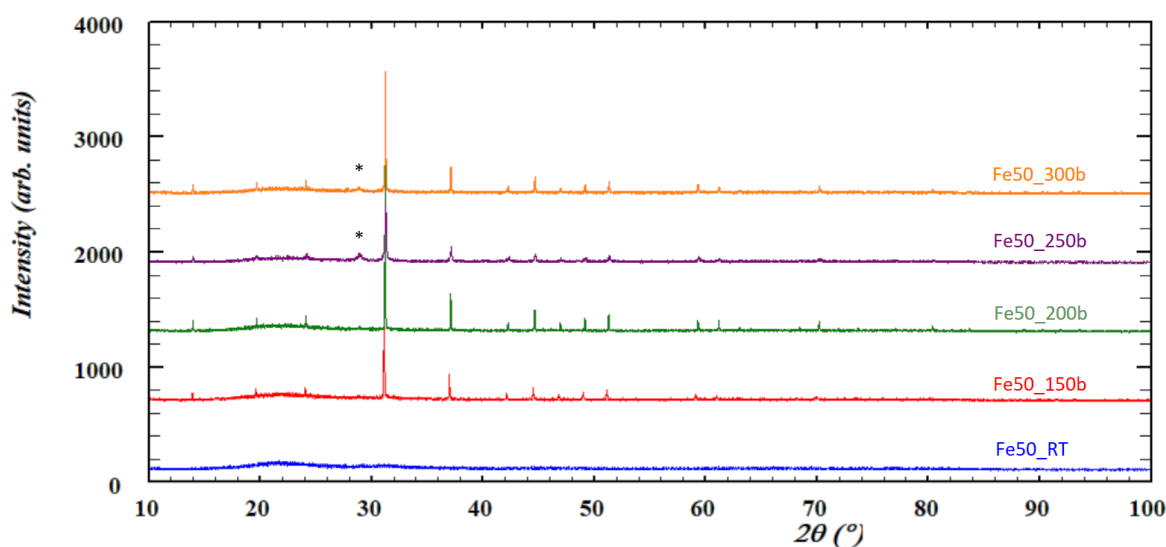
Figure 59 – Preliminary X-ray diffraction pattern of films belonging to the Fe50 series and annealed for 6 hours at different temperatures (refers to free Sb).*

annealing, skutterudite's diffraction peaks appear in the XRD diffractograms. No secondary phases are visible from this analysis for all samples annealed for 3 h and films annealed at 150 and 200 °C for 6 h, confirming the results described in Section 4.1.2.2. In the meanwhile, samples annealed at higher T show the appearance of a peak attributable to free Sb (Figure 59). In Figure 58 and Figure 59, it is only noticeable how the intensity of peaks increases with the annealing temperature and time. Anyway, as visible in Figure 58 and Figure 59, peaks are low and the signal/noise ratio is not enough good to obtain relevant info.

Although, the variation of the cell parameter a was preliminarily investigated by means of a graphic method with the software WinPlotR [188] in order to get a first overview of our samples and the results are reported in Table 5 and Table 6. As a general consideration, it can be seen that the cell parameter ($a = b = c$, being a cubic structure) decreases with the increase of the annealing temperature. This fact is quite common, due to the rearrangement caused by the thermal process. Because the lower parameter is accompanied by a change in the TE properties, as it will be described later, a slight change in the composition cannot be excluded (the cell parameter is sensitive to the quantity of Fe and Sm). Furthermore, by raising the quantity of Fe in the sample, especially between Fe63 and Fe70 series, the value of the cell parameter becomes bigger, as expected from a previous work of Artini et al. on bulk skutterudites belonging to the same system [42].

Table 5 - Cell parameters for the samples annealed for 3 hours (series a).

T annealing [°C]	Parameter Fe50_a [Å]	Parameter Fe63_a [Å]	Parameter Fe70_a [Å]
150	--	9.063	9.077
200	9.059	9.063	9.072
250	9.049	9.068	9.073
300	9.031	9.048	9.047

Table 6 - Cell parameters for the samples annealed for 6 hours (series b).

T annealing [°C]	Parameter Fe50_b [Å]	Parameter Fe63_b [Å]	Parameter Fe70_b [Å]
150	9.070	9.063	9.081
200	9.053	9.066	9.072
250	9.038	9.070	9.066
300	9.037	9.053	9.058

Samples belonging to the Fe50 series are less crystalline, and the higher the annealing temperature, the more pronounced the crystallinity is. The grade of crystallinity in the films

belonging to the series Fe63 is the highest among all samples. Deeper analyses regarding the cell parameter to understand its correlation with the thermal treatment are needed. Rietveld refinements to understand in depth the behaviour of the cell parameters, strain and domain evolution are required. Anyway, the signal/noise ratio was not high enough to perform the
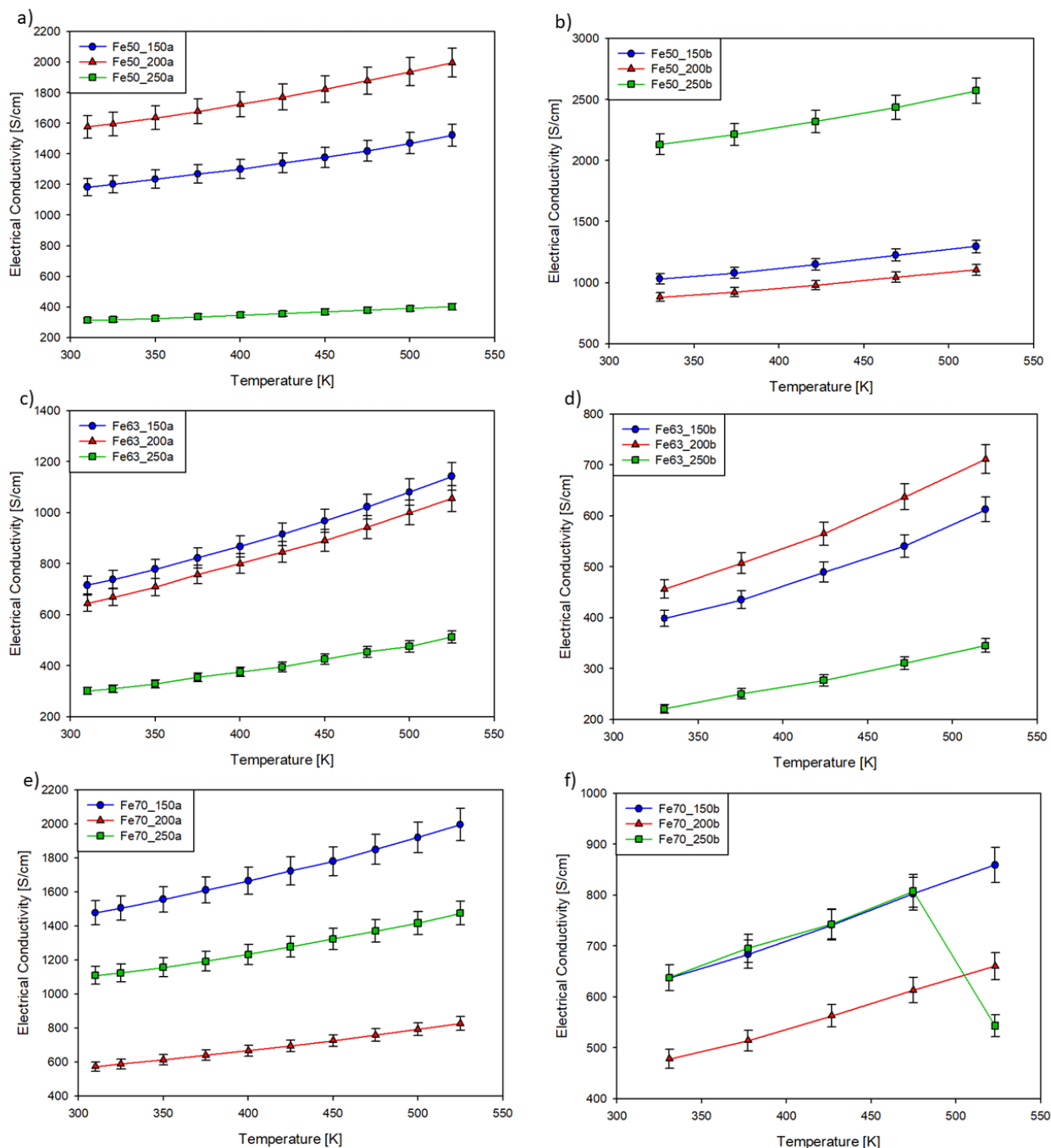
Figure 60 - Electrical conductivity vs. temperature. On the left side there are samples annealed for 3 hours while of the right-side sample annealed at 6 hours. Each graph focuses on one composition. Scales are intentionally displayed with different values to be able to appreciate better the differences between samples in the same plot. a) Fe50 for 3 h; b) Fe50 at 150°C for 6 h; c) Fe53 for 3 h; d) Fe63 for 6 h; e) Fe70 for 3 h; f) Fe70 for 6 h.

required advanced analysis. At this purpose, a new series called c was deposited and preliminary data are discussed later in this chapter.

Electrical conductivity, Seebeck coefficient and power factor were investigated with their dependence on temperature and on the annealing temperature. Most of the samples annealed at 300°C were not measured because they presented a clearly damaged brownish surface.

Contrarily to the behaviour of samples described in Section 4.1.2.2 in the Figure 51, 3- and 6-hours annealing processes are found long enough to obtain stable samples suitable for the thermoelectric properties' measurement at high temperature.

In Figure 60, the trend of electrical conductivity *vs.* temperature is presented for all samples. Values for films annealed for 3 hours, corresponding to all graphs on the left side, are found usually higher than the others. As the main observation, values for the sample annealed at 150°C are comparable to the values displayed in Section 4.1.2.2. Furthermore, the trends confirm the semiconducting nature of the samples.

In Figure 61 the electrical conductivity is displayed together with the respective cell parameters. Generally, it appears that both electrical conductivity and cell parameters decrease
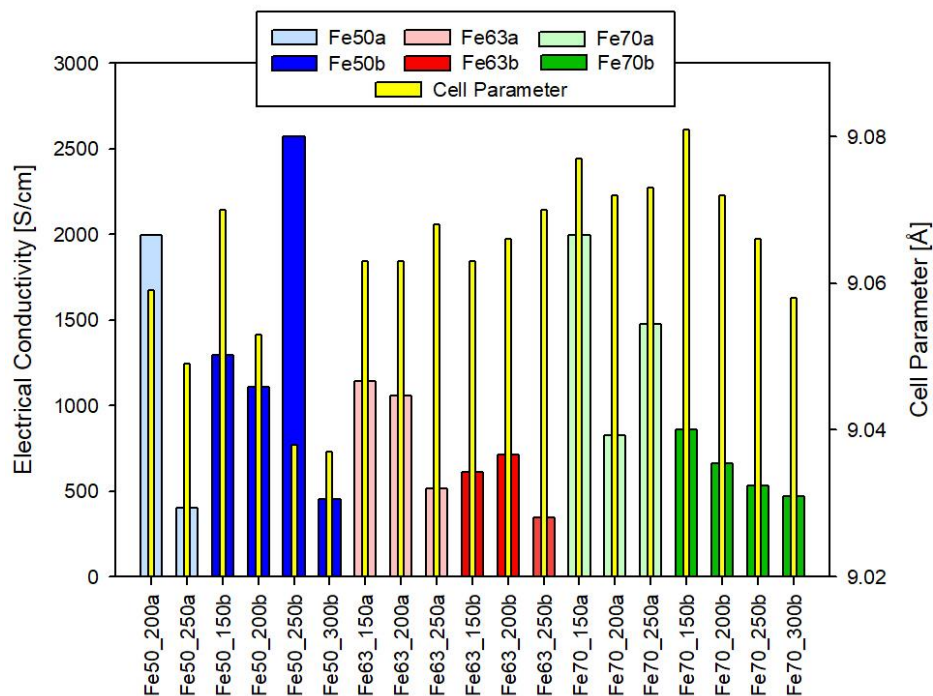
Figure 61 - Trend of the electrical conductivity at 573 K and cell parameters of the corresponding samples. Only samples for which both values were available are represented here.

with the increasing of the annealing temperature, with lower values for the longer annealing time.

Regarding Seebeck coefficient measurements, *S* vs. temperature is shown in Figure 62. The two compositions Fe63 and Fe70 present very similar data and result to be *p*-conducting,
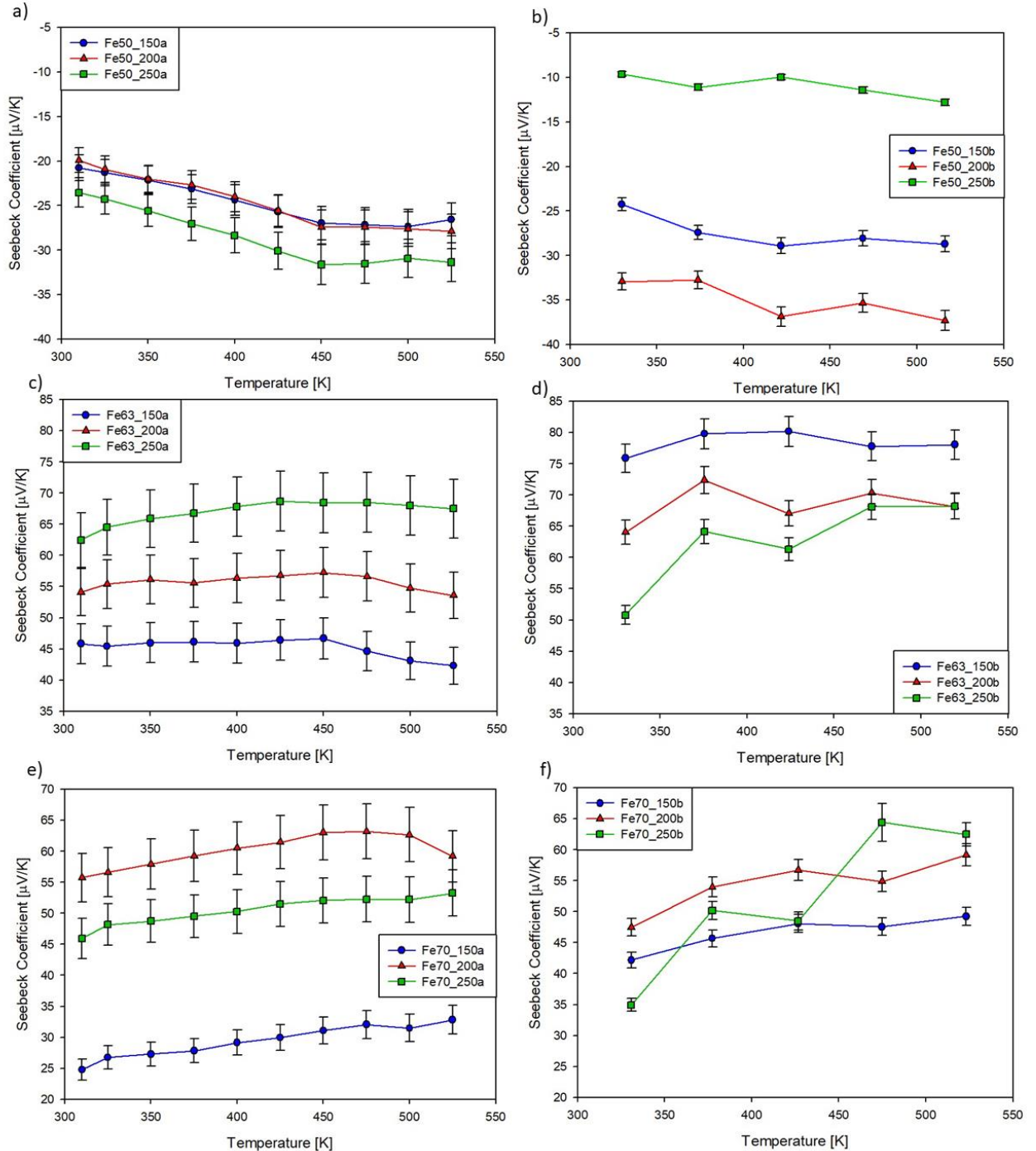
Figure 62 – Seebeck coefficient vs. temperature. On the left side there are samples annealed for 3 hours while of the right-side sample annealed at 6 h. Each graph focuses on one composition. a) Fe50 for 3 h; b) Fe50 at 150°C for 6 h; c) Fe53 for 3 h; d) Fe63 for 6 h; e) Fe70 for 3 h; f) Fe70 for 6 h.
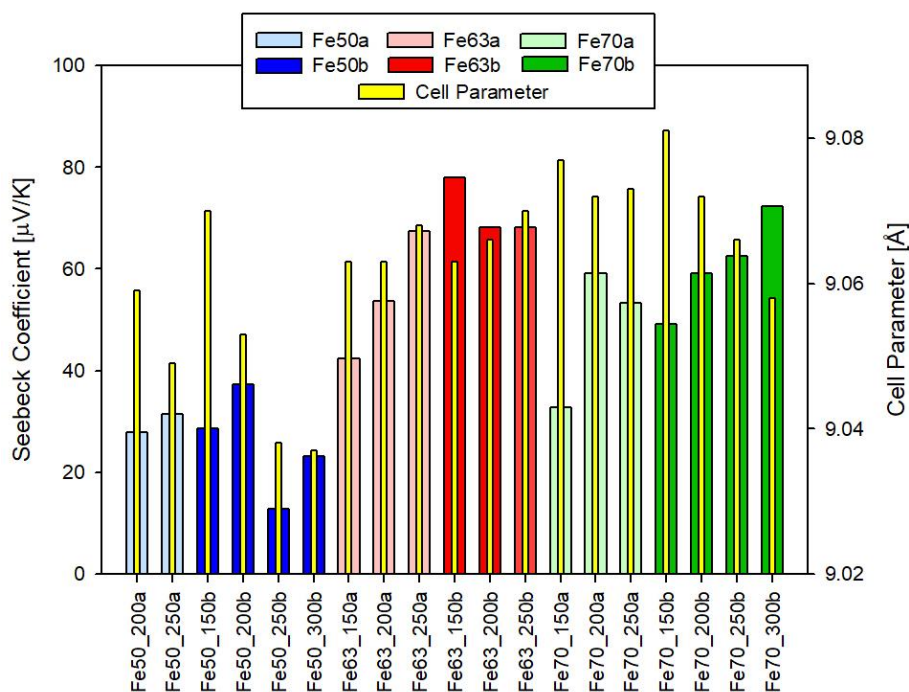
Figure 63 - Trend of the Seebeck coefficients at 573 K and cell parameters of the corresponding samples. Notice that absolute values are reported for the Fe50 series, for a practical reason. Only samples for which both values were available are represented here.

with values remarkably lower than the ones of (Sm,Gd)-filled compositions [41], same as described in Section 4.1.2.2, while the series Fe50 appears to be *n*-conducting, according to [143]. As a general consideration, all samples have a weak dependence on temperature, and maximum values are mostly found at 500 K. Peak values for each composition were found to be ~ -37 µV/K for the sample Fe50_200b, ~80 µV/K for the sample Fe63_150b and ~64 µV/K for the sample Fe70_250b.

Values of Seebeck at high temperature and cell parameters of the films are depicted in Figure 63. With the exception of the series Fe63a, Seebeck and cell parameters are showing an opposite trend as a function of the annealing temperature.

Considering the measured electrical conductivity and Seebeck coefficient, values of power factor in function as a temperature were then calculated and their trends are reported in Figure 64. Combining σ and *S*, the best performance is given by films annealed at 250°C for 3h. Aside from sample Fe63_150b, a longer annealing results in a degradation of the TE performances of the thin films. Regarding the absolute values of the observed maxima for each composition, they are 155 µW/m·K^2, 373 µW/m·K^2 and 418 µW/m·K^2 for samples Fe50_200a, Fe63_150b and Fe70_250a, respectively, which are significantly lower than the corresponding

data of the (Sm,Gd)-filled skutterudite [41], but comparable to ones obtained by Bourgès at all for $CoSb_3$ [51].

Same as before, data of best power factor for each composition are reported together with obtained cell parameters in Figure 65. No visible correlation arises from the plot.
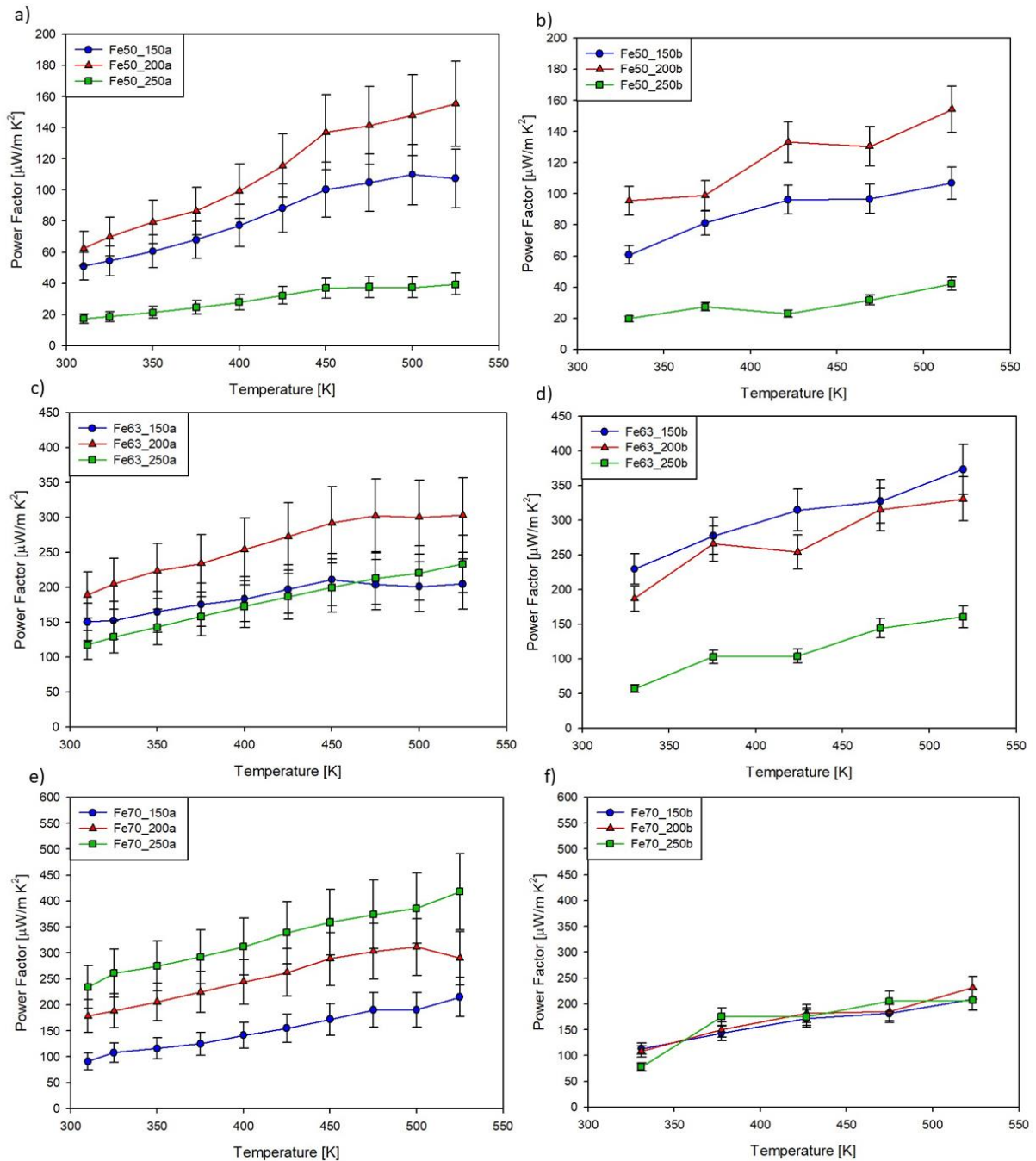
Figure 64 – Power factor vs. temperature. On the left side there are samples annealed for 3 hours while of the right side sample annealed at 6 h. Each graph focuses on one composition. a) Fe50 for 3 h; b) Fe50 at 150°C for 6 h; c) Fe53 for 3 h; d) Fe63 for 6 h; e) Fe70 for 3 h; f) Fe70 for 6 h.
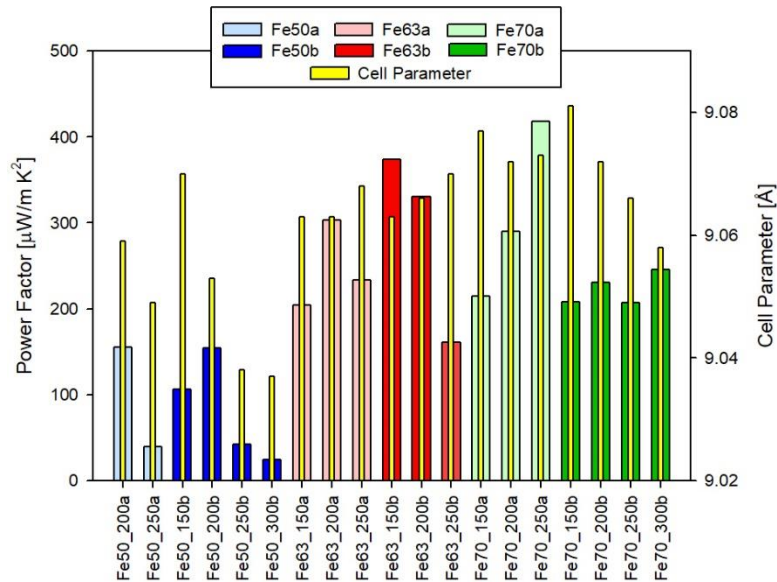
Figure 65 - Trend of the power factor at 573 K and cell parameters of the corresponding samples. Only samples for which both values were available are represented here.

In the tentative to explain the effect of the annealing on thermoelectric properties of the film in analysis, room temperature Hall measurements were performed to obtain the carriers' concentration n_H and mobility μ_H values for the as-deposited and annealed (FeXX_200a, 200°C for 3 hours) films and they reported in Figure 66a and Figure 66b respectively. The availability of the facilities was limited and the number of samples for the analysis has to be restricted. For this reason, the annealing temperature of 200°C was chosen due to the general higher TE performance of the samples compared to the other conditions, and as- deposited samples were measured as well in order to evaluate the effect of the heat treatment on the films. Anyway, values of resistivity and mobility of carriers are not available for the sample Fe70_200a due to a problem of peeling of the sample during the cleaning process prior to the measurement.

In both cases, moving from *n-* to *p*-type the mobility of carriers seems to decrease. Regarding the number of carriers, the trend is opposite in the two batches: for the as-deposited series, the number doubles from Fe50 to Fe70, while the exact opposite trend is shown for the annealed series. Resistivity values seem to have a maximum for the sample Fe63_RT, while it can be seen an increase between the sample Fe50_200a and Fe63_200a, but no info is available for the sample Fe70_200a, as explained before.

With the aim to make a comparison between the two series, the number of carriers, their mobility and the resistivity of samples are separately reported in Figure 67. In the Figure 67a, it is clearly visible how the annealing process caused a reduction of the number of carriers of an order of magnitude, from 10^{23} to 10^{22} cm^{-3}, while their mobility is doubled in the case of
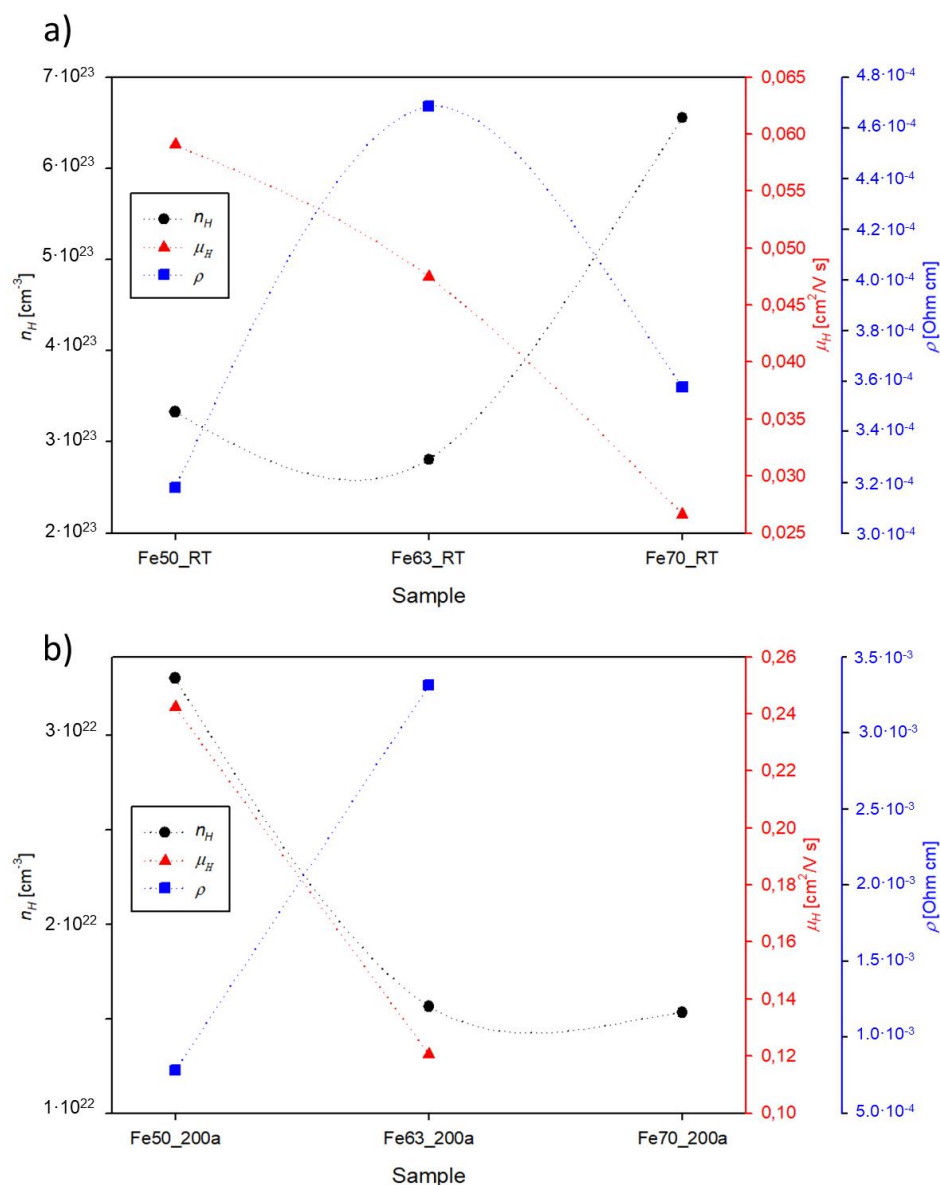
Figure 66 - Hall effect measurements of the number of carriers and their mobility for a) as deposited films and b) films annealed at 200°C for 3 hours in function of the starting target composition.

Fe63 and even increased by a factor of 4 for Fe50 (Figure 67b). Surprisingly, the resistivity increases after the annealing process.

As aforementioned, new X-ray acquisitions were performed on the new series c. Conditions of the analysis were changed, acquiring overnight measurements with a much lower scan speed, aiming to obtain a better signal/noise ratio suitable for deeper refinements. Unfortunately, due to time constraints on the common equipment, no data regarding the sample Fe50_150c are available. For the same reason, the variation of the cell parameter *a* was only preliminary investigated by means of a graphic method with the software WinPlotR [188] and
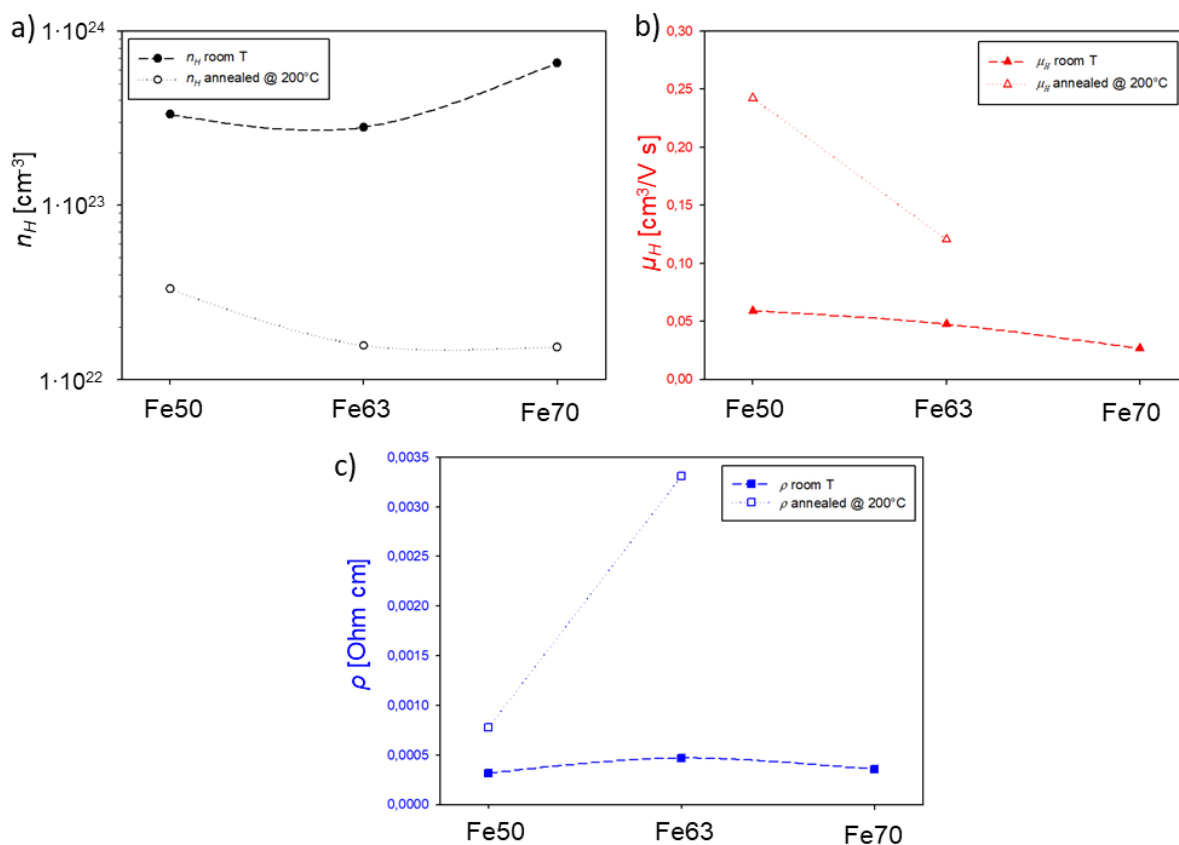
Figure 67 – a) Number of carriers, b) mobility of carriers and c) resistivity for both as-deposited and samples annealed at 200°C for 3h.

deeper analysis will be carried out soon in the view of the preparation of a paper. Results are listed in Table 7 and graphically shown in Figure 68.

At a first glance, it is clear that these values are higher than the previous ones and are closer to what was described by C. Artini et al [42] for bulk skutterudites with the same compositions (Figure 69). As a general trend, rising the temperature of annealing, the cell parameter increases as well for all compositions. This may be due to the rearrangement and reorder of the structure thanks to the heat treatment. Moreover, same as the trend shown in Figure 69 for bulks, our films present enlargement of the cell parameter between the composition Fe50 (x = 0.5) and Fe70 (x = 0.7). Anyway, it is hard to explain why the cell size appears bigger for the crossover composition Fe63 (x = 0.63), even though it should be comparable to Fe50 and smaller than Fe70. Unfortunately, deeper analyses are needed again in order to understand the real and precise effect of the annealing on our samples. Besides, the new XRD data, as aforementioned, have much better quality and we positively think we will be able to obtain more info in the near future.

Table 7 - Cell parameters for the samples annealed for 3 hours (series c).

T annealing [°C]	Parameter Fe50_b [Å]	Parameter Fe63_b [Å]	Parameter Fe70_b [Å]
150	-	9.144	9.129
200	9.104	9.137	9.125
250	9.103	9.137	9.120
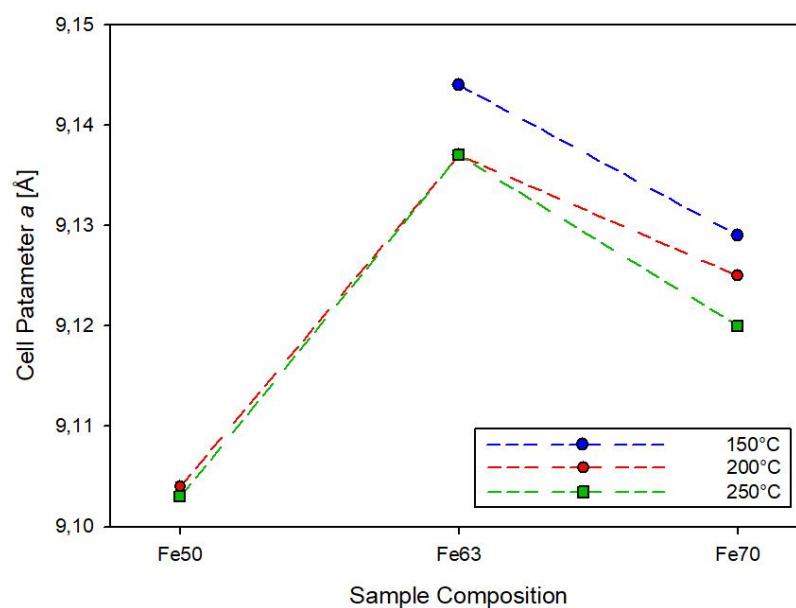
Figure 68 - Cell parameter for samples belonging to the series c.
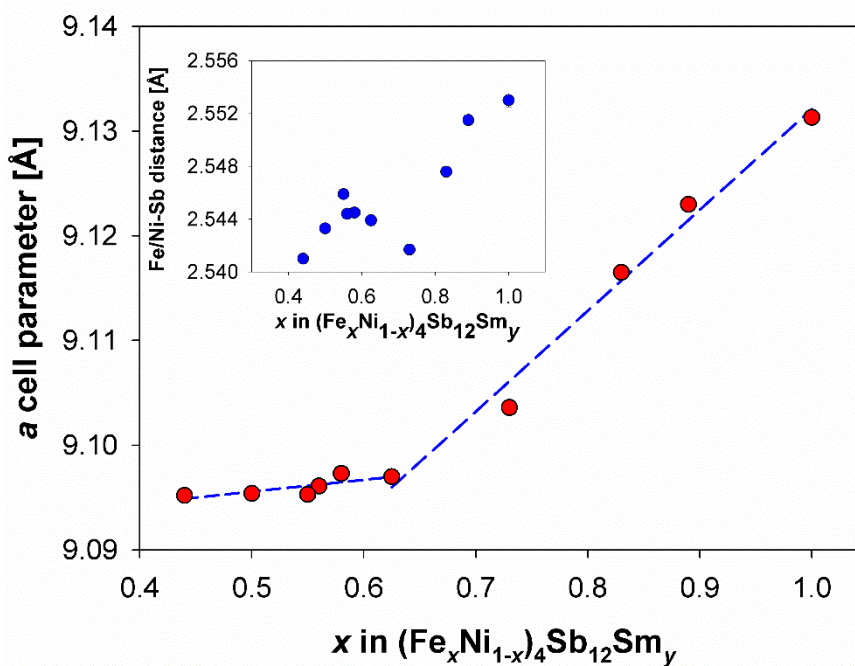
Figure 69 - Trend of the cell parameter of bulk $Sm_y(Fe_xNi_{1-x})_4Sb_{12}$ filled skutterudites as a function of x [42].

4.2.3   Conclusions

With the aim to obtain stable filled skutterudites thin films belonging to the $Sm_y(Fe_xNi_{1-x})_4Sb_{12}$ system, a systematic study of the effect of the annealing was performed. Thin films were prepared via the PLD method using fused silica as substrate. Intending to perform a complete work, targets of both *n-* and *p-*type, such as the composition lying on the crossover between them, were used. The difference between 3 and 6 h of annealing was investigated, such as the dependence of TE properties on the annealing of the thermal treatment. All the starting thin films were deposited at room temperature, to be successively subjected to an annealing treatment at 150, 200, 250 and 300°C. The last temperature was not found suitable for the material, causing an evident degradation of the film, immediately intuitable from the brownish surface of samples.

At a preliminary point of the analysis, we noticed that, as a general rule, annealing performed at 200°C and for 3 h is the best combination for these Fe,Ni-based filled skutterudites. Measurements of carriers' concentration and mobility were carried on only on as-deposited and samples annealed at 200°C for time and apparatuses limitations, and they will need to be performed on the remaining films to clarify the correlation of the transport and thermoelectric properties with the annealing temperature. Moreover, better XRD patterns were acquired, but more time is needed to complete good refinements. From a preliminary cell parameter calculation, values decrease with the rising of the annealing temperature, probably because of an effect of rearrangement of the structure and values are similar to the bulk ones. Anyway, Fe63 shows a bigger size of the cell than expected but no more information is available at the moment.

4.3 Preliminary Thermoelectric Performances' Test of a Skutterudite Thin Film Device

On-chip thermoelectric thin film module containing five *n*-type and five *p*-type skutterudite legs, from the targets Fe50 and Fe63 respectively mentioned in Section 4.2, was fabricated on a fused silica substrate by the pulsed laser deposition technique. The performance of modules was measured using ad custom-made system at Shibaura Institute of Technology displayed in Figure 70, following the procedure previously done by S. Saini et al [189].
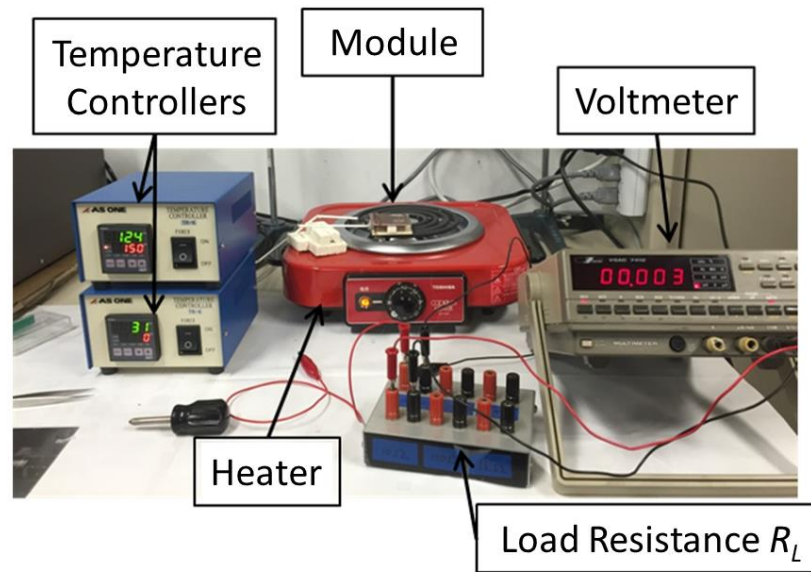
Figure 70 - Custom-made apparatus available at Shibaura IT in Professor Mele's laboratory.

As described by J. García-Cañadas [190], we consider a thermoelectric device made by *2N* legs, with *N* the number of *n*- and *p*-type semiconductor pairs, under steady-state conditions. The material's properties are considered independent of temperature and have an average value for the operating temperature range and they are considered equal for both *n*- and *p*-type materials. In this case, the system delivers a certain amount of electric power *P* when connected to a load. The power delivered to the load (called R_L) is given by the equation:

$$P \ = \ I \ \Delta V_L \tag{18}$$

where *I* is the electric current and ΔV_L the potential difference across the load, expressed as:

$$\Delta V_L \ = \ I \ R_L \tag{19}$$

It can be seen from Equation 19 that ΔV_L and I, and therefore P, vary when changing the load resistance, which is a parameter that can be conveniently adjusted. After various mathematical steps, it is found that the maximum power P_{max} is achieved when:

$$P_{max} = \frac{[2N \, |S|(T_h - T_c)]^2}{4R_L} \tag{20}$$

where T_h and T_c are hot-end and cold-end temperature of the module and $|S|$ is the absolute average Seebeck coefficient, instead of using the single S values for the n- and p-type materials for clarity. This equation predicts a parabolic relationship between P_{max} and ΔT, which experimentally is frequently found. Using Equation 2, Equation 20 can be also written as:

$$P_{max} = \frac{[2N \, V_L]^2}{4R_L} \tag{21}$$

As a consequence, V_L was acquired with varying R_L values, and P_{max} was plotted as a function of the voltage. The maximum output power at each temperature was then graphically determined as the peak of the polynomial bell-shape fitting the experimental points.

4.3.1   Materials and Methods

Thin film devices were prepared by pulsed laser deposition using a Nd:YAG (266 nm, 10 Hz) laser. The substrate of silica in a squared shape (1x1 cm^2) underwent initially a cleaning process at 773 K for 2 h in air, and, thenceforward, they were secured to an Inconel plate with silver paint. Before being inserted into the PLD chamber, the substrate was covered with a custom-made Nickel mask (Process Lab. Micron Co. Ltd, Nagoya) (Figure 71) in order to selectively deposit only the desired legs on the silica substrate. The laser was shot on the dense targets (p-type Fe63 first) with an energy density of about 4.2 J/cm^2 for a deposition time of 30 minutes under a high vacuum (10^{-4} Pa) and at room temperature. Then, the Ni mask was manually shifted in order to deposit the second set of legs (n-type Fe50) under the same aforementioned conditions. The final result of all 10 legs deposited on the 1x1 cm^2 transparent substrate is shown in Figure 71. The device underwent then to an annealing process at 200°C

for 3 hours in order to enhance the thermoelectric properties of the materials as reported in Section 4.2
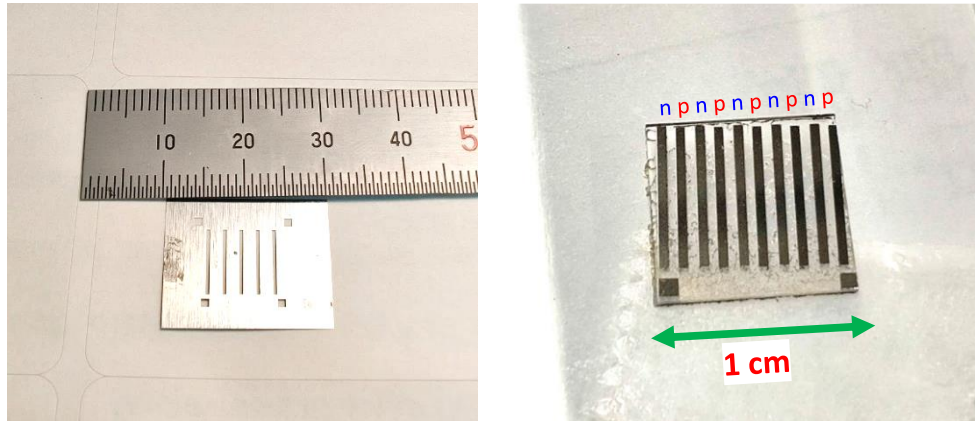
Figure 71 - On the left side, the Ni mask used for the selective deposition of thermoelectric legs of the device. On the right side, a completed deposition of both n- and p-type legs.

Gold electrodes are then deposited in order to connect in series the device's legs by means of a Gold Sputtering (Sanyu Electron, SC-701Mk II). A different custom-made Ni mask (Process Lab. Micron Co. Ltd, Nagoya) (top left of Figure 72) is perfectly aligned on the sample, which then is inserted in the sputtering apparatus for the deposition of the Au. On the top right part of the Figure 72 the mask and the piece of glass (used only as support) are portrayed after the process was completed.
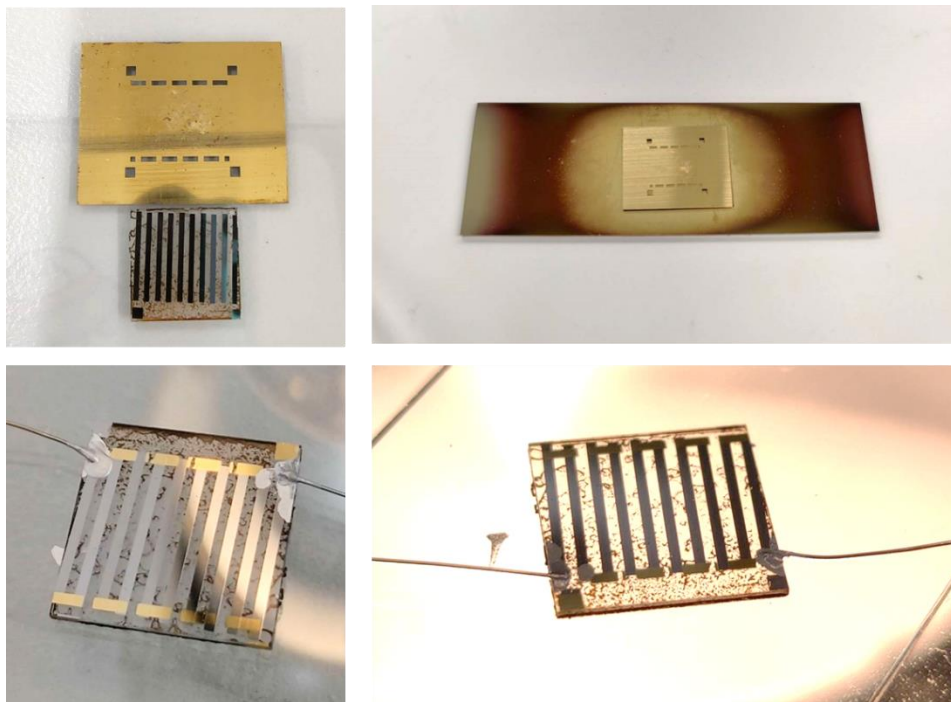
Figure 72 - Upper pictures: gold deposition of the electrodes. Bottom pictures: wires connections.
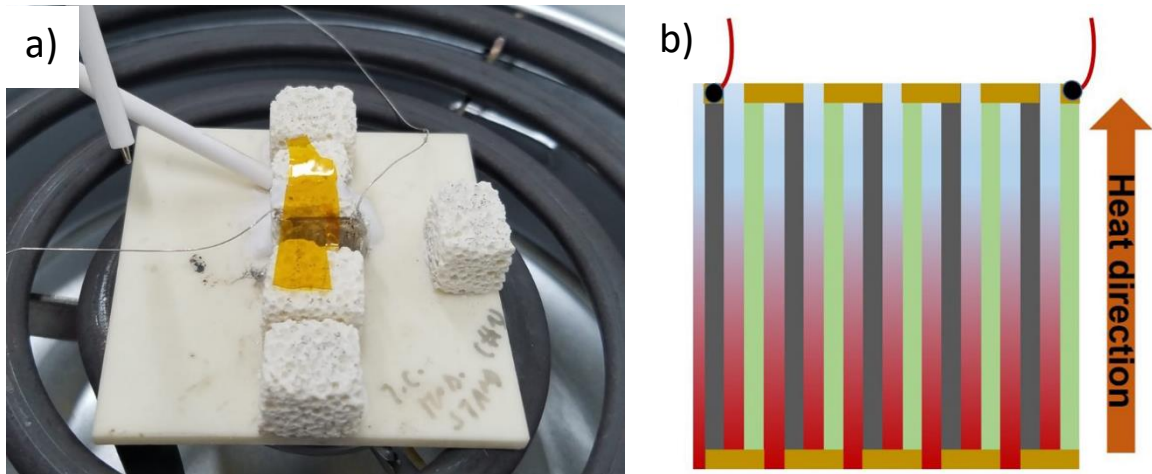
Figure 73 – a) Vertically-placed skutterudite module on the alumina plate. Ni wires are visible. b) Direction of the heat flow during the performance measure on a thermoelectric thin film module [189].

In order to perform the measurement, it was necessary to attach Ni wires to the sample by means of silver epoxy. The result is shown in the bottom part of Figure 72.

Measurement of the performance of modules was carried out using an *ad hoc* customized system where the module was arranged vertically (Figure 73a) in between alumina positioned on a hot plate, which works as the heat source, and aluminium nitride sheet, working as a heat sink, in contact with a beaker full of ice. The sample is positioned vertically with legs perpendicular to the heat flow (Figure 73b) in order to maximize the thermoelectric output of the device, being the module fabricated in a lateral Π-shape. The experimental setup is schematically portrayed in Figure 74.
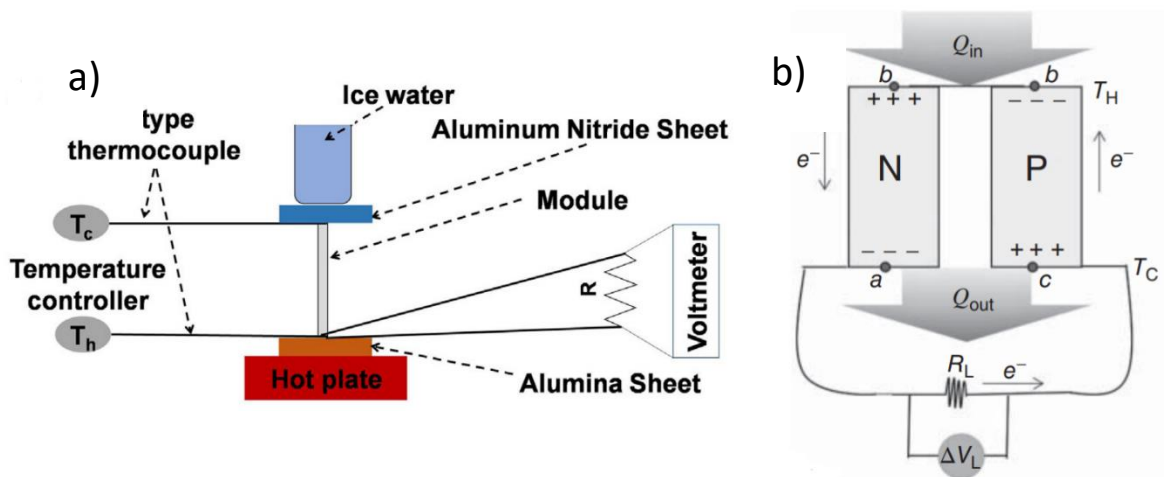
Figure 74 – a) Schematic of module testing set-up with a load resistor ($R = R_L$), where T_h and T_c are hot-end and cold-end temperature of the module, respectively. The module is portrayed in his cross section [189]. b) Scheme of an n- and p-type semiconductor couple under power generation mode delivering electric power to a load (R_L) [190].

The generation of thermoelectric voltage was checked by manually heating up the module from the bottom on a hot plate (T_h up to 300°C) while monitoring voltage (by Keithley 2182A) and temperature through two K-type thermocouples controlled by TR-KN units (AS-ONE) placed on Al_2O_3 and AlN sheets. A difference in temperature between the two sides of the module was generated by setting a water beaker as a coolant on the top of AlN sheet. This thermoelectric voltage is acquired by using a variable resistance (in the range of 10 Ω to 10^6 Ω), called load resistance R_L, and power was estimated at different temperatures (100, 200 and 300°C) for each value of external resistance.

4.3.2 Results and Discussion

The measure of V_L was repeated four times for each chosen R_L and the average value of the potential has been used then to plot the *P vs. V_{Lavg}* graph by means of Equation 21. Values are reported in Table 8 for three distinct temperatures of the hot side. Afterwards, polynomial trendlines were added.

The maximum output power at each temperature was determined as the peak of the polynomial bell-shape fitting the experimental points (plotted in Figure 75). For the temperature on the hot side equal to $T_h^1 = 100$°C, the maximum of the curve graphically relies around the value of $P_{max} \approx 3.2 \cdot 10^{-8}$ W, while in both cases of $T_h^2 = 200$°C and $T_h^3 = 300$°C we found a $P_{max} \approx 1.6 \cdot 10^{-7}$ W.

Table 8 – Hot side temperature, load resistance, average potentials and calculated power for the skutterudite device.

Th [°C]	*ΔT* [°C]	R_L [Ω]	V_{Lavg} [mV]	*P* [W]
		1000	0.5283	$6.976 \cdot 10^{-9}$
100	45	10000	3.466	$3.003 \cdot 10^{-8}$
		100000	7.380	$1.362 \cdot 10^{-8}$
		1000000	8.152	$1.661 \cdot 10^{-9}$
		1000	1.250	$3.906 \cdot 10^{-8}$
200	95	10000	7.972	$1.589 \cdot 10^{-7}$
		100000	13.70	$4.671 \cdot 10^{-8}$
		1000000	13.16	$4.327 \cdot 10^{-9}$
		1000	1.685	$7.098 \cdot 10^{-8}$
300	110	10000	7.798	$1.520 \cdot 10^{-7}$
		100000	14.49	$5.246 \cdot 10^{-8}$
		1000000	15.35	$5.893 \cdot 10^{-9}$

These values are 3 to 4 orders of magnitude better than what reported by S. Saini et al [189] for oxides TE modules, which were in the order of $P_{max} = 3 \cdot 10^{-11}$ W at 300°C.
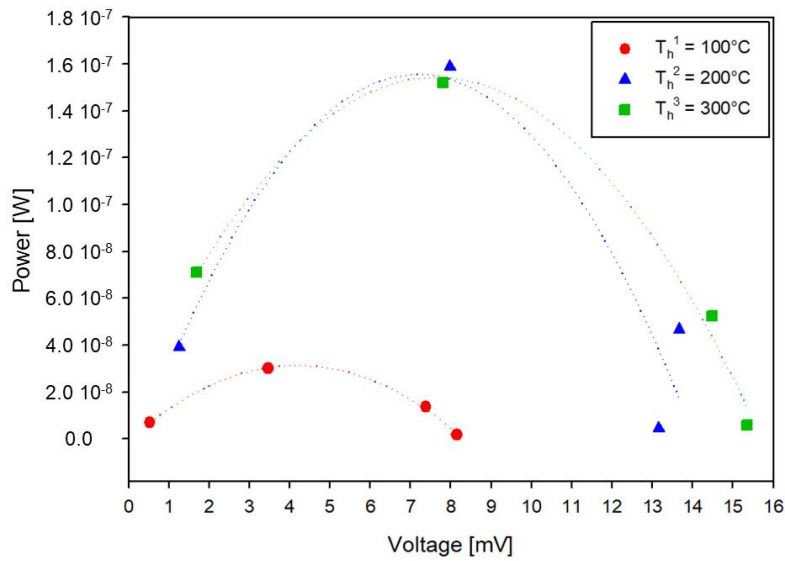
Figure 75 - Plots of the fitting polynomial curves for the three temperatures of 100, 200 and 300°C.

4.3.3 Conclusions

The preliminary on-chip thin film thermoelectric module fabricated by PLD and entirely made by Fe,Ni based filled skutterudites has been successfully fabricated. The performance of the on-chip thermoelectric module was evaluated by an *ad hoc* customized system where the module was set vertically. The output power increased between the operating temperatures of 100 and 200°C, while no substantial difference was found between 200 and 300°C, settling a maximum of $P_{max} \approx 1.6 \cdot 10^{-7}$ W, which is 3 to 4 orders of magnitude better than what was reported by S. Saini et al [189] for oxides TE modules. Further studies will be carried out varying the composition of the targets and substrates in order to find the best possible performance.

5 ALUMINUM-DOPED ZINC OXIDE THIN FILMS

5.1 Synthesis and Characterization of Al- and SnO$_2$-Doped ZnO Thermoelectric Thin Films

The attention of researchers towards the thermoelectricity field has been recently focused on the development of stable, environmentally benign, abundant, and cost-effective TE materials based on oxides. The *ZT* of oxides is not yet up to the level of the best conventional TE materials and requires to be drastically improved to reach a level acceptable for practical applications. The bulk oxides also have the main disadvantages of the requirement of a long time for sintering and fabrication of the *n-* and *p-* elements, and their assembling in module shape, and mechanical fragility. All these drawbacks can be overcome by using oxide thin films. Thin-film materials offer significant advantages to developing oxide TE with high performance: low dimensionality, rapid fabrication, control of strain at the interface with substrates, and the possibility to insert artificial nano-defects to improve the phonon scattering.

In this work, we have been focused on enhancing the thermoelectric performance of Al-doped ZnO films by the addition of a controlled amount of SnO$_2$ as a secondary dopant. AZO has the same structure of hexagonal ZnO: wurtzite, hexagonal, space group ***P6$_3$mc,*** cell parameters $a = b = 0.3289$ nm and $c = 0.5307$ nm, while SnO$_2$ is cassiterite, tetragonal, space group ***P4$_2$/mnm*** and cell parameters $a = b = 0.4832$ nm and $c = 0.3243$ nm. Since the mismatch between the *a*-axis of AZO and the *c*-axis of SnO$_2$ is 1.4%, we forecasted the growth of quasi-epitaxial nanostructures (nanoparticles) of SnO$_2$ with $c_{SnO2}//a_{AZO}$, dispersed in the AZO matrix.

The motivation of this study is to prove the presence of SnO$_2$ nanoparticulate into the AZO matrix and verify the optimal content of SnO$_2$ for the TE properties of the nanocomposite Al- and SnO$_2$- doped (AZO+SnO$_2$) thin films.

5.1.1 Materials and Methods

5.1.1.1 *Deposition of thin films*

Two sets of four thin films were prepared using various compositions and substrate materials. All samples were deposited both on amorphous silica and *c*-axis oriented alumina by pulsed laser deposition (PLD) technique focusing a Nd:YAG (266 nm, 10 Hz) laser on dense pellets. Four commercial targets (Kurt Lesker Ltd, Jefferson Hills, PA, USA) used for film making had different content of SnO_2 (0, 1, 2 and 4 %w) dispersed in the Al-ZnO (AZO) main phase where the Al content is kept as 2 w%. Prior to the deposition, the substrates were cleaned at 773 K for 2h, then glued by conductive silver glue to a rectangular Inconel plate, which was put in direct thermal contact with a cartridge heater and finally inserted into the vacuum chamber. All films were grown with an energy density of about 4.2 J/cm^2 for 60 minutes at 573 K, in the atmosphere of 20 mtorr of oxygen. Thereafter, the samples deposited on silica will be named AZO_xS and the ones deposited on alumina AZO_xA, with x = 0, 1, 2 and 4 referring to the concentration (w%) of the SnO_2 in the respective targets.

5.1.1.2 *Characterization of thin films*

Electrical conductivity (σ) and Seebeck coefficient (S) were measured by means of the four-probe method using a ZEM-3 (ULVAC Advance-Riko, Yokohama, Kanagawa, Japan) apparatus under partial He pressure to assure thermal transport between the heater and the sample. Measurements with ZEM-3 were conducted performing three cycles between 353 and 573 K and measuring both heating and cooling processes. The σ and S curves reported in the Results section for each sample are the ones obtained from the last cooling cycle, considered as the most stable and reliable one. The uncertainties on the ZEM-3 measurements are considered equal to ±4% on the electrical conductivity and ±3% on the Seebeck coefficient ones.

The thickness of the thin films (in the range 295-585 nm, as summarized in Table 9) was obtained by using a Dektak 6M Stylus Profiler (Bruker, Billerica, MA, USA) measurement system and a Filmetrics Profilm 3D (KLA, Milpitas, CA, USA).

The X-ray diffraction analysis was conducted on a Bragg-Brentano powder diffractometer (Smart Lab 3, Rigaku Corporation, Tokyo, Japan) using the Cu Kα radiation in the 10° - 100° angular range with angular step 0.02° (power settings: 40 mA, 40 kV).

The TEM images and EDS analyses were conducted on JEM-2100F (JEOL, Akishima, Tokyo, Japan) with EDS spectroscopy. The STEM beam size was set to 0.5 nm.

The picosecond Time-Domain Thermo Reflectance (TD-TR) technique using a customized focused thermal analysis system based on PicoTR (PicoTherm, Netzsch Japan KK, Tsukuba, Japan) was utilized to measure the thermal conductivity of the samples at room temperature ($T = 300$ K) in the cross-plane direction.

Hall coefficient determination at room temperature was performed through the usage of a standard 4-terminal method with a commercial PPMS instrument (Quantum Design, San Diego, CA, USA) using an electrical AC current of 5 mA.

5.1.2   Results and Discussion
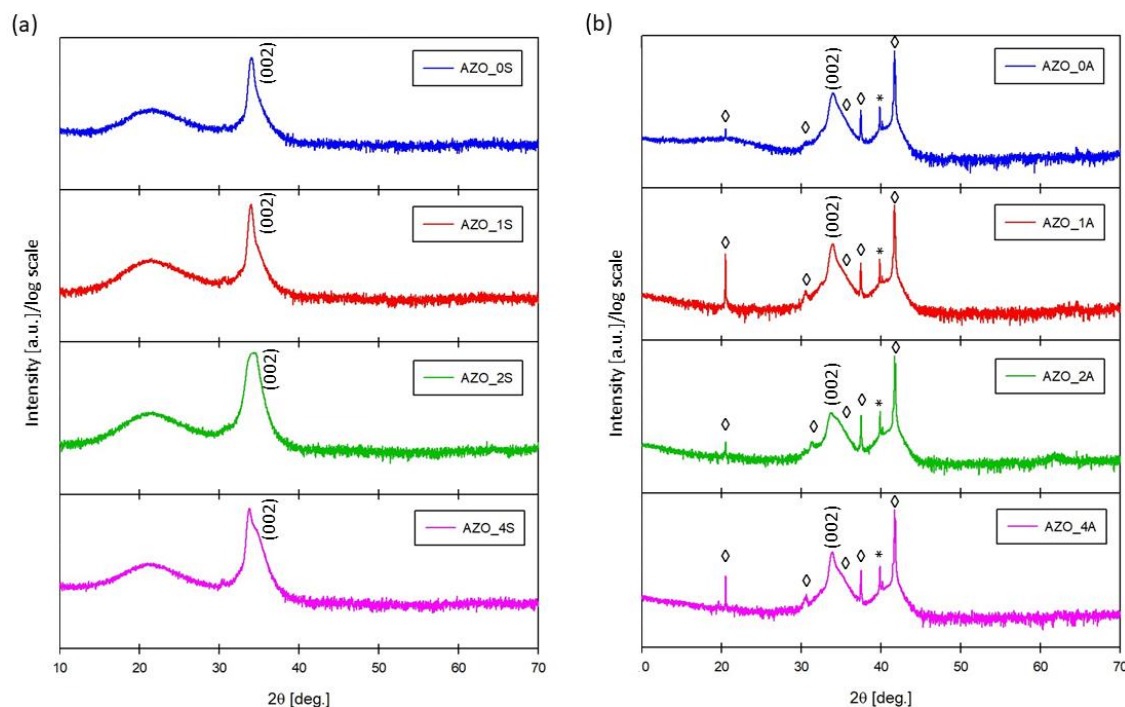
*Figure 76 - XRD spectra of AZO films deposited (a) on silica (series AZO_xS); (b) on Al₂O₃ (series AZO_xA). (hkl) reflections of AZO are indicated, while ◊ labels the peaks of Al₂O₃ substrate and asterisks * the unattributed peaks [175].*

The θ-2θ XRD patterns of the thin films fabricated on amorphous silica and single-crystal c-axis oriented Al_2O_3 are reported in Figure 76 (a) and (b), respectively.

On both substrates, the preferred orientation of AZO films is along the c-axis since only (00l) reflection appears. The presence of SnO_2 in the films of both series is undetectable by X-rays even for the highest amount (x = 4).
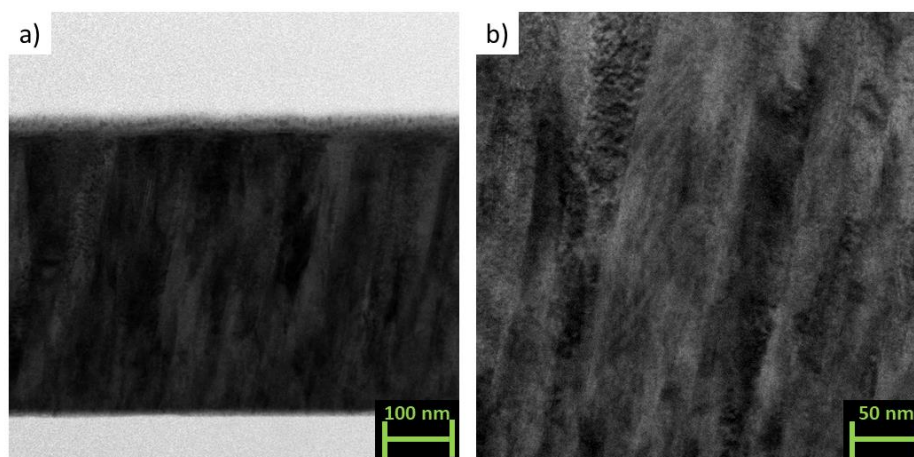
Figure 77 - (a) cross-sectional TEM image (magnification 150000X) of the AZO/silica thin film AZO_0S; (b) double magnification (300000X) taken on the central zone of figure (a) [175].
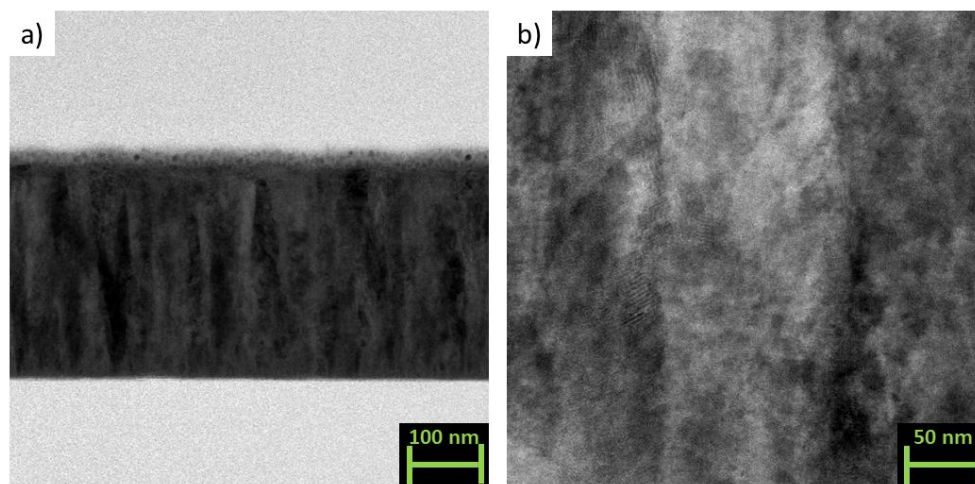
Figure 78 - (a) cross-sectional TEM image (magnification 150000X) of the AZO/silica thin film AZO_2S; (b) double magnification (300000X) taken on the central zone of figure (a) [175].

The cross-sectional TEM images (magnification 150000X, Figure 77a and Figure 78a) of two representative samples deposited on fused silica without (AZO_0S) and with the addition of SnO_2 (2 w%, AZO_2S) reveal a typical columnar growth along the c-axis of the films as often reported in the literature for AZO PLD thin films [54,56,126,128]. The addition of SnO_2 (AZO_2S) is not affecting the morphology of the films. The higher magnification images (300000X, Figure 77b and Figure 78b for AZO_0S and AZO_2S, respectively) show that the
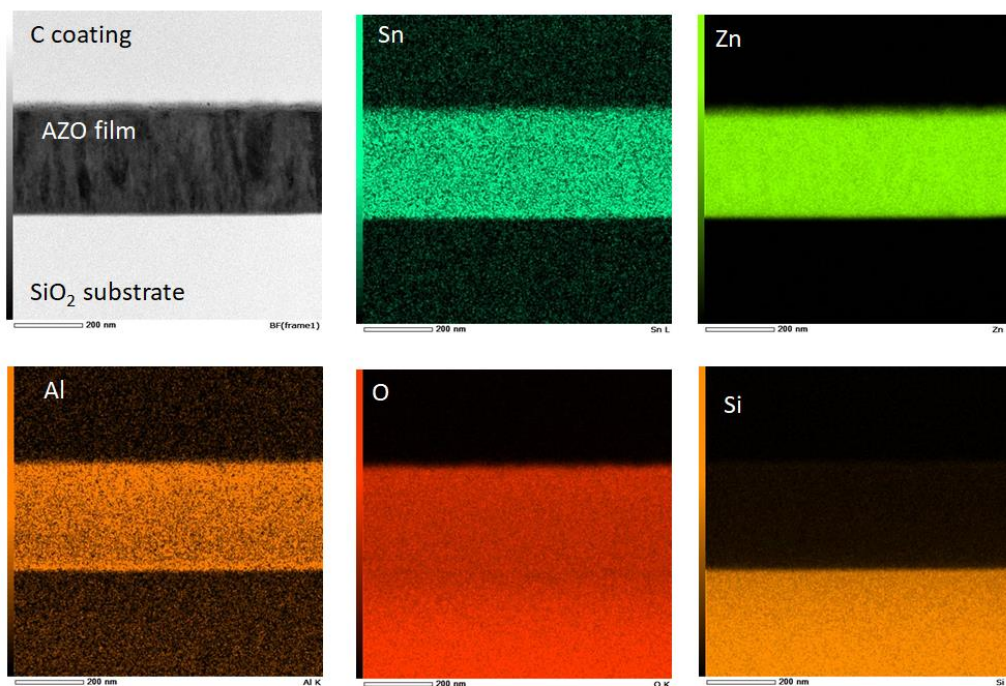
Figure 79 - TEM-EDS elemental maps of the AZO+SnO₂ 2 w% silica thin film (AZO_2S) for the atoms Sn, Zn, Al, O and Si [175].

columns are well connected without the presence of pores or misoriented grains so that the density of the films can be considered close to the theoretical value.

The TEM-EDS mapping performed on sample AZO_2S (Figure 79) reveals a uniform distribution not only of the elements Al, Zn, O, but also of Sn. Contrary to the predictions based on the 1.4% lattice mismatch, Sn did not form nanoscale aggregates into the AZO matrix but
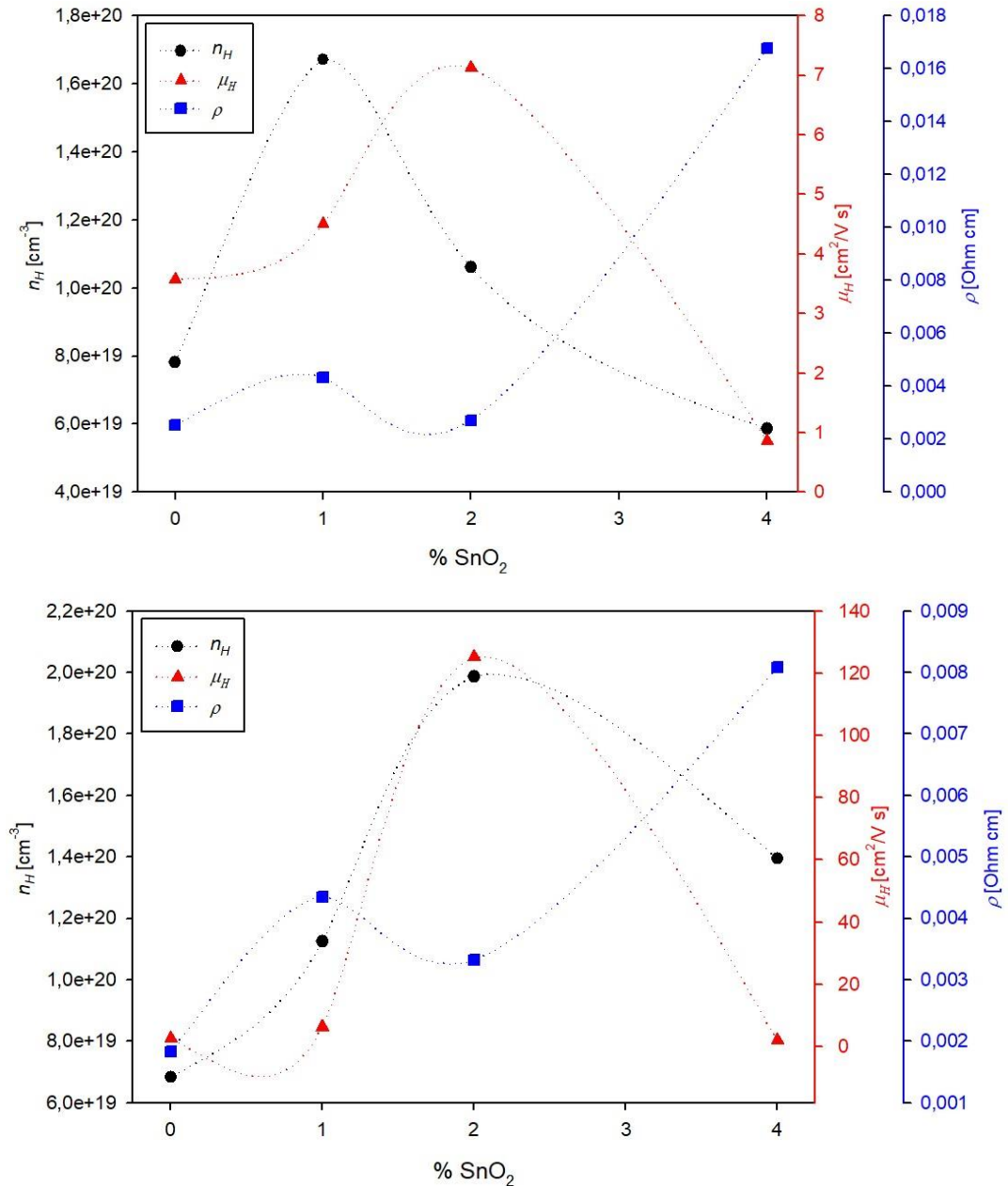
Figure 80 - Hall effect measurements of the number of carriers and their mobility for films deposited (a) on silica (series AZO_xS) and Al$_2$O$_3$ (series AZO_xA) in function of the % content of SnO$_2$ (x). Please note that is reported the absolute value of n$_H$ with the aim of simplifying the reading. The resistivity of both series was measured at the lowest temperature (348 K) using the ZEM-3 apparatus. Modified from [175].

presumably entered as substitutional or interstitial atom in the AZO elementary cell. According with TEM-EDS analysis, the atomic % of Sn in the film prepared with 2 w% SnO_2-added AZO target is 0.49%. The atom % of oxygen is 33.91%. Since it is not possible to separate the contribution of oxygen from SnO_2 and from ZnO, we can only compare the % of Sn in the target and in the film. The % of Sn in SnO_2 is 78.77%, which in 2 w% SnO_2 corresponds to 1.58%. This means that in the film the amount of Sn is about 1/3 than in the target. Si is not considered in the discussion being part of the substrate only.

Room temperature Hall measurement was performed to measure the carriers' concentration n_H and mobility μ_H values for the AZO_xS and AZO_xA films and it is reported in Figure 80, together with room temperature resistivity values from the ZEM-3 analysis.

The resistivity at room temperature has a clear ascending trend with the content of SnO_2 on both substrates and the films on Al_2O_3 present values of about a half of those of the films grown on silica. The range of n_H is almost the same on the two substrates, and is on the order of 10^{20} cm^{-3}, as expected for a typical semiconductor as AZO. The maximum number of carriers occurs at x = 1 on silica and at x = 2 on Al_2O_3. The carrier mobility has the maximum at x = 2 on both substrates but is about 20 times larger on AZO_2A than on AZO_2S. AZO_0S has larger mobility than AZO_0A and this can be explained with the larger amount of misfit dislocations generated on Al_2O_3, due to a lattice misfit of 15% [56,191]. Surprisingly, with increasing the content of SnO_2 doping, there was a reversal trend and the films grown on Al_2O_3 presented higher mobility, with the maximum value for AZO_2A - 20 times larger than for AZO_0S.
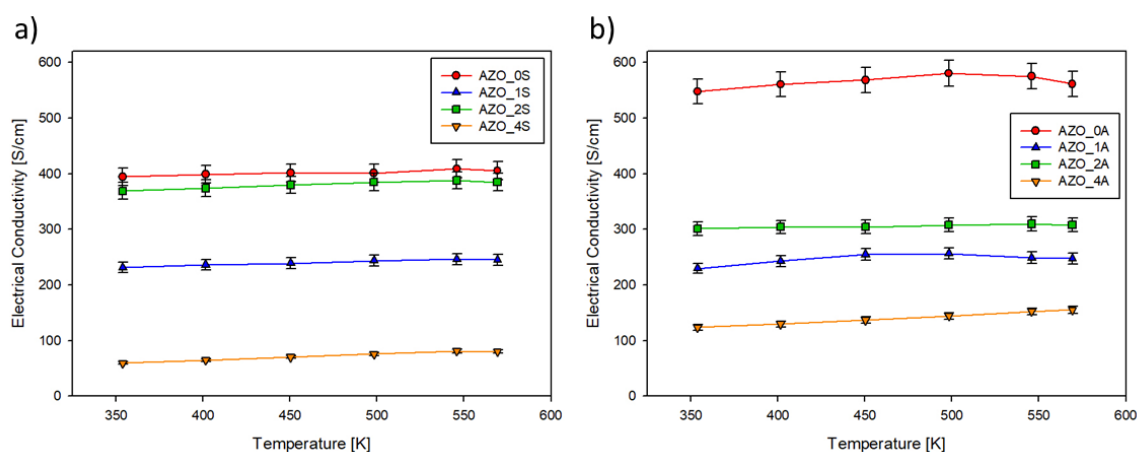
Figure 81 - Trend of the electrical conductivity vs. temperature of thin films deposited on (a) silica (series AZO_xS); (b) on Al_2O_3 (series AZO_xA) [175].

The electrical conductivity for the AZO films is presented in Figure 81 as a function of temperature in the range 300-600 K. The figure shows that σ increases with the rising temperature, confirming the semiconducting behaviour of materials. On both substrates, the film grown without additional SnO_2 has the largest σ followed by the film with x = 2.
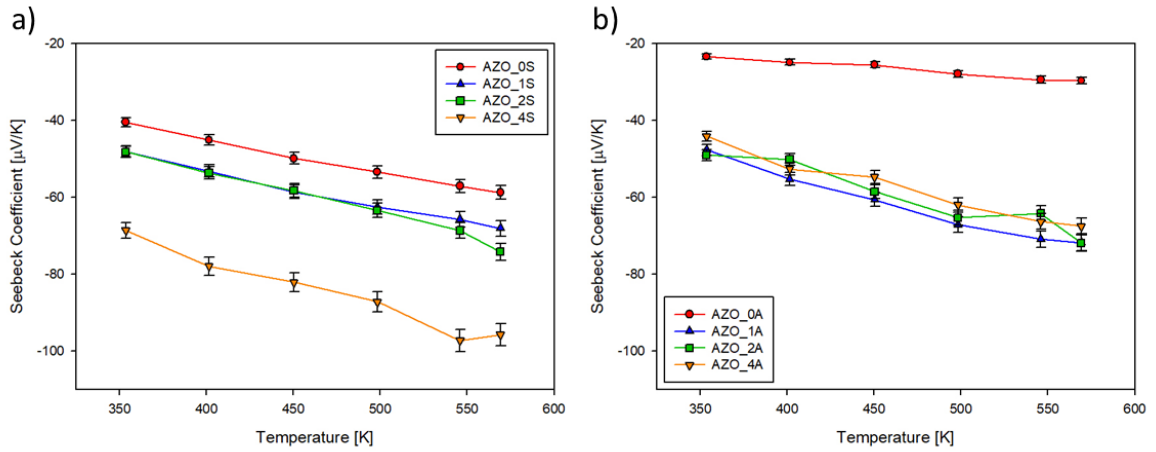
Figure 82 - Trend of the Seebeck coefficient vs. temperature of thin films deposited on (a) silica (series AZO_xS); (b) on Al_2O_3 (series AZO_xA) [175].

The temperature dependence (300-600 K) of Seebeck coefficient for the AZO films is plotted in Figure 82. *S* has a negative sign, confirming the *n*-type conducting behaviour of AZO. Figure 82 shows that *S* decreases with the rising temperature, a reversal trend with respect to σ as commonly expected for semiconductor materials. On both substrates, the pure AZO film had the lowest *S* while the sample fabricated with target containing 4% of SnO_2 presents the largest one.
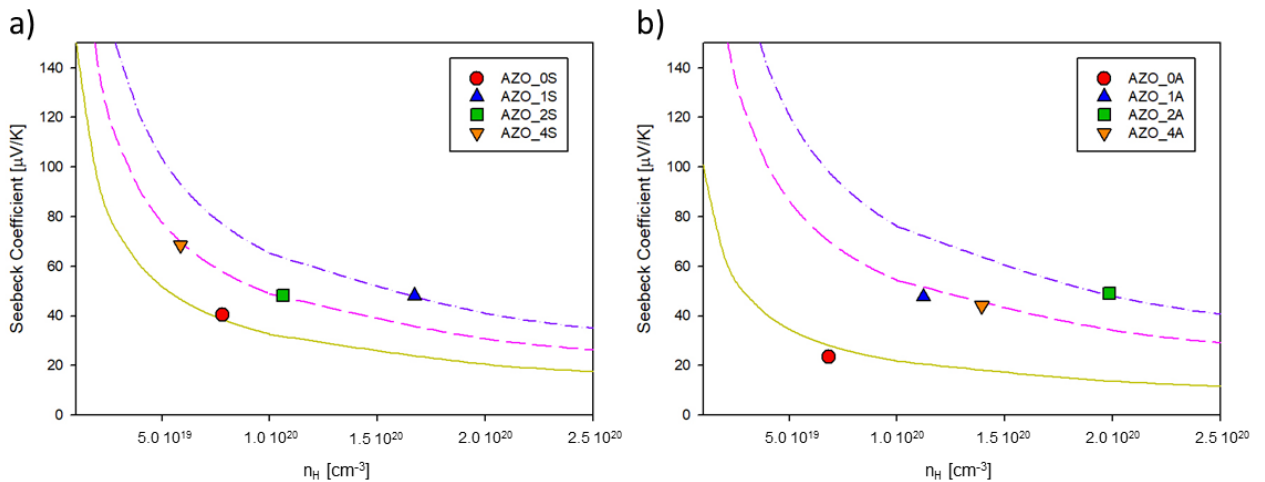
Figure 83 - Pisarenko plot at 300K for thin films deposited on (a) silica (series AZO_xS); (b) on Al_2O_3 (series AZO_xA) [175].

The Seebeck coefficient can be expressed as the previous Equation 5, reported here again for sake of clarity:

$$S = \left(\frac{8\pi^2 k_B^2}{3eh^2}\right) m^* T \left(\frac{\pi}{3n}\right)^{2/3} \tag{5}$$

where k_B is Boltzmann's constant, h is Planck's constant, T is the absolute temperature, m^* is the effective mass and n is the carrier concentration. The effective mass is also expressed as $m^* = \alpha\, m_e$, where m_e is the mass of the electron and α is a positive rational number.

The room temperature (300 K) "Pisarenko plots" (S versus n_H) for both series of films are reported in Figure 83 According to the graphs, m^* was (0.3-0.6) m_e and (0.2-0.7) m_e for the films grown on silica and alumina, respectively. The fractional m_e is consistent with a parabolic band approximation and the relatively simple band structure reported for ZnO [192].
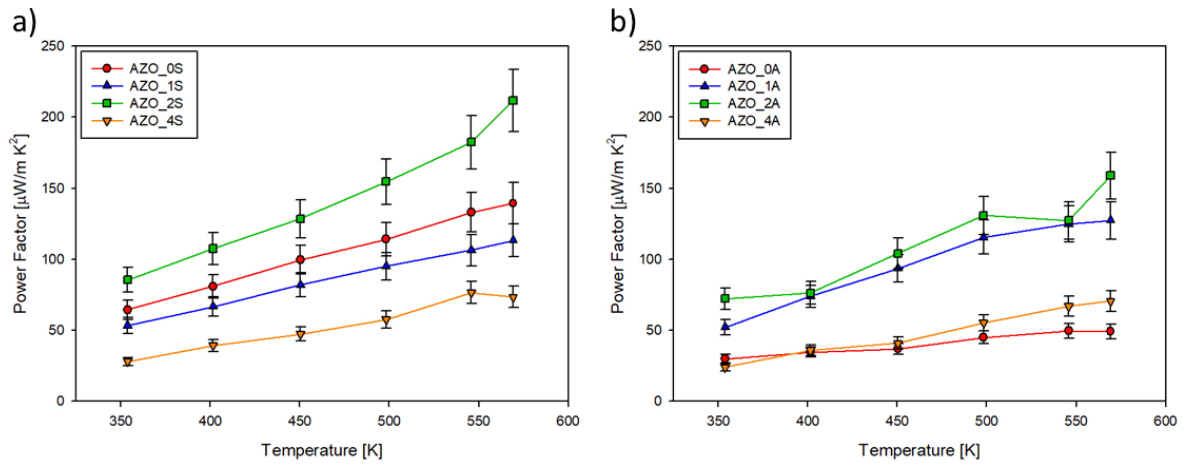
Figure 84 - Trend of the power factor vs. temperature of thin films deposited on (a) silica (series AZO_xS); (b) on Al₂O₃ (series AZO_xA) [175].

The calculated power factor (*PF*) as a function of temperature is shown in Figure 84. The maximum power factor value is found for sample AZO_2S at 573K as 211.78 μW/m·K^2. This value lies on the same order of magnitude as the one measured on bulk AZO in the same conditions (340 μW/m·K^2 [194]) and is also comparable with the values reported for AZO thin films [54,56,126,130,132,133,134].

The *PFs* of all films at 353K and 573K are summarized in Figure 85 making clear that on both substrates, 2% of SnO₂ represents the optimal dopant`s concentration.
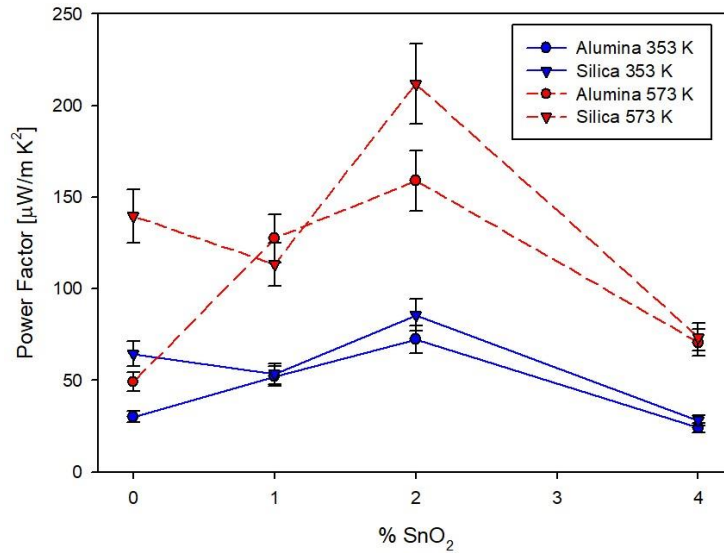
Figure 85 - The trend of power factor with the content of SnO₂ for the two series of films on silica and alumina at 353 and 573 K [175].

For the films AZO_0S and AZO_2S deposited on silica the measurements were repeated using two different apparatuses to verify accuracy the reproducibility of data.

A summary of the transport and thermoelectric properties of the films of AZO_xS and AZO_xA series is reported in Table 9.

Table 9 - Thickness, electrical and thermoelectric properties of the AZO films deposited on silica (series AZO_xS) and on A_l2O_3 (series AZO_xA) with x = % of SnO₂ dopant

Sample	Thickness [nm]	n_H [cm⁻³]	μ_H [cm²/V·s]	s [S/cm]		S [μV/K]		PF [μW/m·K²]		κ [W/m·K]
		(300 K)	(300 K)	(353 K)	(573K)	(353 K)	(573K)	(353 K)	(573K)	(300 K)
AZO_0S	595	-7.812 10⁺¹⁹	3.571	394.7	405.3	-40.41	-58.66	64.47	139.5	8.88
AZO_1S	505	-1.671 10⁺²⁰	4.503	231.2	245.0	-48.07	-68.02	53.43	113.4	-
AZO_2S	300	-1.061 10⁺²⁰	7.119	369.2	385.0	-48.13	-74.17	85.54	211.8	8.56
AZO_4S	295	-5.865 10⁺¹⁹	0.8606	59.63	80.23	-68.57	-95.73	28.03	70.70	-
AZO_0A	535	-6.832 10⁺¹⁹	2.576	547.8	561.4	-23.38	-29.61	29.94	49.21	-
AZO_1A	498	-1.124 10⁺²⁰	6.345	229.8	247.7	-47.66	-71.72	52.19	127.4	-
AZO_2A	535	-1.986 10⁺²⁰	125.1	301.4	307.6	-49.00	-71.87	72.38	158.9	-
AZO_4A	480	-1.394 10⁺²⁰	2.143	123.7	155.4	-44.06	-67.45	24.01	70.70	-

The room temperature (300 K) thermal conductivity (κ) of the sample with the highest *PF* (AZO_2S) and of a reference sample of the same batch (AZO_0S) was evaluated by the TD-TR method [178,179,180,193]. The value of κ was 8.88 and 8.56 W/m·K for samples AZO_0S and AZO_2S, respectively. These values were in the same range as those reported for pure AZO films deposited by PLD [54,56,128]. So the 4 times decrease of κ with respect to bulk [194] must be attributed to the phonon scattering of grain boundaries, and not to the addition of SnO₂. The calculation of *ZT* (*T* = 353 K) using equation (2) gave the following

result: ZT (AZO_0S) = 0.003 and ZT (AZO_2S) = 0.004, of the same order as for AZO thin film deposited by PLD on different substrates. Conservative estimates of $ZT^`$ ($T^`$ = 573 K) were $ZT^`$ (AZO_0S) = 0.009 and $ZT^`$ (AZO_2S) = 0.014. Since oxide thin films κ is expected to decrease with T [195], ZT was calculated using a conservative approach from the PF values at 353 K or 573 K, κ at 300 K, and $T =$ 353 K or 573 K.

These values of ZT did not surpass the reported performance of bulk AZO at the same conditions and were also of the same or lower level as for other AZO films prepared by PLD. This indicated that SnO_2 could not be considered as an optimal dopant for AZO thin films for thermoelectric applications. On the other hand, it could be that the fine dispersion of SnO_2 into AZO matrix enhanced the photoelectric response of AZO, as reported for SnO_2/ZnO hierarchical nanostructures prepared by electrospinning method [196], or can be used to fabricate compact gas sensors, as reported for ZnO–SnO_2 nanofibers [197].

5.1.3   Conclusions

In summary, we fabricated using pulsed laser deposition (PLD) two series of thermoelectric thin films of Al-doped ZnO (AZO) doped with various concentrations of SnO_2 (x = 0, 1, 2, 4 wt%) on the substrates made of fused silica and Al_2O_3 (001) single crystals. The goal was to enhance thermoelectric performance. All the films were c-axis oriented. The films deposited on silica showed the highest values of Seebeck coefficient (S) and power factor (PF) in comparison with the films on Al_2O_3 with the same content of SnO_2. The AZO film on silica with x = 2 showed the best performance, with σ = 385.0 S/cm, S = -74.17 mV/K, and $PF =$ 211.8 μW/m·K^2 at the maximum operating temperature (573 K). The room temperature (300 K) thermal conductivity of this sample was evaluated as κ = 8.56 W/ m·K, with a calculated figure of merit ZT (353 K) = 0.003 and a projected value of ZT (573 K) = 0.014, comparable with ZT of the nanostructured PLD AZO films grown on several substrates.

6 COBALT-DOPED COPPER ALUMINUM OXIDE

6.1 Strongly *c*-axis Textured Pure and Co-Doped CuAlO₂ Films Obtained by Pulsed Laser Deposition

In order to assemble a TE device, both *n-* and *p-* type materials are needed. After investigating AZO thin films in the previous section, which is an *n*-type material, we present here a preliminary study regarding the *p*-type CuAlO₂. Copper aluminium oxide is a transparent semiconductor whose optoelectronic, electrical, and thermoelectric properties have attracted attention, especially since the discovery of its *p*-type character by Kawazoe et al in 1997 [198]. *p*-type transparent conductors are much less common than their *n*-type commercially available counterparts (tin selenium oxide, ITO). This fact hinders the development of practical transparent electronic devices based on *p-n* junctions [199].

On the other hand, CuAlO₂ and other delafossite oxides have been considered promising candidates as thermoelectric materials. They show high values of their Seebeck coefficient *S* and, at least in principle, it is possible to tune their electrical and thermal transport by proper control of their microstructure and chemical composition [200].

In the delafossite structure, each Cu atom is linearly coordinated with two O atoms, forming O–Cu–O dumbbells parallel to the *c* axis (Figure 86). Oxygens in these O–Cu–O units are also each coordinated to three Al atoms (in the figure, M^{III}), oriented such that Al-centered octahedra form AlO₂ layers, which lie parallel to the *ab* plane [201].

Amongst the different synthesis methods that have been explored for deposition of CuAlO₂ films, as pulsed laser deposition [198,202, 203], sputtering [204,205], spin-coating [206] or spray [207], PLD and sputtering are preferred due to the prospect of easier application for the fabrication of electronic devices. From a practical point of view, low or moderate deposition temperatures, eventually combined with simple heat treatment procedures, would be advantageous.

In this chapter, made in collaboration with prof. Marco A. López de la Torre (University of Castilla-La Mancha, Ciudad Real, Spain), we will describe our efforts to synthesize pure and Co-doped $CuAlO_2$ films by means of pulsed laser deposition (PLD). The results of structural and physical properties characterization experiments will be presented and discussed.
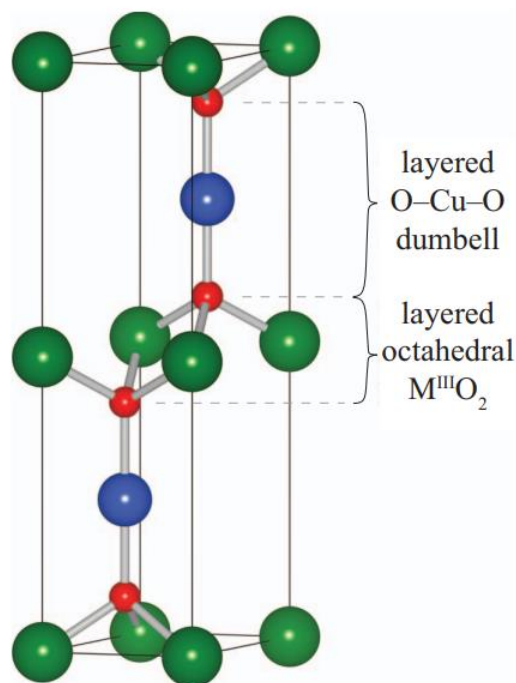
Figure 86 - The hexagonal delafossite structure. The green, red, and blue spheres are M^{III} (= Al,Cr,Sc,Y), O, and Cu [201].

6.1.1 Materials and Methods

Thin films of pure and Co-doped $CuAlO_2$ (Co-$CuAlO_2$ from now on) were obtained using Pulsed Laser Deposition (PLD) in a vacuum chamber. A sintered ceramic disk of $CuAlO_2$ (Toshima Limited, Tokyo) was used as target. In the case of Co-$CuAlO_2$, a composite target consisting of Co chips glued on the $CuAlO_2$ disk was used instead. A Nd:YAG laser from Advanced Optics Vacuum, operating at 10 Hz frequency and 266 nm wavelength, was used. Substrates were glued with silver paste on an Inconel plate attached to the heater. Target-substrate distance was fixed at 35 mm. Before every deposition the vacuum chamber was pumped down with a molecular pump down to a base pressure of around $2 \cdot 10^{-5}$ Torr. Two sets

of films were grown on *c*-axis (0001) oriented sapphire substrates using two different procedures:

Table 10 - Deposition parameters for pure and Co-doped CuAlO$_2$ samples[1].

SET	Deposition Temperature [°C]	Deposition Atmosphere O$_2$ [Torr]	Deposition time [min]	Cooling Atmosphere O$_2$ [Torr]	*In-situ* Annealing [min-°C]	*Ex-situ* Annealing [min-°C]
A	700	0.2	15	200	60-700	-
A	700	0.2	30	200	60-700	-
A	700	0.2	60	200	60-700	-
A	750	0.2	15	200	60-750	-
A	750	0.2	30	200	60-750	-
A	750	0.2	60	200	60-750	-
A	800	0.2	15	200	60-800	-
A	800	0.2	30	200	60-800	-
A	800	0.2	60	200	60-800	-
B	400	0.01	60	0.01	-	180-900
B	450	0.01	60	0.01	-	180-900
B	400	0.01	60	0.01	-	180-1003
B	450	0.01	60	0.01	-	180-1003
B	400	0.01	60	0.01	-	180-1040

In both cases, sapphire substrates were cleaned by means of heat treatment at 1000 °C in air for 60 minutes and subsequent furnace cooling to room temperature, in air. Film thickness (*t*) was estimated, for selected samples, using stylus profilometry (Sloan Dektak), AFM measurements, or low angle XRD for *t* values below 100 nm.

Structural characterization of the films was performed by means of X-ray diffraction experiments, both at Shibaura Institute of Technology and Universidad the Castilla-La Mancha, and using X-ray photoemission a Raman spectroscopy at Instituto de Ciencias Moleculares (Universidad de Valencia). Morphology and chemical composition studies were carried out, both at Tokyo and Ciudad Real, using two different field emission electron microscopes.

---

[1] These deposition parameters are the same for both pure and Co-doped CuAlO$_2$ batches of samples.

6.1.2 Results and Discussion

6.1.2.1 X-ray diffraction measurements

In Figure 87 we display the results of XRD measurements performed in selected samples of set A (CuAlO$_2$ and Co-CuAlO$_2$ films, deposited at 700, 750, and 800 °C, for 60 minutes). All the patterns show a very strong peak at 41.6°, corresponding to the (0006) Al$_2$O$_3$ reflection coming from the sapphire substrate. Weaker reflections corresponding to the
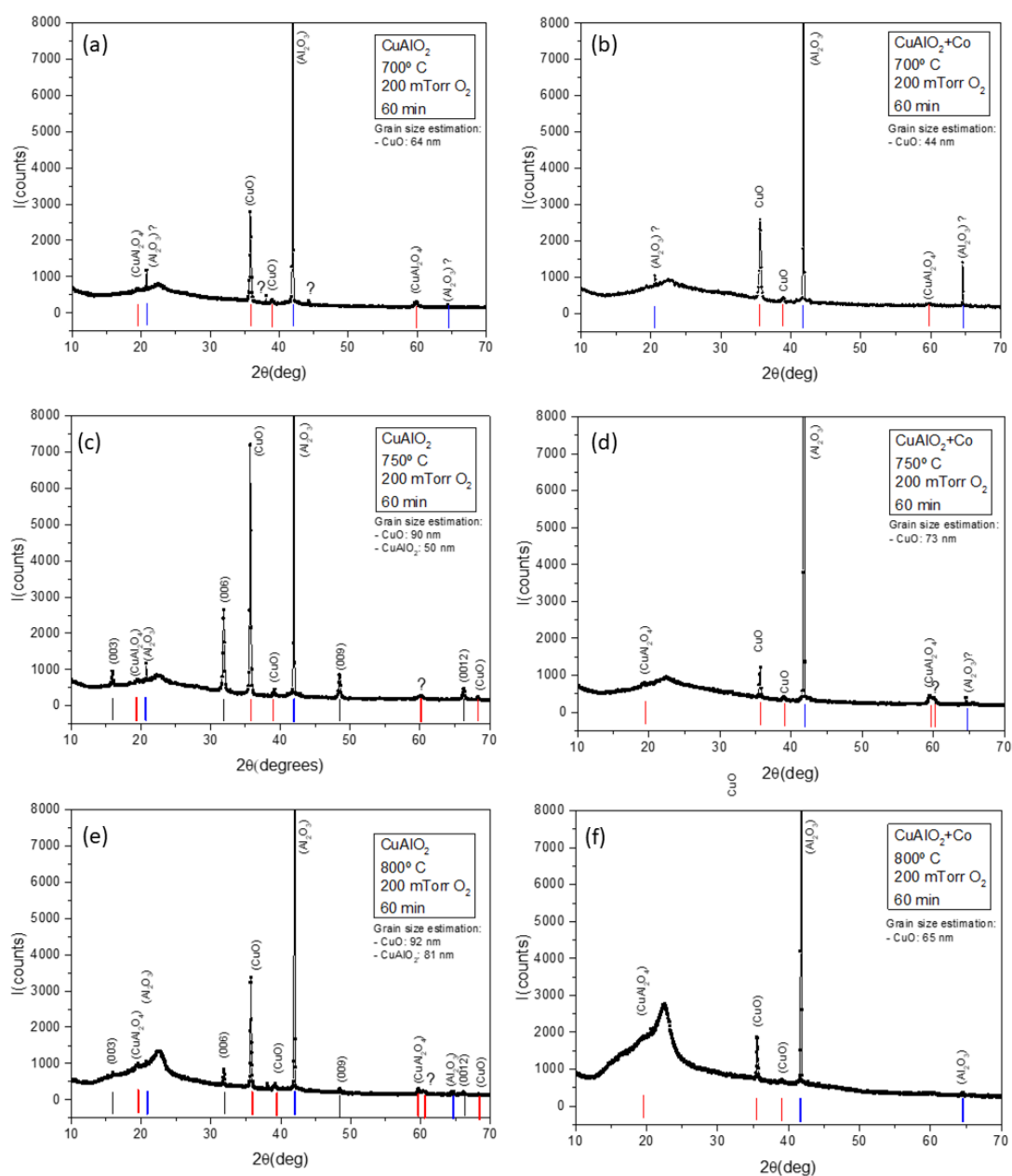
Figure 87 - XRD patterns of selected CuAlO$_2$ and Co-CuAlO$_2$ films of set A.

substrate can be observed at 20.5° and 64.5°. For all films, peaks corresponding to $CuAlO_2$, CuO and $CuAl_2O_4$ are observed, on top of a broad "amorphous halo".

In the case of films grown at 700 °C in Figure 87a and Figure 87b, no $CuAlO_2$ (delafossite structure) peaks were observed. Apart from the substrate peaks, only an amorphous-like background plus peaks corresponding to CuO and $CuAl_2O_4$ phases are detected. In the pure $CuAlO_2$ film, two very small unidentified peaks can be seen too.

Regarding the films grown at 750 °C, pure $CuAlO_2$ display delafossite peaks consistent with a very strong *c*-axis preferential orientation, i.e. (003), (006), (009) and (0012) are much more intense than the (101) and (012), the main peaks for bulk polycrystalline samples. As a matter of fact, these last peaks are not observed at all in this sample. As in the previous case, an amorphous-like background plus peaks corresponding to secondary CuO and $CuAl_2O_4$ phases are observed. A weak unidentified peak is observed at 60.5 degrees. On the other hand, Co seems to inhibit $CuAlO_2$ crystallization for this growth temperature, as only peaks corresponding to CuO and $CuAl_2O_4$ phases are detected.

Finally, pure $CuAlO_2$ grown at 800 °C also display delafossite peaks consistent with *c*-axis preferential but weaker than those observed for the 750 °C films. As in the previous case, an amorphous-like background, slightly different to that observed for the other growth temperatures, plus other peaks corresponding to CuO and $CuAl_2O_4$ phases, are observed in the patterns. These peaks are also weaker than for 750 °C films. A weak unidentified peak is observed at 60.5 degrees. Once again, Co seems to inhibit $CuAlO_2$ crystallization for this growth temperature.

From the width of the (006) peak in Figure 87c, using the Scherrer formula it is possible to estimate a crystallite size (*d*) of the delafossite phase similar to 60 nm. This can be done also for the secondary phases observed in the other films, which results in *d* values ranging between 40 and 90 nm. Complementary low angle XRD experiments allowed us to estimate a film thickness of around 60 nm for both $CuAlO_2$ and Co-$CuAlO_2$ grown for 60 minutes. The fact that *d* (crystalline coherence length in out of plane direction) equals the film thickness points to a pseudomorphic growth mode of the delafossite phase on the sapphire substrate.

Obviously, the films need a post-annealing treatment. Considering the $CuAlO_2$ phase diagram reported in reference [208], these films would require treatment at a temperature between 1000° C and 1100° C, for a time of 1 hour or longer at low O_2 pressure, to achieve

proper growth of the $CuAlO_2$ phase. For that reason, we decide to change our strategy. So, for set B the deposition was performed at lower temperatures (400 °C and 450 °C), and lower oxygen pressure (10 mTorr), which is advantageous from a technical point of view (heater endurance), followed by subsequent heat treatments in rotary pump vacuum.
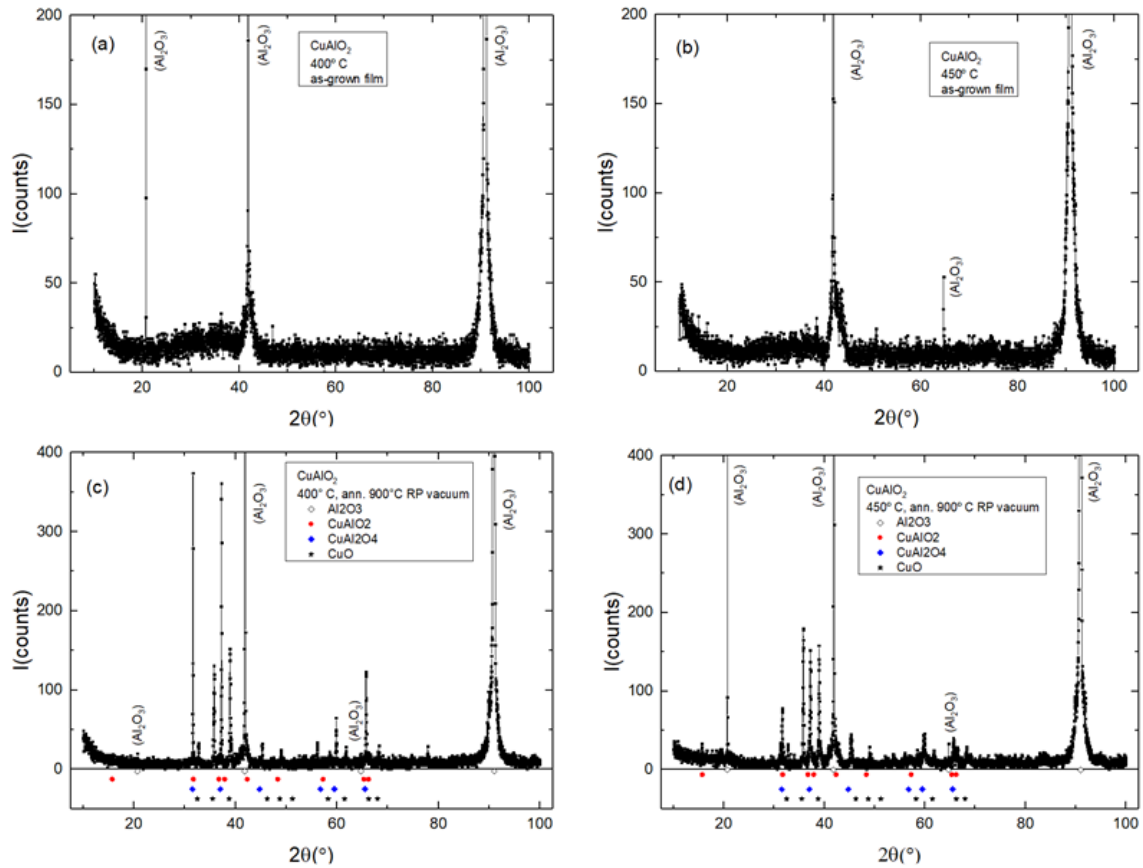
Figure 88 - XRD patterns of selected $CuAlO_2$ and Co-$CuAlO_2$ films of set B.

In Figure 88 we display the results of XRD measurements performed at SIT in selected samples of set B. As-grown samples at 400 °C and 450 °C (Figure 88a and Figure 88b) show a weak and broad amorphous "halo", on top of which only the very strong and narrow peaks associated with the sapphire substrate can be observed.

Annealing at 900 °C results, for both deposition temperatures, in crystallization of the amorphous precursor, not in a single $CuAlO_2$ phase, but a complex mixture of the delafossite phase with CuO and $CuAl_2O_4$ phases (Figure 88c and Figure 88d). Practically all the significant peaks in these two patterns can be indexed to the main peaks of those three phases. This means that annealing at 900 °C is not enough to complete the reaction of CuO and $CuAl_2O_4$ to $CuAlO_2$.

Following reference [208], we chose two heat treatment temperatures of 1003 °C and 1040° C, hoping to ensure the formation of single-phase $CuAlO_2$ films. For this last experiment,

the deposition temperature of 400 °C, the most convenient for our PLD system, was selected, and two $CuAlO_2$ and $Co\text{-}CuAlO_2$ films were deposited. The corresponding XRD patterns are displayed in Figure 89a and Figure 89b. It is readily observed that, for pure $CuAlO_2$ films, heat treatment at 1003º C is partially successful and fully successful in the case of 1040º C. The sample annealed at 1003ºC (Figure 89a) shows three $CuAlO_2$ phase peaks consisting of *c*-axis textured growth: (003), (006) and (009). Besides that, (101) and (012) $CuAlO_2$ peaks are also observed. No peaks associated with other phases were detected. This pattern looks essentially like that shown by Kawazoe et al. in reference [198]. Regarding the film annealed at 1040 ºC (Figure 89c), an extra (0012) peak consisting of *c*-axis textured growth is observed. Please observe the enhanced intensity and sharpness of these peaks. So, the pattern displayed in Figure 89 indicates the growth of almost pure $CuAlO_2$ delafossite films on sapphire with a strong *c*-axis texture.
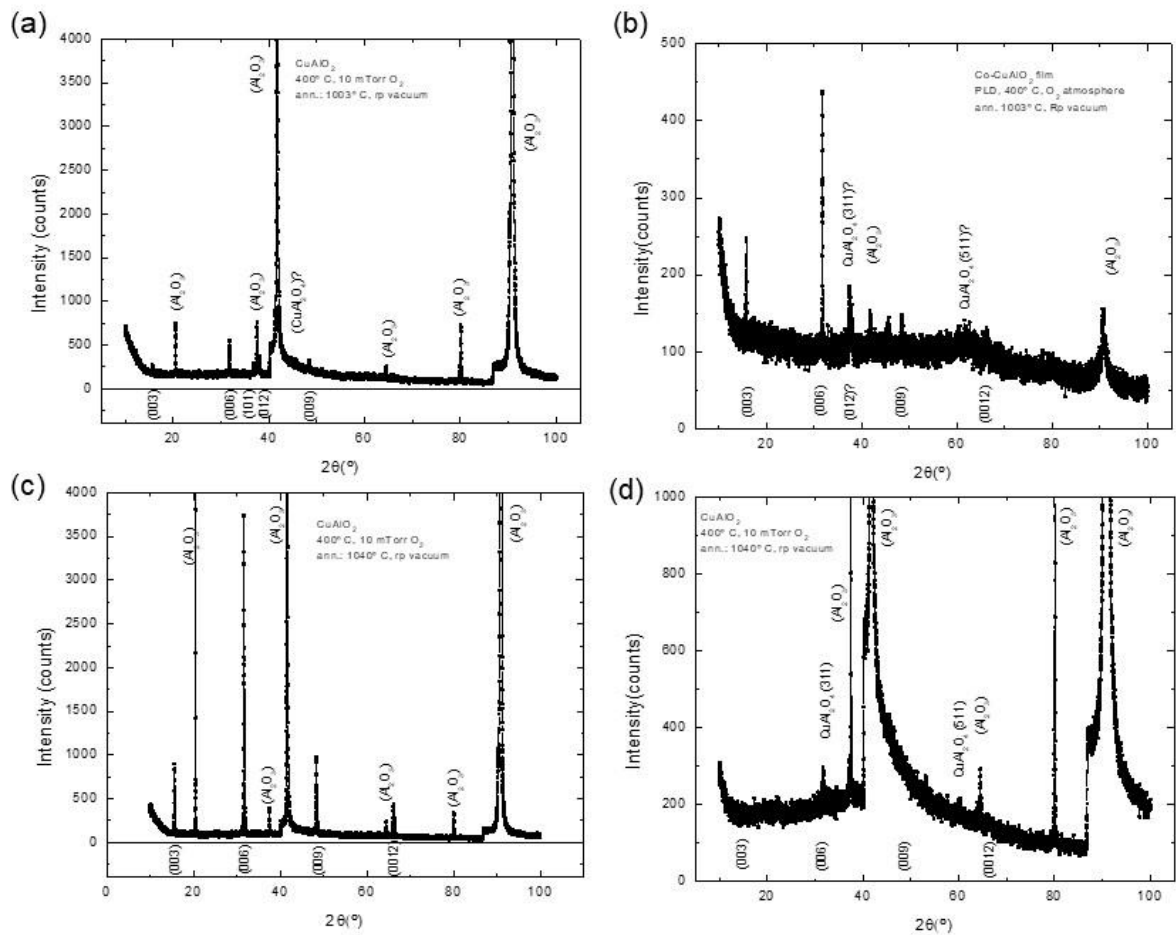
Figure 89 - XRD patterns of films of set B annealed at 1003°C and 1040°C.

The effect of annealing at 1003 °C and 1040 ºC is different in the case of $Co\text{-}CuAlO_2$ films. Whereas the $Co\text{-}CuAlO_2$ film pattern is consisting of a $CuAlO_2$ phase majority phase, hints of a residual $CuAl_2O_4$ phase are observed in the pattern displayed in Figure 89b. Please

notice the reduced crystallinity of the film and the diminished contribution of the Al_2O_3 peaks. For the Co-CuAlO$_2$ films, the patterns were repeated several times, as the height of the substrate peaks strongly changed between different runs. The most representative runs are shown in Figure 89.

Finally, annealing at 1040 ℃ seems to induce the partial decomposition of the CuAlO$_2$ phase, as the XRD pattern (Figure 89d), shows a mixture of CuAlO$_2$ and $CuAl_2O_4$ peaks. Please notice the reduced crystallinity of the film.

In the following sections, we will present the results of complementary characterization experiments, with the aim of confirming the results of the XRD experiments.

6.1.2.2 AFM and profilometry
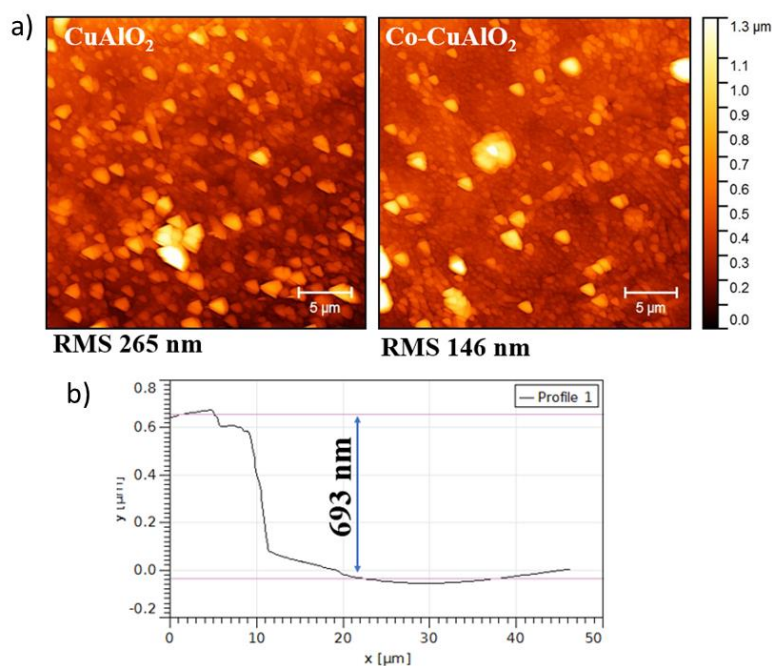
Figure 90 - a) AFM images of selected CuAlO$_2$ and Co-CuAlO$_2$ films of set B. b) Profile measurements of the step for the CuAlO$_2$ sample.

Profilometry measurements were performed for the CuAlO$_2$ and Co-CuAlO$_2$ films annealed at 1003 °C. The results were 850 ± 50 nm for the CuAlO$_2$ film, and 950 ± 50 nm for the Co-CuAlO$_2$ film. These results are consistent with the results of AFM in two especially step-graded samples, showing steps of around 700 nm (Figure 90). The morphology of both samples is similar, showing micrometre-sized structures with quite homogeneous distribution.

The size distribution seems to be quite narrow too. The only significant difference between both films is the smaller roughness of the Co-CuAlO$_2$ film (146 vs 265 nm).

6.1.2.3   Raman spectroscopy

The effect of annealing at 1040 °C on CuAlO$_2$ and Co-CuAlO$_2$ films was studied by means of Raman spectroscopy experiments performed on the very same samples used for XRD experiments. The results are shown in Figure 91a and Figure 91b. For the pure CuAlO$_2$ film,
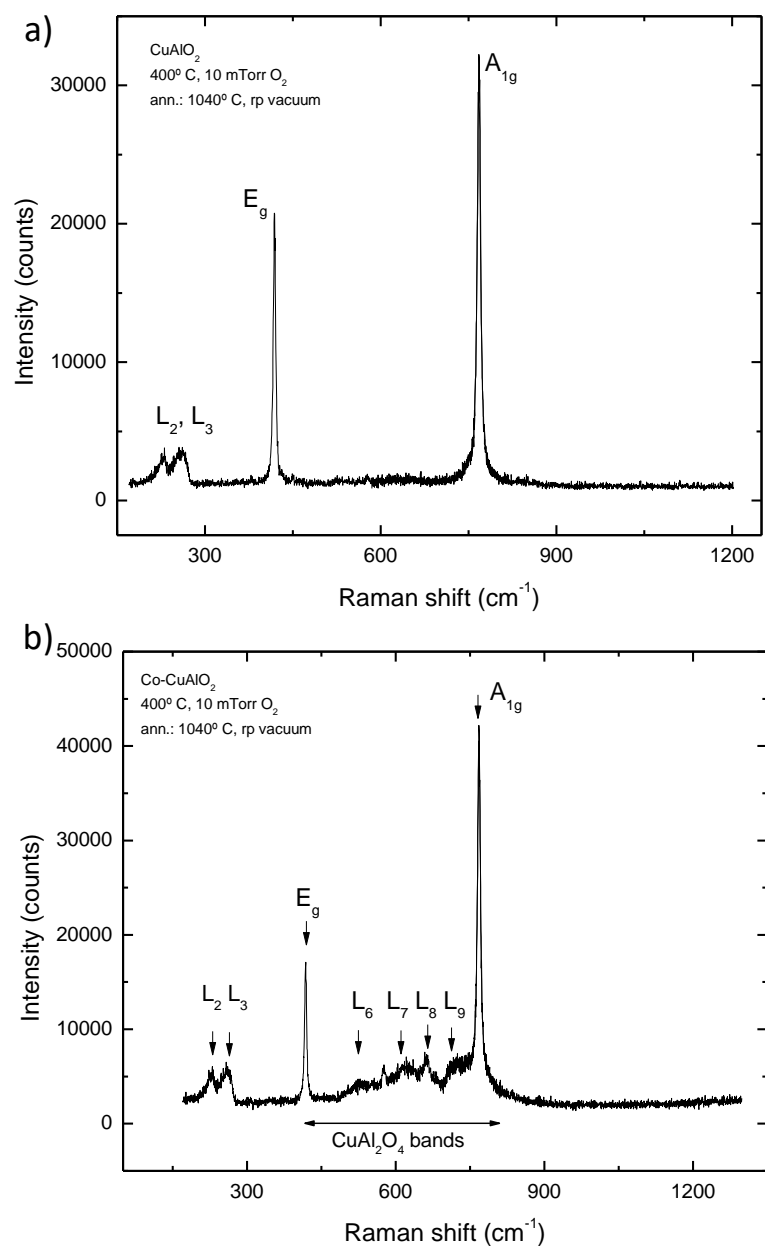
Figure 91 - Raman spectra of CuAlO$_2$ and Co-CuAlO$_2$ films annealed at 1040º C.

the Raman spectrum displayed is fully consisting with previous reports for single crystalline for single-crystalline, thin film or polycrystalline $CuAlO_2$ delafossite [209,210,211,212]. The Raman spectrum shown in Figure 91a shows two main peaks at 768 and 418 cm^{-1}, which can be identified as the A_{1g} and E_g Raman active peaks of the delafossite structure. The two broad peaks observed at 227 and 260 cm^{-1} can be associated to the L_2 and L_3 forbidden Raman modes reported by Pellicer-Torres et al. [209]. Following these authors, these modes are activated by defects in the crystalline structure and have been observed by other authors [211,212]. Regarding the spectrum corresponding to a Co-$CuAlO_2$ film annealed at 1040 ºC, displayed in Figure 91b, the A_{1g} and E_g Raman modes of the delafossite structure are clearly observed, but on top of a wide structure, ranging from 400 to 800 cm^{-1}, consistent with the superposition of wide Raman bands reported by different authors for $CuAl_2O_4$ [213,214]. On the other hand, the features related to the L_2 and L_3 modes, and other weak peaks possible related with L_4 to L_9 forbidden Raman modes, perhaps "activated" by structural defects, are observed too. In any case, the results of Raman spectroscopy experiments are consisting of those of XRD measurements.

6.1.2.4 XPS spectroscopy

To complete the structural characterization of $CuAlO_2$ and Co- $CuAlO_2$ films annealed at 1003 ºC and 1040 ºC, we performed X-ray photoemission spectroscopy (XPS) experiments at ICMOL (Universidad de Valencia, Spain).

In Figure 92 we show the Cu $2p$ core level spectra measured for the same samples used for XRD experiments. The spectra of the $CuAlO_2$, as well as that of the Co-CuAlO2 film annealed, are in good agreement with previous reports for pure delafossite $CuAlO_2$ [210,215]. The spectra are dominated by two peaks at ~ 933 eV (Cu+) and ~ 952.8 eV (Cu$^+$), which indicate that Cu cations mainly exist in Cu$^+$ form in a $CuAlO_2$ lattice. The satellites of the $2p_{3/2}$ and $2p_{1/2}$, as well as those observed between 941 and 948 eV indicated that Cu^{2+} state is presented in the films, even no $CuAl_2O_4$ or CuO peaks were detected by XRD in the samples annealed at 1003 ºC and 1040 ºC. On the other hand, the spectrum of the Co-$CuAlO_2$ film annealed at 1040 ºC, which shows an enhancement of the peaks associated to Cu^{2+} state, can be interpreted as the superposition of the Cu $2p$ spectra corresponding to coexisting $CuAlO_2$ and $CuAl_2O_4$ [230]. In

brief, the XPS results are in complete agreement with the results of our previous XRD and Raman spectroscopy experiments.
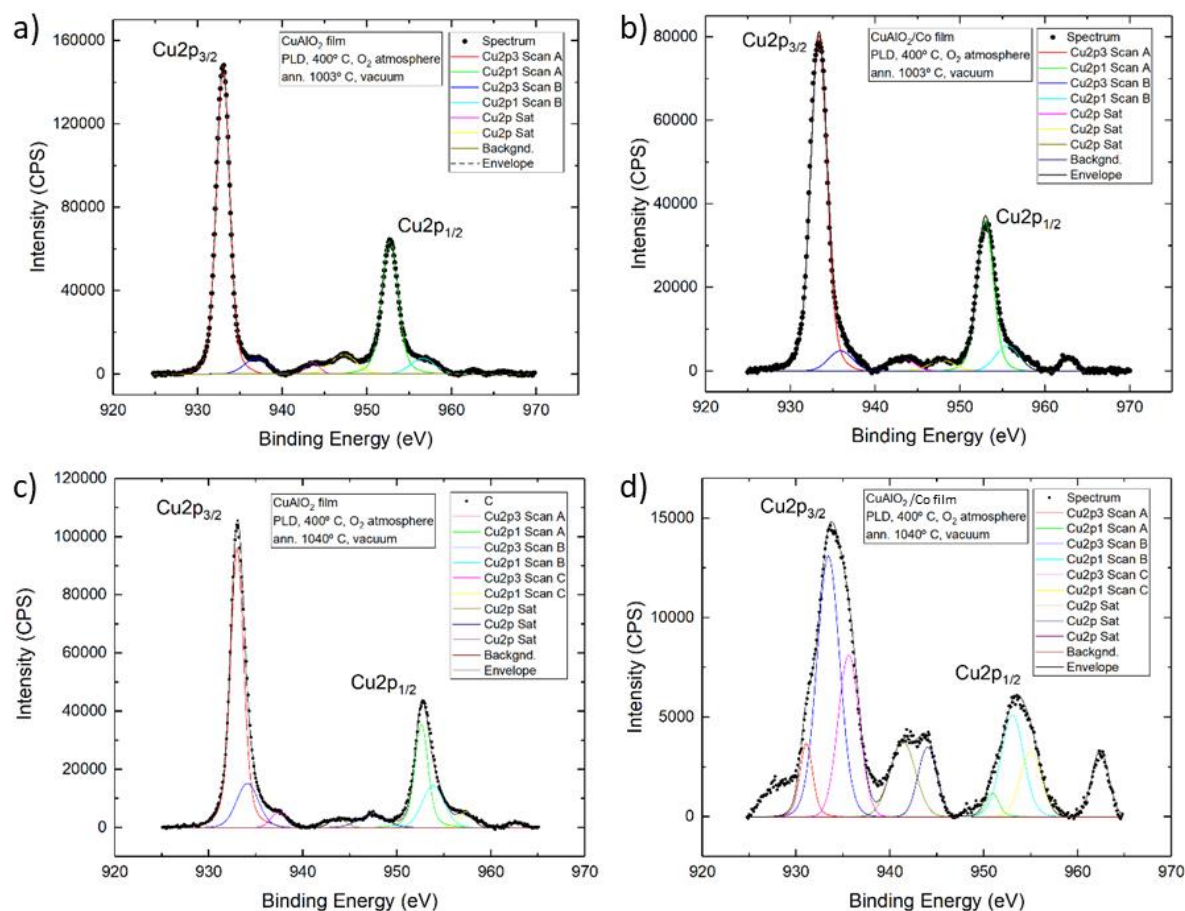
Figure 92 - Cu 2p XPS spectra of a) CuAlO₂ and b) Co-CuAlO₂ films annealed at 1003 ºC and c) CuAlO₂ and d) Co-CuAlO₂ films annealed at 1040 ºC.

6.1.2.5 Electrical conductivity and SQUID measurements

Preliminary electrical conductivity measurements failed due to the high resistance of the films, but allow us to estimate approximate conductivity values lower or equal than 0.01 $S \cdot cm^{-1}$. Electrical transport measurements are reported to be difficult in $CuAlO_2$ films [203,209]. The experimental difficulties maybe explain the wide ranges of conductivity values reported for this material, between 0.01 and 1 $S \cdot cm^{-1}$ in the case of films obtained by PLD or sputtering [198,202,208]. In the case of $Co-CuAlO_2$ samples, preliminary SQUID measurements show a small ferromagnetic signal in $Co-CuAlO_2$ films with features consistent with the presence of Co particles in our films.

6.1.3   Conclusions

This work is focused on the preliminary study of PLD thin films of $CuAlO_2$, which is considered a promising candidate as *p*-type thermoelectric material. Different temperatures and post-annealing (*in-situ* and *ex-situ*) conditions were explored. After a first structural investigation, we can report that we have synthesized excellent good quality pure delafosssite $CuAlO_2$ films displaying strong c-axis texture, by PLD deposition at 400 ºC on sapphire substrates, followed by annealing in rotary pump vacuum at 1040 ºC. For Co-$CuAlO_2$, annealing at 1003 ºC resulted also in films with delafossite structure, whereas the film annealed at 1040 ºC consist of a mixture of $CuAlO_2$ and $CuAl_2O_4$ phases. Deeper analyses are required to present a complete overview of the material. Electrical transport, SQUID and thermopower experiments in the best quality samples obtained in this work are currently underway.

7 CONCLUSIONS AND PERSPECTIVES

The increasing worldwide demand for energy and the resultant depletion of fossil fuels have brought new challenges for the scientific community. One of the major issues is to develop high-efficiency devices for capturing energy from abundant natural sources such as solar, wind and geothermal energy. Another surplus, but mostly unused, source of energy is wasted heat.

A greatly promising method for energy recovery from such heat sources is the application of thermoelectric (TE) materials that can convert numerous types of waste heat flow into electricity. The efficiency in the conversion of thermoelectric devices is determined by three main properties of the material, such as the electrical conductivity σ, the Seebeck coefficient S and thermal conductivity κ. The big challenge in this field is to positively tune the three aforementioned properties since they are interdependent.

Over the last decades, the necessity for employing micro-TE devices as a substitute power source for small electric devices and systems is expanding and the research in the micro-TE device is becoming vastly appealing. Since usual TE device making methods are not suitable for such miniaturized devices, small apparatuses based on thin films are one of the most extensively investigated research topics to achieve this objective. TE characteristics of a material are enhanced by nanostructurization, which is a typical property of thin films and they are considered a revolutionary way to decouple electrical and thermal transport properties, enhancing the overall TE efficiency.

As a consequence of what aforementioned, my PhD project is focused on the synthesis and characterization of TE thin films using the pulsed laser deposition (PLD) technique.

In Chapters 4.1, 4.2 and 4.3, novel studies regarding Fe,Ni-based skutterudites thin films are reported. Several studies regarding thermoelectric bulks belonging to the $Sm_y(Fe_xNi_{1-x})_4Sb_{12}$ system were conducted by our research group [34,41,42,45,138,141,142,143,144,145,182], anyway no extensive researches regarding filled skutterudites thin films are reported in the literature. To this purpose, thin films of the aforementioned composition were prepared by means of the PLD method under different conditions and TE properties were then investigated.

As a result of the first study reported in chapter 4.1, we understood the primary importance of the annealing process. For this reason, an extensive investigation regarding the annealing parameters of n-, p-type and the crossover compositions was carried on. Two times, three compositions and four temperatures were inspected, finding the best conditions in order to improve the efficiency of the material. Despite our efforts, the peak power factor value found was for the p-type composition and it is equal to 466 μW/m·K^2, that still be lower than the double-doped bulk ones [41], even if it is competitive with what reported in the literature for common Co-based skutterudites [51,185]. Further improvements could be done by the employment of multi-fillers in addition to Sm or doping at the Sb site. Measurements of carriers' concentration and mobility will need to be performed on the remaining films to clarify the correlation of the transport and thermoelectric properties with the annealing temperature. Moreover, from a preliminary cell parameter calculation, no correlation between annealing temperature and cell size was found, but better XRD patterns were acquired, More time is needed to complete good refinements.

Chapter 4.3 is dedicated to a preliminary study of the output power of an on-chip thermoelectric thin film module containing five n-type and five p-type skutterudite legs, fabricated on a fused silica substrate by the pulsed laser deposition technique. The performance of modules was measured using ad custom-made system. The output power showed a maximum of $P_{max} \approx 1.6 \cdot 10^{-7}$ W at 200 and 300 °C, which is 3 to 4 orders of magnitude better than what was reported by S. Saini et al [189] for oxides TE modules. Further studies will be carried out varying the composition of the targets and substrates in order to find the best possible performance.

In Chapters 5.1, AZO samples with the addition of different quantities of SnO_2 has been prepared by the PLD technique. Our purpose was trying to enhance the thermoelectric performance of AZO films by the addition of a controlled amount of SnO_2, hoping in the formation of favourable dispersed nanostructures. The best thermoelectric performance has been obtained for the AZO + 2% SnO_2 thin film grown on silica, with a power factor $PF = 211$ μW/m·K^2 at 568 K and a room- temperature (300 K) thermal conductivity of 8.56 W/m·K. PF is on the same order of magnitude as the value reported for typical AZO bulk material in the same measurement conditions (340 μW/m·K^2) while κ is reduced by about 5 times. This indicates that SnO_2 cannot be considered as an optimal dopant for AZO thin films for thermoelectric applications. On the other hand, it may be possible that the fine dispersion of

SnO_2 into the AZO matrix enhances the photoelectric response of AZO [196], or can be used to fabricate compact gas sensors, as reported for ZnO-SnO_2 nano-fibers [197].

Chapter 6.1 is dedicated to a preliminary study of PLD thin films of $CuAlO_2$, which is considered a promising candidate as p-type thermoelectric material. It generally shows high values of Seebeck coefficient S and, at least in principle, it is possible to tune its electrical and thermal transport by proper control of its microstructure and chemical composition [200]. p-type transparent TE materials are much less common than n-type ones, so $CuAlO_2$ is of noteworthy interest for transparent devices. Anyhow, only structural data are presented in this version of the thesis showing that good quality $CuAlO_2$ and Co-$CuAlO_2$ films were found for PLD deposited samples at 400 ℃ followed with an *ex-situ* annealing in rotary pump vacuum at 1003 ℃ and 1040 °C. Deeper investigations of the material will be performed soon.

LIST OF PUBLICATIONS

[1] **G. Latronico**, S. Singh, P. Mele, A. Darwish, S. Sarkisov, S.W. Pan, Y. Kawamura, C. Sekine, T. Baba, T. Mori, T. Takeuchi, A. Ichinose, S. Wilson, "Synthesis and Characterization of Al- and SnO_2-Doped ZnO Thermoelectric Thin Films", *Materials* 14 (2021) 6929.

[2] **G. Latronico**, P. Mele, C. Artini, P. Manfrinetti, S.W. Pan, Y. Kawamura, C. Sekine, S. Singh, T. Takeuchi, T. Baba, C. Bourgès, T. Mori, "Investigation on the power factor of skutterudite $Sm_y(Fe_xNi_{1-x})_4Sb_{12}$ thin films: Effects of deposition and annealing temperature", *Materials*, 14(19) (2021) 5773.

[3] C. Artini, A. Cingolani, F. Valenza, U. Anselmi-Tamburini, **G. Latronico**, P. Mele, "Effect of the sintering pressure on structure and microstructure of the filled skutterudite $Sm_y(Fe_xNi_{1-x})_4Sb_{12}$ (x = 0.50–0.80, y = 0.17–0.55)", *Mater. Res. Bull.,* 139 (2021) 11126.

[4] A. Phuangyod, J. Hayashi, Y. Kawamura, C. Artini, **G. Latronico**, R. Carlini, S. Saini, P. Mele, C. Sekine, "Low-Temperature thermoelectric properties of *p*-Type and *n*-Type filled skutterudite compounds $Sm_y(Fe_{1-x}Ni_x)_4Sb_{12}$ prepared under high pressure", *Jpn. J. Appl. Phys.,* 59 (2020) 061004.

[5] **G. Latronico**, F. Valenza, R. Carlini, P. Mele, C. Artini, "Interfacial Reactivity of the Filled Skutterudite $Sm_y(Fe_xNi_{1-x})_4Sb_{12}$ in Contact with Liquid In-Based Alloys and Sn", *Metals* 10 (2020) 364.

[6] R. Spotorno, G. Ghiara, **G. Latronico**, R. Carlini, P. Mele, C. Artini, "Corrosion of the Filled Skutterudite $Sm_{0.1}(Fe_{0.45}Ni_{0.55})_4Sb_{12}$ by NaCl Solutions: An Electrochemical Study", *J. Electron. Mater.,* 49 (2020) 1-9.

[7] C. Artini, **G. Latronico**, R. Carlini, S. Saini, T. Takeuchi, S. Choi, A. Baldini, U. Anselmi-Tamburini, F. Valenza, P. Mele, "Effect of different processing routes on the power factor of the filled skutterudite $Sm_y(Fe_xNi_{1-x})_4Sb_{12}$ (x = 0.50-0.80; y = 0.12-0.53)", *ES Mater. Manuf.,* 29 (2019) 29–37.

PRESENTATIONS

[1] ***Oral Presentation at Conference***: <u>**G. Latronico**</u>, P. Mele, P. Mele, C. Artini, P. Manfrinetti, C. Fanciulli, P.S. Wei, S. Singh, T. Takeuchi, C. Bourgès, T. Mori, C. Sekine "High-Power Factor of Fe,Ni-based Skutterudites Thin Films", Materials Research Meeting 2021, Yokohama (Japan), December 15th, 2021

[2] ***Invited Talk at Workshop***: <u>**G. Latronico**</u>, C. Artini, S. Singh, T. Takeuchi, P. S. Wei, Y. Kawamura, C. Sekine, C. Bourgès, T. Mori, P. Mele, "Systematic Study of Synthesis and Annealing on Fe-Ni Based Skutterudites Thin Films for Thermoelectric Purposes", Muroran Institute of technology Rare Earth Workshop 2021 (REWS2021), Online Virtual Meeting, October 27th-28th, 2021

[3] ***Oral Presentation at Conference***: <u>**G. Latronico**</u>, P. Mele, C. Artini, P. Manfrinetti, C. Fanciulli, S. Singh, T. Takeuchi, C. Bourgès, T. Mori, C. Sekine, "High-Power Factor and Annealing Optimization of Fe,Ni-based Skutterudites", 1st Japan-France Virtual Workshop on Thermoelectrics (VWT), Online Virtual Meeting, September 27th-30th, 2021

[4] ***Oral Presentation at Conference***: <u>**G. Latronico**</u>, C. Artini, P. Manfrinetti, C. Fanciulli, S. Singh, T. Takeuchi, P. Mele, "Systematic Study About the Annealing of Skutterudite $Sm_y(Fe_xNi_{1-x})_4Sb_{12}$ Thin Films", The 82nd Autumn Meeting 2021, The Japan Society of Applied Physics (JSAP), Online Virtual Meeting, September 10th-13th, 2021

[5] ***Oral Presentation at Conference***: <u>**G. Latronico**</u>, P. Mele, C. Artini, P. Manfrinetti, C. Fanciulli, U. Anselmi-Tamburini, P.S. Wei, Y. Kawamura, C. Sekine, T. Baba, C. Bourgès, T. Mori, "Effects of Annealing and Deposition Temperature on the Power Factor of $Sm_y(Fe_xNi_{1-x})_4Sb_{12}$ Thin Films", Virtual Conference on Thermoelectrics (VCT2021), Online Virtual Meeting, July 20th-22nd, 2021

[6] ***Oral Presentation at Conference***: <u>**G. Latronico**</u>, P. Mele, C. Artini, C. Fanciulli, P. Manfrinetti, M. Pani, F. Valente, I. Imae, K. Alok, S. Singh, T. Takeuchi, "Thermoelectric study of thin films of the filled skutterudite $Sm_y(Fe_xNi_{1-x})_4Sb_{12}$", 30th Annual Meeting of MRS-J, Online Virtual Meeting, December 9th-11th, 2020

[7] ***Oral Presentation at Workshop***: <u>**G. Latronico**</u>, P. Mele, C. Artini, F. Valenza, R. Spotorno, G. Ghiara, R. Carlini, S. Saini, S. Choi, S. Singh, T. Takeuchi, "Insights on the

skutterudite $Sm_y(Fe_xNi_{1-x})_4Sb_{12}$: wettability tests, corrosion behaviour and feasibility of thin films" Muroran IT REWS2020 Workshop, Online Virtual Meeting, October 28th, 2020

[8] ***Oral Presentation at Conference***: **G. Latronico**, P. Mele, C. Artini, C. Fanciulli, P. Manfrinetti, S. Singh, T. Takeuchi, "Study of thin films of the filled skutterudite $Sm_y(Fe_xNi_{1-x})_4Sb_{12}$", The 81st Autumn Meeting 2020, The Japan Society of Applied Physics (JSAP), Online Virtual Meeting, September 8th-11th, 2020

[9] ***Oral Presentation at Conference***: **G. Latronico**, P. Mele, C. Artini, C. Fanciulli, P. Manfrinetti, S. Singh, T. Takeuchi, "Preliminary study of thin films of the filled skutterudite $Sm_y(Fe_xNi_{1-x})_4Sb_{12}$", Virtual Conference on Thermoelectrics (VCT2020), Online Virtual Meeting, July 21st-23rd, 2020

[10] ***Oral Presentation at Conference***: **G. Latronico**, P. Mele, S. Saini, F. Valenza, R. Carlini, S. Choi, T. Takeuchi, A. Baldini, U. Anselmo-Tamburini, C. Artini, "Properties of the Thermoelectric Filled Skutterudite Belonging to the System $Sm_y(Fe_xNi_{1-x})_4Sb_{12}$", Materials Research Meeting 2019, Yokohama (Japan), December 10th-14th, 2019

[11] ***Oral Presentation at International School***: **G. Latronico**, "Properties of the Thermoelectric Filled Skutterudites Belonging to the System Smy(FexNi1-x)4Sb12", Course 207 "*Advances in Thermoelectricity: Fundational Issues, Materials and Nanotechnology*", International School of Physics "Enrico Fermi", Varenna (Italy), July 15th-20th, 2019

[12] ***Oral Presentation at Conference***: C. Artini, **G. Latronico**, R. Carlini, S. Saini, T. Takeuchi, S. Choi, A. Baldini, U. Anselmi-Tamburini, F. Valenza, P. Mele, "Wettability of the filled skutterudite $Sm_y(Fe_xNi_{1-x})_4Sb_{12}$ by Sn and In-based alloys", Days on Thermoelectricity, GiTe 2019, Bologna (Italy), February 20th- 21st 2019

[13] ***Oral Presentation at Conference***: **G. Latronico**, C. Artini, A. Castellero, M. Baricco, M.T. Buscaglia, R. Carlini, "Rapid Solidification of $Sm_y(Fe_xNi_{1-x})_4Sb_{12}$ (x = 0.45, 0.50, 0.70, 1) Thermoelectric compounds: effect on structure, microstructure and microhardness", Days on Thermoelectricity, GiTe 2018, Santa Margherita - GE - (Italy), February 21st- 22nd 2018

PRESENTATIONS AS CONTRIBUTING AUTHOR

[1] **_Oral Presentation at Conference_:** A. Cingolani, **G. Latronico**, R. Spotorno, F. Valenza, R. Carlini, U. Anselmi-Tamburini, P. Mele, C. Artini, "Effect of processing parameters on structure and microstructure of $Sm_y(Fe_xNi_{1-x})_4Sb_{12}$", Days on Thermoelectricity, GiTe 2021, Online Virtual Meeting, February 17th-18th, 2021

[2] **_Oral Presentation at Conference_:** P. Mele, S. Singh, T. Takeuchi, **G. Latronico**, S. Saini, T. Mori, T. Baba, A. Darwish, "Synthesis and characterization of SnO_2-doped AZO thermoelectric thin films", MRS-J, Online Virtual Meeting, December 9th, 2020

[3] **_Invited Oral at Workshop_:** P. Mele, C. Artini, **G. Latronico**, R. Spotorno, R. Carlini, A. Cingolani, S. Saini, T. Takeuchi, S. Choi, F. Failamani, T. Mori, A. Baldini, U. Anselmi-Tamburini, F. Valenza, "Synthesis and Characterization of Rare-Earth Filled Skutterudites $Sm_y(Fe_xNi_{1-x})_4Sb_{12}$ and $(Sm,Gd)_y(Fe_xNi_{1-x})_4Sb_{12}$" Muroran IT REWS2020 Workshop, Online Virtual Meeting, October 28th, 2020

[4] **_Invited Oral at Workshop_:** P. Mele, C. Artini, **G. Latronico**, R. Carlini, S. Saini, T. Takeuchi, S. Choi, T. Mori, A. Baldini, U. Anselmi-Tamburini, F. Valenza, "Synthesis and Characterization of Rare-Earth Filled Skutterudites $Sm_y(Fe_xNi_{1-x})_4Sb_{12}$ and $(Sm,Gd)_y(Fe_xNi_{1-x})_4Sb_{12}$", 2nd Manutec Workshop, Kyushu University, Fukuoka (Japan), November 2nd, 2019

[5] **_Invited Oral at Conference_:** P. Mele, C. Artini, **G. Latronico**, R. Carlini, S. Saini, T. Takeuchi, S. Choi, T. Mori, A. Baldini, U. Anselmi-Tamburini, F. Valenza, "Recent advances in thermoelectric thin films", PacRim 13, Okinawa (Japan), October 27th, 2019

[6] **_Oral Presentation at Conference_:** P. Mele, G. **Latronico**, F. Valenza, R. Carlini, C. Artini, "Interfacial reactivity of the filled skutterudite $Sm_y(Fe_xNi_{1-x})_4Sb_{12}$ in contact with Sn and In based alloys as revealed by the sessile drop method", ICT2019, Gyeonju (Korea), July 2nd, 2019

[7] **_Oral Presentation at Conference_:** C. Artini, **G. Latronico**, R. Carlini, S. Saini, T. Takeuchi, S. Choi, A. Baldini, U. Anselmi-Tamburini, F. Valenza, P. Mele, "How processing routes affect the power factor of the filled skutterudite Smy(FexNi1-x)4Sb12", Days on Thermoelectricity, GiTe 2019, Bologna (Italy), February 20th- 21st 2019

LIST OF FIGURES

REFERENCES

[1] iEA, "World total energy supply by source, 1971-2018" [Online]. Available: https://www.iea.org/data-and-statistics/charts/world-total-energy-supply-by-source-1971-2018.

[2] S. Chu, A. Majumdar, "Opportunities and challenges for a sustainable energy future", *Nature* **2012**, *488*, 294-303.

[3] Z. Şen, "Solar energy in progress and future research trends", *Prog. Energy Combust. Sci.* **2004**, *30*, 367-341.

[4] A. Zerrahn, "Wind Power and Externalities", *Ecol. Econ.* **2017**, *141*, 245-260.

[5] S. Ma, M. Lin, T.E. Lin, T. Lan, X. Liao, F. Maréchal, J. Van Herle, Y. Yang, C. Dong, L. Wang, "Fuel cell-battery hybrid systems for mobility and off-grid applications: A review", *Renew. Sust. Energ. Rev.* **2021**, *135*, 110119.

[6] C. Artini, "RE-doped ceria systems and their performance as solid electrolytes: a puzzling tangle of structural issues at the average and local scale", *Inorg. Chem.* **2018**, *57*, 13047-13062.

[7] "BP statistical review of world energy" **2021** [Online]. Available: https://www.bp.com/en/global/corporate/energy-economics/statistical-review-of-world-energy.html

[8] Annual energy flow charts by Lawrence Livermore Nat. Lab. [Online]. Available: https://flowcharts.llnl.gov/commodities/energy

[9] I.R. Cózar, T. Pujol, E. Massaguer, A. Massaguer, L. Montoro, J.R. Gonzàlez, M. Comamala, S. Ezzitouni, "Effects of module spatial distribution on the energy efficiency and electrical output of automotive thermoelectric generators", *Energies* **2021**, *14*, 2232.

[10] M.A. Zoui, S. Bentouba, J.G. Stocholm, M. Bourouis, "A review on thermoelectric generators: Progress and applications", *Energies* **2020**, *13*, 3606.

[11] T. M. Tritt and M. A. Subramanian, "Thermoelectric materials, phenomena, and applucations: a bird's eye view", *MRS Bull.* **2006**, *31*, 188-198.

[12] G. J. Snyder and E. S. Toberer, "Complex thermoelectric materials", *Nat. Mater.* **2008,** *7*, 105-114.

[13] T. J. Hendricks and D. T. Crane, "Thermoelectric energy recovery systems: thermal, thermoelectric, and structural considerations" in *Modules, systems, and applications in thermoelectrics*, D. Rowe, Ed., Boca Raton, FL: CRC Press, **2012**.

[14] D. Beretta, N. Neophytou, J.M. Hodges, M.G. Kanatzidis, D. Narducci, M. Martin- Gonzalez, M. Beekman, B. Balke, G. Cerretti, W. Tremel, A. Zevalkink, A.I. Hofmann, C. Müller, B.

Dörling, M. Campoy-Quiles, M. Caironi, "Thermoelectrics: From history, a window to the future, Materials Science and Engineering", *R: Reports* **2019**, *138*, 100501.

[15] E. Altenkirch, "Über den nutzeffekt der thermosäule", *Phys. Zeits.* **1909**, 10, 560 -580.

[16] J. He, T.M. Tritt, "Advances in thermoelectric materials research: Looking back and moving forward", *Science* **2017**, *357*, 1369.

[17] J. Yang, L. Xi, W. Qiu, L. Wu, X. Shi, L. Chen, J. Yang, W. Zhang, C. Uher, D.J Singh, "On the tuning of electrical and thermal transport in thermoelectrics: an integrated theory–experiment perspective", *NPJ Comp. Mater.* **2016**, *2*, 15015.

[18] P.A. Kinzie, "Thermocouple temperature measurement", *Phys. Today* **1973**, *26* (11), 52.

[19] Y. Li, P. Qiu, H. Duan, J. Chen, G.J. Snyder, X. Shi, B. Brummerstedt Iversen, L. Chen, "Enhanced thermoelectric performance in rare earth-filled skutterudites", *J. Mater. Chem. C* **2016**, *4*, 4374-4379.

[20] A.U. Khan, K. Kobayashi, D.M. Tang, Y. Yamauchi, K. Hasegawa, M. Mitome, Y. Xue, B. Jiang, K. Tsuchiya, D. Golberg, Y. Bando, T. Mori, "Nano-micro porous skutterudites with 100% enhancement in ZT for high performance thermoelectricity", *Nano Energy* **2017**, *31*, 152-159.

[21] G. Rogl, P. Rogl, "Skutterudites, a most promising group of thermoelectric materials", *Curr. Opin. Green Sust. Chem.* **2017**, *4*, 50-57.

[22] M. Benyahia, V. Ohorodniichuk, E. Leroy, A. Dauscher, B. Lenoir, E. Alleno, "High thermoelectric figure of merit in mesostructured $In_{0.25}Co_4Sb_{12}$ n-type skutterudite", *J. Alloy Compd.* **2018**, *735*, 1096-1104.

[23] G. Rogl, P. Rogl, "How nanoparticles can change the figure of merit, ZT, and mechanical properties of skutterudites", *Mater. Today Phys.* **2017**, *3*, 48-69.

[24] L.D. Zhao, S.H. Lo, Y. Zhang, H. Sun, G. Tan, C. Uher, C. Wolverton, V.P. Dravid, M.G. Kanatzidis, "Ultralow thermal conductivity and high thermoelectric figure of merit in SnSe crystals", *Nature* **2014**, *508*, 373-377.

[25] C. Zhou, Y.K. Lee, Y. Yu, S. Byun, Z.Z. Luo, H. Lee, B. Ge, Y.L. Lee, X. Chen, J.Y. Lee, O. Cojocaru-Mirédin, H. Chang, J. Im, S.P. Cho, M. Wuttig, V.P. Dravid, M.G. Kanatzidis, "Polycrystalline SnSe with a thermoelectric figure of merit greater than the single crystal", *Nat. Mater.* **2021**, *20*, 1378-1384.

[26] G. Slack, *Thermoelectrics Handbook - Macro to Nano*, D. Rowe, Ed, Boca Raton, FL: Taylor and Francis, **2006**.

[27] I. Pallecchi, M. Pani, F. Ricci, S. Lemal, D. Bilc, P. Ghosez, C. Bernini, N. Ardoino, G. lamura, D. Marrè, "Thermoelectric properties of chemically substituted full-Heusler $Fe_2TiSn_{1-x}Sb_x$ (x=0, 0.1 and 0.2) compounds", *Phys. Rev. Mater.* **2018**, *2*, 075403.

[28] S. Chen, Z. Ren, "Recent progress of half-Heusler for moderate temperature thermoelectric applications", *Mater. Today*, **2013**, *16*, 387-395.

[29] A. Tavassoli, F. Failamani, A. Grytsiv, G. Rogl, P. Heinrich, H. Müller, E. Bauer, M. Zehetbauer, P. Rogl, "On the Half-Heusler compounds $Nb_{1-x}\{Ti,Zr,Hf\}_xFeSb$: Phase relations, thermoelectric properties at low and high temperature, and mechanical properties", *Acta Mater.* **2017**, *135*, 263-276.

[30] J. Fu, X. Su, Y. Yan, W. Liu, Z. Zhang, X. She, C. Uher, X. Tang, "Thermoelectric properties of Cu/Ag doped type-III $Ba_{24}Ge_{100}$ clathrates", *J. Solid State Chem.* **2017**, *253*, 414-420.

[31] J.A. Dolyniuk, B. Owens-Baird, J. Wang, J.V. Zaikina, K. Kovnir, "Clathrate thermoelectrics", *Mater. Sci. Eng. R* **2016**, *108*, 1-46.

[32] B. Sales, "Filled Skutterudites" in *Handbook on the Physics and Chemistry of Rare Earths*, vol. 33, North Holland, 1-34, **2003**.

[33] C. Huer, "Skuterudite-based thermoelectric" in *Thermoelectric Handbook - Macro to Nano*, Boca Raton, Taylor and Francis, **2006**.

[34] C. Artini, C. Fanciulli, G. Zanicchi, G.A. Costa, R. Carlini, "Thermal expansion and high temperature structural features of the filled skutterudite $Sm_\beta(Fe_\alpha Ni_{1-\alpha})_4Sb_{12}$", *Intermetallics* **2017**, *87*, 31-37.

[35] C. Uher, "Skutterudite-Based Thermoelectrics" in *Thermoelectrics Handbook – Macro to Nano*, 1st ed.; Rowe, D.M., Ed.; Taylor and Francis: Boca Raton, USA, **2005**.

[36] C. Uher, "In search of efficient n-type skutterudite thermoelectrics" in *Twenty-First International Conference on Thermoelectrics*, *Proceedings of the 21st Conference on Thermoelectrics*, Long Beach, USA, 29 Aug 2002, 35-41, **2002**.

[37] V. Keppens, D. Mandrus, B.C. Sales, B.C. Chakoumakos, P. Dai, R. Coldea, M.B. Maple, D.A. Gajewski, E.J. Freeman, S. Bennington, "Localized vibrational modes in metallic solids", *Nature* **1998**, *395*, 876-878.

[38] G.A. Slack, "New Materials and Performance Limits for Thermoelectric Cooling" in *CRC Handbook of Thermoelectrics,* 1st ed.; Rowe, D.M., Ed.; Taylor and Francis: Boca Raton, USA, 407-439, **1995**.

[39] G. Rogl, A. Grytsiv, P. Rogl, N. Peranio, E. Bauer, M. Zehetbauer, O. Eibl, "*n*-Type skutterudites $(R,Ba,Yb)_yCo_4Sb_{12}$ (R = Sr, La, Mm, DD, SrMm, SrDD) approaching ZT ≈ 2.0", *Acta Mater.* **2014**, *63*, 30-43.

[40] G. Rogl, O. Renk, S. Ghosh, R.C. Mallik, A. Grytsiv, J. Bursik, E. Schafler, F. Tuomisto, E. Bauer, P. Rogl, "Properties of HPT-Processed Large Bulks of *p*-Type Skutterudite $DD_{0.7}Fe_3CoSb_{12}$ with ZT > 1.3", *ACS Appl. Energy Mater.* **2021**, *4*, 4831-4844.

[41] C. Artini, R. Carlini, R. Spotorno, F. Failamani, T. Mori, P. Mele, "Structural properties and thermoelectric performance of the double filled skutterudite $(Sm,Gd)_y(Fe_xNi_{1-x})_4Sb_{12}$", *Materials* **2019**, *12*, 2451.

[42] C. Artini, G. Zanicchi, G.A. Costa, M.M. Carnasciali, C. Fanciulli, R. Carlini, "Correlations between structural and electronic properties in the filled skutterudite $Sm_y(Fe_xNi_{1-x})_4Sb_{12}$", *Inorg. Chem.* **2016,** *55,* 2574-2583.

[43] G. Rogl, A. Grytsiv, P. Heinrich, E. Bauer, P. Kumar, N. Peranio, O. Eibl, J. Horky, M. Zehetbauer, P. Rogl, "New bulk *p*-type skutterudites $DD_{0.7}Fe_{2.7}Co_{1.3}Sb_{12-x}X_x$ (X = Ge, Sn) reaching ZT > 1.3", *Acta Mater.* **2015**, *91*, 227-238.

[44] G. Rogl, A. Grytsiv, E. Bauer, P. Rogl, M. Zehetbauer, "Thermoelectric properties of novel skutterudites with didymium: $DD_y(Fe_{1-x}Co_x)_4Sb_{12}$ and $DD_y(Fe_{1-x}Ni_x)_4Sb_{12}$", *Intermetallics* **2010**, *18*, 57-64.

[45] C. Artini, R. Carlini, L. Gigli, C. Fanciulli, "Compositional optimization and structural properties of the filled skutterudite $Sm_y(Fe_xNi_{1-x})_4Sb_{11.5}Sn_{0.5}$", *Metals* **2020**, *10*, 692.

[46] N. Shaheen, M. Sufyan Javed, H. Ullah Shah, S. Hussain, M. Ashfaq Ahmad, R. Raza, M. Saleem, X. Zhou, "Enhanced thermoelectric properties in Ge-doped and single-filled skutterudites prepared by unique melt-spinning method", *Cer. Int.* **2018**, *44*, 12610-12614.

[47] G.X. Liang, Z.H. Zheng, F. Li, J.T. Luo, H. Jin, X.H. Zhang, P. Fan, "Nano structure Ti-doped skutterudite $CoSb_3$ thin films through layer inter-diffusion for enhanced thermoelectric properties", *J. Eur. Cer. Soc.* **2019**, *39*, 4842-4849.

[48] G. Fu, L. Zuo, J. Chen, M. Lu, L. Yu, "Thermoelectric properties of DC-sputtered filled skutterudite thin film", *J. Appl. Phys.* **2015**, *117*, 125304.

[49] M.V. Daniel, M. Lindorf, M. Albrecht, "Thermoelectric properties of skutterudite $CoSb_3$ thin films", *J. Appl. Phys.* **2016**, *120*, 125306.

[50] Z.H. Zheng, F. Li, J.T. Luo, G.X. Liang, H.L. Ma, X.H. Zhang, P. Fan, "Thermoelectric properties and micro-structure characteristics of nano-sized $CoSb_3$ thin films prefabricating by co-sputtering", *J. Alloy Compd.* **2018**, *732*, 958-962.

[51] C. Bourgès, N. Sato, T. Baba, T. Baba, I. Ohkubo, N. Tsujii, T. Mori, "Drastic power factor improvement by Te doping of rare earth-free $CoSb_3$-skutterudite thin films", *RSC Adv.* **2020**, *10*, 21129-21135.

[52] D. Colceag, A. Dauscher, B. Lenoir, V. da Ros, R. Birjega, A. Moldovan, M. Dinescu, "Pulsed laser deposition of doped skutterudite thin films", *Appl. Surf. Sci.* **2007**, *253*, 8097-8101.

[53] M. Ohtaki, K. Araki, K. Yamamoto, "High Thermoelectric Performance of Dually Doped ZnO Ceramics", *J. Electron. Mater.* **2009**, *38*, 1234-1238.

[54] S. Saini, H. Yaddanapudi, K. Tian, Y. Yin, D. Magginetti, A. Tiwari, "Terbium Ion Doping in $Ca_3Co_4O_9$: A Step towards High-Performance Thermoelectric Materials", *Sci. Rep.* **2017,** *7,* 44621.

[55] P. Mele, T. Endo, S. Arisawa, C. Li, T. Tsuchiya, *Oxide Thin Films, Multilayers, and Nanocomposites*, Springer, **2015**.

[56] P. Mele, S. Saini, H. Honda, K. Matsumoto, K. Miyazaki, H. Hagino, A. Ichinose, "Effect of substrate on thermoelectric properties of Al-doped ZnO thin films", *Appl. Phys. Lett.* **2013**, *102*(25), 253903.

[57] P. Jood, R.J. Mehta, Y. Zhang, G. Peleckis, X. Wang, R. W. Siegel, T. Borca-Tasciuc, S.X. Dou, G. Ramanath, "Al-doped zinc oxide nanocomposites with enhanced thermoelectric properties", *Nano Lett.* **2011**, *11*(10), 4337-42.

[58] S. Han, "Wearable Thermoelectric Devices" in Mele P. et al. (eds) *Thermoelectric Thin Films.* Springer, Cham, **2019**.

[59] M.F. Silva, J.F. Ribeiro, J.P. Carmo, L.M. Gonçalves, J.H.Correia, "Thin Films for Thermoelectric Applications" in Bhushan B. (eds) *Scanning Probe Microscopy in Nanoscience and Nanotechnology* 3. NanoScience and Technology. Springer, Berlin, Heidelberg, **2012**.

[60] Y. Yu, W. Zhu, X. Kong, X., Y. Wang, P. Zhou, Y. Deng, "Recent development and application of thin-film thermoelectric cooler", *Front. Chem. Sci. Eng.* **2020**, *14*, 492-503.

[61] X. Chen, Z. Zhou, Y.H. Lin, C. Nan, "Thermoelectric thin films: Promising strategies and related mechanism on boosting energy conversion performance", *J. Materiomics* **2020**, *6*(3), 494-512.

[62] T.J. Seebeck, "Magnetische Polarisation der Metalle und Erze Durch Temperatur-Differenz" 1822-23 in Ostwald's *Klassiker der Exakten Wissenshaften* Nr. 70, **1895**.

[63] M.H. Elsheik, D.A. Shnawa , M.F. Mohd Sabri, S.B. Mohd Said, M.H. Hassan, M. Ali Bashir, M. Mohamed, "A review on thermoelectric renewable energy: Principle parameters" *Renew. Sust. Energ. Rev.* **2014***, 30*, 337-355.

[64] G.D. Mahan, "Thermoelectric Effect", *Encyclopaedia of Condensed Matter Physics*, **2005**, 180-187.

[65] G. Min, "Thermoelectric Module Design Theories" in *Thermoelectrics Handbook: Macro to Nano*, 1-3, **2006**.

[66] N.M. Ravindra, B. Jariwala, A. Bañobre, A. Maske, "Thermoelectric parameters and their optimization - Chapter 2" in *Thermoelectrics*, Springer, 7-20, **2019**.

[67] S. Ceresara, "Materiali nanostrutturati per applicazioni termoelettriche", *La Metall. Ital.* **2003***, 2*, 49-53.

[68] Q.E. Hussain, D. Brigham, C. Maranville, "Thermoelectric exhaust heat recovery for hybrid vehicles", *SAE Int. J. Engines* **2009**, *2*, pp. 1132-114.

[69] C. Vineis, A. Shakouri, A. Majumdar, M. Kanatzidis, "Nanostructured Thermoelectrics: Big Efficiency Gains for Small Features", *Adv. Mater.* **2010**, 22, 3970-3980.

[70] M. Ohtaki, "Nanostructured Oxide thermoelectric Materials with Enhanced Phonon Scattering", Chapter 8 in *Oxide Thin Films, Multilayers and Nanocomposites*, Springer Books, **2015**.

[71] J.H. Goldsmid, *Introduction to thermoelectricity*, Berlin, Springer Series in Materials Science, 197-198, **2006**.

[72] J.R. Sootsman, D.Y. Chung, M.G. Kanatzidis, "New and Old Concepts in Thermoelectric Materials", *Angew. Chem.* **2009**, *48*, 8616-8639.

[73] E. Macìa-Barber, "Fundamental Aspects" in *Thermoelectric Materials: Advances and Applications*, Boca Ratòn, Florida, CRC Press, Taylor and Francis Group, **2015**.

[74] X.L. Shi, J. Zou, Z.G. Chen, "Advanced Thermoelectric Design: From Materials and Structures to Devices", *Chem. Rev.* **2020**, *120* (15), 7399-7515.

[75] C. Zhang, M. de la Mata, Z. Li, F.J. Belarre, J. Arbiol, K.A. Khor, D. Poletti, B. Zhu, Q. Yan, Q. Xiong, "Enhanced thermoelectric performance of solution-derived bismuth telluride based nanocomposites via liquid-phase Sintering", *Nano Energy* **2016**, *30*, 630-638,

[76] M. Li, D.L. Cortie, J. Liu, D. Yu, S.M.K.N. Islam, L. Zhao, D.R. Mitchell, R.A. Mole, M.B. Cortie, S. Dou, X. Wang, "Ultra-High Thermoelectric Performance in Graphene Incorporated Cu_2Se: Role of Mismatching Phonon Modes", *Nano Energy* **2018**, *53*, 993-1002.

[77] X. Xu, L. Xie, Q. Lou, D. Wu, J. He, "Boosting the Thermoelectric Performance of Pseudo-Layered $Sb_2Te_3(GeTe)_n$ via Vacancy Engineering", *Adv. Sci.* **2018**, *5*, 1801514.

[78] Z. Zhou, J. Li, Y. Fan, Q. Zhang, X. Lu, S. Fan, K. Kikuchi, N. Nomura, A. Kawasaki, L. Wang, W. Jiang, "Uniform Dispersion of SiC in Yb-Filled Skutterudite Nanocomposites with High Thermoelectric and Mechanical Performance", *Scr. Mater.* **2019**, *162*, 166-171.

[79] G. Rogl, A. Grytsiv, K. Yubuta, S. Puchegger, E. Bauer, C. Raju, R. Mallik, P. Rogl, "In-Doped Multifilled *n*-Type Skutterudites with ZT = 1.8", *Acta Mater.* **2015**, *95*, 201-211.

[80] P. Jood, R.J. Mehta, Y. Zhang, G. Peleckis, X. Wang, R.W. Siegel, T. Borca-Tasciuc, S.X. Dou, G. Ramanath,

"Al-Doped Zinc Oxide Nanocomposites with Enhanced Thermoelectric Properties", *Nano Lett.* *2011*, *11*, 4337–4342.

[81] R. Carlini, M.M. Carnasciali, F. Soggia, Y. Shen, G. Zanicchi, "ICP-AES and microRaman corrosion behaviour investigation on Pb, Sb, Bi tellurides in sodium chloride solution", *J. Alloys Compd.* **2016**, *654*, 593-598.

[82] W. He, G. Zhang, X. Zhang, J. Ji, G. Li , X. Zhao, "Recent development and application of thermoelectric generator and cooler", *Appl. Energy* **2001**, *143*, 1-25.

[83] R. Venkatasubramanian, E. Siivola, T. Colpritts, "Thin-film thermoelectric devices with high room-temperature figures of merit", *Nature* **2001**, *413*, 597–602.

[84] Y. Hosokawa, K. Tomita, M. Takashiri, "Growth of single-crystalline Bi_2Te_3 hexagonal nanoplates with and without single nanopores during temperature-controlled solvothermal synthesis", *Sci. Rep.* **2019**, *9*, 10790.

[85] A. Sharan, Z. Gui, A. Janotti, "Formation of two-dimensional electron and hole gases at the interface of half-Heusler semiconductors", *Phys. Rev. Mater.* **2019**, *3*(6), 061602-061608.

[86] S.C. Sevov in *Intermetallic Compounds – Principles and Practice: Progress*, Volume 3, Ed. Westbrook, J.H. & Freisher, R.L., 113-132, John Wiley & Sons. Ltd., **2002**.

[87] A. Castellero, C. Fanciulli, R. Carlini, G. Fiore, P. Mele, F. Passaretti, M. Baricco, "Effect of processing routes on the synthesis and properties of Zn_4Sb_3 thermoelectric alloy", *J. Alloys Compd.* **2015**, *653*, 54-60.

[88] A. Denoix, A. Solaiappan, R. Ayral, F. Rouessac, J. Tedenac, "Chemical route for formation of intermetallic Zn_4Sb_3 phase", *J. Solid State Chem.* **2010**, *183*, 1090-1094.

[89] T. Takabatake, K. Suekuni, T. Nakayama, E. Kaneshita, "Phonon-glass electron-crystal thermoelectric clathrates: Experiments and theory", *Rev. Mod. Phys.* **2014**, *86*, 669.

[90] P. Rogl, *Thermoelectrics Handbook Macro to Nano*, Boca Raton, FL: D. M. Rowe, Ch. 32, **2006**.

[91] G.S. Nolas, J. Poon, M. Kanatzidis, "Recent Developments in Bulk Thermoelectric Materials", *MRS Bulletin* **2006**, *31*, 199-205.

[92] Z. Tian, S. Lee, G. Chen , "Comprehensive review on heat transport in thermoelectric materials and devices", *Annual reviews on heat transfer in Thermoelectric Materials and Devices* **2014**, *17*, 425-466.

[93] G. Svensson, A. Palmqvist, A. Saramat, "Large thermoelectric figure of merit at high temperature in Czochralski-grown clathrate $Ba_8Ga_{16}Ge_{30}$", *J. Appl. Phys.* **2006**, *99*(023708), 1-5.

[94] M.C. Schafer, S. Bobev, "New Type-I and Type-II Clathrates in the Systems Cs–Na–Ga–Si, Rb–Na–Ga–Si, and Rb–Na–Zn–Si", *Inorganics* **2014**, *2*(1), 79-95.

[95] Y. Yu, B. Duan, G. Bai, J. Li, L. E, F. Li, G. Chen, P. Zhai, "Rapid preparations and thermoelectric properties of bulk skutterudites with in situ nanostructures", *AIP Advances* **2018**, *8*, 085201.

[96] X. Shi, H. Kong, C.-P. Li, C. Uher, J. Yang, J. R. Salvador, H. Wang, L. Chen, W. Zhang, "Low thermal conductivity and high thermoelectric figure of merit in n-type $Ba_xYb_yCo_4Sb_{12}$ double-filled skutterudites", *Appl. Phys. Lett.* **2008**, *92*, 182101.

[97] X. Y. Zhao, X. Shi, L. D. Chen, W. Q. Zhang, S. Q. Bai, Y. Z. Pei, and X. Y. Li, "Synthesis of $Yb_yCo_4Sb_{12}/Yb_2O_3$ composites and their thermoelectric properties", *Appl. Phys. Lett.* **2006**, *89*, 092121.

[98] B.J. Jeon, D.K. Shin, I.H. Kim, "Synthesis and Thermoelectric Properties of $Ce_{1-z}Yb_zFe_{4-x}Ni_xSb_{12}$ Skutterudites", *J. Electron. Mater.* **2015**, *44*(6), 1388-1393.

[99] G. Tan, S. Wang, Y. Yan, H. Li, X. Tang, "Enhanced thermoelectric performance in p-type $Ca_{0.5}Ce_{0.5}Fe_{4-x}Ni_xSb_{12}$ skutterudites by adjusting the carrier concentration", *J. Alloys Compd.* **2012**, *513*, 328-333.

[100] B.J. Jeon, D.K. Shin, I.H. Kim, "Synthesis and Thermoelectric Properties of $La_{1-z}Yb_zFe_{4-x}Ni_xSb_{12}$ Skutterudites", *J. Electron. Mater.* **2016**, *5*(3), 1907-1913.

[101] M. Martin-Gonzalez, "Past and present of metal chalcogenides, oxides, Heusler compounds and Zintl phases as thermoelectrics: A brief summary", *Proceedings of the International School of Physics "Enrico Fermi", Course 207 "Advances in Thermoelectricity: Foundational Issues, Materials and Nanotechnology"*, edited by D. Narducci, G.J. Snyder, C. Fanciulli, IOS, Amsterdam, SIF, Bologna, **2021**.

[102] J. D. Baran, M. Molinari, N. Kulwongwit, F. Azough, R. Freer, D. Kepaptsoglou, Q. M. Ramasse, S. C. Parker, "Tuning Thermoelectric Properties of Misfit Layered Cobaltites by Chemically Induced Strain", *J. Phys. Chem. C* **2015**, *119*(38), 21818-21827.

[103] Y. Huang, B. Zhao, S. Lin, Y. Sun, "Enhanced Thermoelectric Performance Induced by Misplaced Substitution in Layered $Ca_3Co_4O_9$", *J. Phys. Chem. C* **2015**, *119*(15), 7979-7986.

[104] L.D. Zhao, J. He, D. Berardan, Y. Lin, J.F. Li, C.W. Nanc, N. Dragoe, "BiCuSeO oxyselenides: new promising thermoelectric materials", *Energy Environ. Sci.* **2014**, *7*, 2900-2924.

[105] Y.L. Pei, J. He, J.F. Li, F. Li, Q. Liu, W. Pan, C. Barreteau, D. Berardan, N. Dragoe, L.D. Zhao, "High thermoelectric performance of oxyselenides: intrinsically low thermal conductivity of Ca-doped BiCuSeO" *NPG Asia Mater.* **2013**, 5(e47).

[106] H. Ohta, K. Sugiura, K. Koumoto, "Recent Progress in Oxide Thermoelectric Materials: *p*-Type $Ca_3Co_4O_9$ and *n*-Type $SrTiO_3^-$", *Inorg. Chem.* **2008**, *47*(19), 8429-8436.

[107] I. Pallecchi, M.T. Buscaglia, V. Buscaglia, E. Gilioli, G. Lamura, F. Telesio, M.R. Cimberle, D. Marré, "Thermoelectric behavior of Ruddlesden–Popper series iridates", *J. Phys.: Condens. Matter* **2016**, *28*, 065601.

[108] R.R. Sun, L.N. Liu, G.L. Guo, J. Zhang, Y.S. Zhang, C.J. Tang, J.F. Su, D.M. Zhang, X.Y. An, "Fabrication and Thermoelectric Properties of *n*-Type Ruddlesden-Popper Phase $Sr_3(Ti_{1-x}Ta_x)_2O_7$ Oxides", *ECS J. Solid State Sci. Technol.* **2016**, *5*, P151.

[109] ZnO structure. Available Online:
https://en.wikipedia.org/wiki/Zinc_oxide#/media/File:Wurtzite_polyhedra.png

[110] T. Tsubota, M. Ohtaki, K. Eguchi, H. Arai, "Thermoelectric properties of Al-doped ZnO as a promising oxide material for high-temperature thermoelectric conversion", *J. Mater. Chem.* **1997**, *7*, 85-90.

[111] H. Ohta, "Thermoelectrics based on strontium titanate", *Materials Today* **2007**, *10*(10), 44-49.

[112] S.R. Sarath Kumar, A. Alyamani, J.W. Graff, T.M. Tritt, H.N. Alshareef, "Pulsed laser deposition and thermoelectric properties of In- and Yb-doped $CoSb_3$ skutterudite thin films", *J. Mater. Res.* **2011**, *26*(15), 1836-1841.

[113] I. Petsagkourakis, K. Tybrandt, X. Crispin, I. Ohkubo, N. Satoh, T. Mori, "Thermoelectric materials and applications for energy harvesting power generation", *Sci. Technol. Adv. Mater.* **2018**, *19*(1), 836-862.

[114] M. Haras, T. Skotnicki, "Thermoelectricity for IoT – A review", *Nano Energy* **2018**, *54*, 461-476.

[115] A. Tarancon, "Powering the IoT revolution with heat", *Nat. Electron.* **2019**, *2*, 270-271.

[116] N. Nandihalli C.J. Liu, T. Mori, "Polymer based thermoelectric nanocomposite materials and devices: Fabrication and characteristics", *Nano Energy* **2020**, *78*, 105186.

[117] D. Narducci, B. Lorenzi, "Challenges and Perspectives in Tandem Thermoelectric–Photovoltaic Solar Energy Conversion", *IEEE Trans. Nanotechnol.* **2016**, *15*(3), 348-355.

[118] J. Yan, X. Liao, D. Yan, Y. Chen, "Review of Micro Thermoelectric Generator", *J. Microelectromech. Syst.* **2018**, *27*(1), 1-18.

[119] J.J. Feng, W. Zhu, Y. Deng , "An overview of thermoelectric films: Fabrication techniques, classifications, and regulation methods", *Chin. Phys. B* **2018**, *27*(4), 047210-1 - 047210-15.

[120] J.M. Gilbert, F. Balouch, "Comparison of Energy Harvesting Systems for Wireless Sensors Networks", *Int. J. Autom. Comput.* **2018**, *5*(4), 334-347.

[121] Z. G. Wan, Y. K. Tan, C. Yuen, "Review on energy harvesting and energy management for sustainable wireless sensor networks", in *Proceeding IEEE 13th International Conference on Communication Technologies* **2011**, JiNan.

[122] A. Suzuki, H. A. Durand, I. Kataoka, in *Proceedings of the XIX International Conference on Thermoelectrics,* Cardiff, D.M. Rowe (Ed.), Babrow Press, Wales, UK, 263, **2000**.

[123] A. Dauscher, M. Puyet, B. Lenoir, D. Colceag, D. Linescu, "Microstructural investigation of $Ca_xCo_4Sb_{12}$ films prepared by pulsed laser deposition", *Appl. Phys. A* **2004**, *79*, 1465-1468.

[124] R.E. Baumbach, W.M. Yuhasz, M.B. Maple, "Pulsed laser deposition of $PrFe_4Sb_{12}$ thin films", *Appl. Phys. A* **2006**, *84*, 227-229.

[125] J.W. Fergus, "Oxide materials for high temperature thermoelectric energy conversion", *J. Eur. Ceram. Soc.* **2012**, *32*(3), 525-540.

[126] S. Saini, P. Mele, H. Honda, D.J. Henry, P.E. Hopkins, L. Molina-Luna, K. Matsumoto, K. Miyazaki, A. Ichinose, "Enhanced thermoelectric performance of Al-doped ZnO thin films on amorphous substrate", *Jpn. J. Appl. Phys.* **2014**, *53*, 060306.

[127] T. Tynell, A. Giri, J. Gaskins, P.E. Hopkins, P. Mele, K. Miyazaki, M. Karppinen, "Efficiently suppressed thermal conductivity in ZnO thin films via periodic introduction of organic layers", *J. Mater. Chem. A* **2014**, *2*, 12150.

[128] A.M. Darwish, A. Muhammad, S.S. Sarkisov, P. Mele, S. Saini, J. Liu, J. Shiomi, "Thermoelectric properties of Al-doped ZnO composite films with polymer nanoparticles prepared by pulsed laser deposition", *Compos. B. Eng.* **2019**, *167*, 406-4106.

[129] S. Saini, P. Mele, T. Oyake, J. Shiomi, J.P. Niemelä, M. Karppinen, K. Miyazaki, C. Li, T. Kawaharamura, A. Ichinose, L. Molina-Luna, "Porosity-tuned thermal conductivity in thermoelectric Al-doped ZnO thin films grown by mist-chemical vapor deposition", *Thin Solid Films* **2019**, *685*,180-185.

[130] P. Mele, S. Saini, T. Mori, Y. Kakefuda, M. I. Adam, S.J. Singh, *work in preparation.*

[131] S. Saini, P. Mele, H. Honda, K. Matsumoto, K. Miyazaki, L. Molina Luna, P.E. Hopkins, "Influence of Postdeposition Cooling Atmosphere on Thermoelectric Properties of 2% Al-Doped ZnO Thin Films Grown by Pulsed Laser Deposition", *J. Electron. Mater.* **2015**, *44*, 1547-1553.

[132] J. Loureiro, N. Neves, R. Barros, T. Mateus, R. Santos, S. Filonovich, S. Reparaz, C.M. Sotomayor-Torres, F. Wyczik, L. Divay, R. Martins, I. Ferreira, "Transparent aluminium zinc oxide thin films with enhanced thermoelectric properties", *J. Mater. Chem. A* **2014**, *2*, 6649.

[133] S. Liu, M. Lan, G. Li, Y. Piao, H. Ahmoum, Q. Wang, "Breaking the tradeoff among thermoelectric parameters by multicomposite of porosity and CNT in AZO films", *Energy* **2021**, *225*, 120320.

[134] Y. Hirose, M. Tsuchii, K. Shigematsu, K. Kakefuda, T. Mori, T. Hasegawa, "Thermoelectric properties of amorphous ZnO_xN_y thin films at room temperature", *Appl. Phys. Lett.* **2019**, *114*, 193903.

[135] N.H.T. Nguyen, T.H. Nguyen, Y.R. Liu, M. Aminzare, A.T.T. Pham, S. Cho, D.P. Wong, K.H. Chen, T. Seetawan, N.K. Pham, H.K.T. Ta, V.C. Tran, T.B. Phan, "Thermoelectric Properties of Indium and Gallium Dually Doped ZnO Thin Films", *ACS Appl. Mater. Interfaces* **2016**, *8*, 33916.

[136] J.W. Sharp, "Thermoelectric and Energy Conversion Device", *Reference Module in Materials Science and Materials Engineering*, **2016**.

[137] C. Uher, "Skutterudites: Prospective novel thermoelectrics", *Semicond. Semimet.* **2001**, *69*, 139-253.

[138] C. Artini, N. Parodi , G. Latronico, R. Carlini, "Formation and Decomposition Process of the Filled Skutterudite $Sm_y(Fe_xNi_{1-x})_4Sb_{12}$ (0.40<x>1) as Revealed by Differential Thermal Analysis", *J. Mater. Eng. Perform.* **2018**, *27*(12), 6259-6265.

[139] K. Ritcher, H. Ipser, "An experimental Investigation of the Fe-Ni-Sb Ternary Phase Diagram", *J. Phase Equilibria* **1997**, *18*(3), 235-244.

[140] V. Raghavan, "Fe-Ni-Sb (Iron-Nickel-Antimony)", *J. Phase Equilibria Diffus.* **2004**, *25*(6), 89 – 91.

[141] G. Latronico, F. Valenza, R. Carlini, P. Mele, C. Artini, "Interfacial Reactivity of the Filled Skutterudite $Sm_y(Fe_xNi_{1-x})_4Sb_{12}$ in Contact with Liquid In-Based Alloys and Sn", *Metals* **2020**, *10*, 364.

[142] C. Artini, A. Cingolani, F. Valenza, U. Anselmi-Tamburini, G. Latronico, P. Mele, "Effect of the sintering pressure on structure and microstructure of the filled skutterudite $Sm_y(Fe_xNi_{1-x})_4Sb_{12}$ ($x = 0.50–0.80$, $y = 0.17–0.55$)", *Mater. Res. Bull.* **2021**, *139*, 111261.

[143] C. Artini, G. Latronico, R. Carlini, S. Saini, T. Takeuchi, S. Choi, A. Baldini, U. Anselmi-Tamburini, F. Valenza, P. Mele, "Effect of different processing routes on the power factor of the filled skutterudite $Sm_y(Fe_xNi_{1-x})_4Sb_{12}$ (x = 0.50-0.80; y = 0.12-0.53)", *ES Mater. Manuf.* **2019**, *29*, 29-37.

[144] A. Phuangyod, J. Hayashi, Y. Kawamura, C. Artini, G. Latronico, R. Carlini, S. Saini, P. Mele, C. Sekine, "Low-Temperature thermoelectric properties of p-Type and n-Type filled skutterudite compounds $Sm_y(Fe_{1-x}Ni_x)_4Sb_{12}$ prepared under high pressure", *Jpn. J. Appl. Phys.*, **2020**, *59*, 061004.

[145] R. Spotorno, G. Ghiara, G. Latronico, R. Carlini, P. Mele, C. Artini, "Corrosion of the Filled Skutterudite $Sm_{0.1}(Fe_{0.45}Ni_{0.55})_4Sb_{12}$ by NaCl Solutions: An Electrochemical Study", *J. Electron. Mater.* **2020**, *49*, 1-9.

[146] B.C. Sales, D. Mandrus, R. Williams, "Filled Skutterudite Antimonides: A new class of thermoelectric Materials", *Science* **1996**, *272*, 1325-1328.

[147] B.C. Sales, D. Mandrus, B.C. Chakoumakos, V. Keppens, J.R. Thompson, "Filled Skutterudites Antimonides: Electron crystals and phonon glasses", *Phys. Rev. B* **1997**, 56(23), 15081-15089.

[148] R. Weast, *Handbook of Chemistry and Physics*, Cleveland: CRC Press, **1976**.

[149] M.J. Kruzewski, L. Ciupinski, R. Zybala, "Review of rapid fabrication methods of skutterudite materials", *Mater. Today: Proc.* **2021**, *44*(4), 3475-3482.

[150] W. Liu, B. P. Zhang, J. F. Li, L. D. Zhao, "Enhanced thermoelectric properties in $CoSb_{3-x}Te_x$ alloys prepared by mechanical alloying and Spark Plasma Sintering", *J. Appl. Phys.* **2007**, *102*(10), 103717-103721.

[151] S. Bao, J. Yang, W. Zhu, X. Fan , X. Duan, J. Peng, "Preparation and thermoelectric properties of La filled skutterudites by mechanical alloyng and hot pressing", *Mater. Lett.* **2006**, *60*(16), 2029-2032.

[152] F. Chen, R. Liu, Z. Yao, Y. Xing, S. Bai, L. Chen, "Scanning laser melting for rapid and massive fabrication of filled skutterudites with high thermoelectric performance", *J. Mater. Chem. A* **2018**, *6*(16), 6772-6779.

[153] "Sintesi Di Materiali Inorganici Solidi" [Online]. Available: http://www.chimdocet.it/solido/file12a.htm.

[154] K. Inoue, "Electric-Discharge Sintering", *Japan Patent* US3241956A, 30 May **1963**.

[155] K. Inoue, "Method of electrically sintering discrete bodies", *Japan Patent* US3340052A, 05 September **1967**.

[156] M. Suarez, A. Fernandez, R. Torrecillas, J. Menendez, "Sintering to Transparency of Polycrystalline Ceramic Materials" in *Sintering of Ceramics - New Emerging Techniques*, A. Lakshmanan, Ed Rijeka, Croatia: InTech, 541, **2012**.

[157] S. Ceresara, C. Fanciulli , F. Passaretti, D. Vasilevskiy, "Texturing of $(Bi_{0.2}Sb_{0.8})_2Te_3$ Nanopowders by Open Die Pressing", *J. Electron. Mater.* **2013**, *42*(7), 1529-1534.

[158] R. Carlini, C. Fanciulli, A. Castellero, F. Passaretti, M. Baricco, G. Zanicchi, "Phase selection and microstructure refinement of melt-spun Zn_4Sb_3-type compound", *Proceedings of the 11th European Conference on Thermoelectrics*, Noordwijk, **2014**.

[159] J.J. Feng, W. Zhu, Y. Deng , "An overview of thermoelectric films: Fabrication techniques, classifications, and regulation methods", *Chin. Phys. B*, **2018**, *27*(4), 047210-1 - 047210-15.

[160] J. E. Crowell, "Chemical methods of thin film depositions: Chemical vapor deposition, atomic layer deposition, and related technologies", *J. Vac. Sci. Technol. A* **2003**, *21*(5), S88 - S96.

[161] A. Knoll, "Thin Film Physical Vapor Deposition (PVD) System", University of Akron, [Online]. Available: https://www.uakron.edu/soa/instruments/pvd/.

[162] P. Schaaf, *Laser Processing of Materials*, vol. 139, Springer, 89-94, **2010**.

[163] https://en.wikipedia.org/wiki/List_of_laser_types#/media/File:Commercial_laser_lines.svg

[164] J. Majumdar, I. Manna, "Laser processing of materials", *Sadhana* **2003**, *28*, 495-562.

[165] Toptica Photonics, "Frequency Conversion" [Online]. Available: https://www.toptica.com/technology/technical-tutorials/frequency-conversion/.

[166] L. Wang, N. Zhai, L. Liu, X. Wang, G. Wang, Y. Zhu, C. Chen, "High-average-power 266 nm generation with a $KBe_2BO_3F_2$ prism-coupled device", *Opt. Express* **2014**, *22*(22), 27086-27093.

[167] Nd:YAG LASER SYSTEM. User's Manual

[168] ThorLabs, Pockels cell, [Online]. Available: https://www.thorlabs.com/newgrouppage9.cfm?objectgroup_ID=6149

[169] N. Kaiser, "Review of the fundamentals of thin-film growth", *Appl. Opt.* **2002**, *41*(16), 3053-3060.

[170] M. Ohring, *Materials Science of Thin Films - Deposition and Structure*, Second Edition, by Academic Press, **2002**.

[171] R. Eason, *Pulsed Laser Deposition of Thin Films*, Wiley Interscience, by John Wiley & Sons, **2007**.

[172] M.A. Gharavi, "Theoretical and Experimental Studies on Early Transition Metal Nitrides for Thermoelectrics", *Doctoral Dissertation*, n° 2031, from Linkoping University, **2019**.

[173] P. Jiang, X. Qian, R. Yang , "Tutorial: Time-domain thermoreflectance (TDTR) for thermal property characterization of bulk and thin film materials", *J. Appl. Phys.* **2018**, *124*, 161103.

[174] Takahiro Baba, Tetsuya Baba, Kazuko Ishikawa, and Takao Mori , "Determination of thermal diffusivity of thin films by applying Fourier expansion analysis to thermo-reflectance signal after periodic pulse heating", *J. Appl. Phys.* **2021**, *130*, 225107.

[175] G. Latronico, S. Singh, P. Mele, A. Darwish, S. Sarkisov, S.W. Pan, Y. Kawamura, C. Sekine, T. Baba, T. Mori, T. Takeuchi, A. Ichinose, S. Wilson, "Synthesis and Characterization of Al- and SnO_2-Doped ZnO Thermoelectric Thin Films", *Materials* **2021**, *14*, 6929.

[176] G. Latronico, P. Mele, C. Artini, P. Manfrinetti, S.W. Pan, Y. Kawamura, C. Sekine, S. Singh, T. Takeuchi, T. Baba, C. Bourgès, T. Mori, "Investigation on the power factor of skutterudite $Sm_y(Fe_xNi_{1-x})_4Sb_{12}$ thin films: Effects of deposition and annealing temperature", *Materials* **2021**, *14(19)*, 5773.

[177] R.C. Weast, *Handbook of Chemistry and Physics,* 56th ed.; CRC Press: Cleveland, USA, **1975**.

[178] Y. Kakefuda, K. Yubuta, T. Shishido, A. Yoshikawa, S. Okada, H. Ogino, N. Kawamoto, T. Baba, T. Mori, "Thermal conductivity of $PrRh_{4.8}B_2$, a layered boride compound", *APL Mater.* **2017**, *5*, 126103.

[179] M. Piotrowski, M. Franco, V. Sousa, J. Rodrigues, F.L. Deepak, Y. Kakefuda, T. Baba, N. Kawamoto, B. Owens-Baird, P. Alpuim, K. Kovnir, T. Mori, Y.V. Kolenko, "Probing of thermal transport in 50 nm Thick PbTe nanocrystal films by time-domain thermoreflectance", *J. Phys. Chem. C* **2018**, *122*, 27127-27134.

[180] R. Daou, F. Pawula, O. Lebedev, D. Berthebaud, S. Hebert, A. Maignan, Y. Kakefuda, T. Mori, "Anisotropic thermal transport in magnetic intercalates Fe_xTiS_2", *Phys. Rev. B*. **2019**, *99*, 085422.

[181] W. Gao, Z. Liu, T. Baba, Q. Guo, D.M. Tang, N. Kawamoto, E. Bauer, N. Tsujii, T. Mori, "Significant off-stoichiometry effect leading to the N-type conduction and ferromagnetic properties in titanium doped Fe_2Val thin films", *Acta Mater.* **2020**, *200*, 848–856.

[182] C. Artini, A. Castellero, M. Baricco, M.T. Buscaglia, R. Carlini, R. "Structure, microstructure and microhardness of rapidly solidified $Sm_y(Fe_xNi_{1-x})_4Sb_{12}$ (x = 0.45, 0.50, 0.70, 1) thermoelectric compounds", *Solid State Sci.* **2018**, *79*, 71-78.

[183] S. Mustoufa, S. Tsuyuguchi, T. Arashi, M. Nishida, T. Hino, "Formation of Droplets on Thin Film Surface in Pulsed Laser Deposition Using Metal Targets", *Q. J. Jpn. Weld. Soc.* **2003**, *21*(3), 338-343.

[184] R. Carlini, A.U. Khan, R. Ricciardi, T. Mori, G. Zanicchi, "Synthesis, characterization and thermoelectric properties of Sm filled $Fe_{4-x}Ni_xSb_{12}$", *J. Alloy Compd.* **2016**, *655*, 321-326.

[185] Z.H. Zheng, M. Wei, J.T. Luo, F. Li, G.X. Liang, Y. Liang, J. Hao, H.L. Ma, X.H. Zhang, P. Fan, "An enhanced power factor via multilayer growth of Ag-doped skutterudite $CoSb_3$ thin films", *Inorg. Chem. Front.* **2018**, *5*, 1409-1414.

[186] P. Mele, K. Matsumoto, T. Horide, O. Miura, A. Ichinose, M. Mukaida, Y. Yoshida, S. Horii, "Tuning of the critical current in $YBa_2Cu_3O_{7-x}$ thin films by controlling the size and density of Y_2O_3 nanoislands on annealed $SrTiO_3$ substrates", *Supercond. Sci. Technol.* **2006**, *19*, 44-50.

[187] G.J.H.M. Rijnders, G. Koster, D.H.A. Blank, H. Rogalla,"In-situ growth monitoring during PLD of oxides using RHEED at high oxygen pressure", *Mater. Sci. Eng. B* **1998**, *56*(2–3), 223-227.

[188] WinPlotR, [Online], Available: https://cdifx.univ-rennes1.fr/winplotr/winplotr.html

[189] S. Saini, P. Mele, K. Miyazaki, A. Tiwari, "On-chip thermoelectric module comprised of oxide thin film legs", *Energy Convers. Manag.* **2016**, *114*, 251-257.

[190] J. García-Cañadas, "Thermoelectric Modules: Power Output, Efficiency, and Characterization", Chapter 7 in *Thermoelectric Energy Conversion: Basic Concepts and Device Applications* (First Edition)Wiley‐VCH Verlag GmbH & Co. KGaA, **2017**.

[191] M. Novotny, J. Cızek, R. Kuzel, J. Bulır J. Lancok, J. Connolly, E. McCarthy, S. Krishnamurthy, J.P. Mosnier, JW. Anwand, G. Brauer, "Structural characterization of ZnO thin films grown on various substrates by pulsed laser deposition", *J. Phys. D: Appl. Phys.* **2012**, *45*, 225101.

[192] M.K. Yaakob, N.H. Hussin, M.F.M. Taib, T.I.T. Kudin, O.H. Hassan, A.M.M. Ali, M.Z.A. Yahya, "First Principles LDA+U Calculations for ZnO Materials", *Integr. Ferroel.* **2014**, *155*, 15.

[193] T. Baba, "Analysis of One-dimensional Heat Diffusion after Light Pulse Heating by the Response Function Method". *Jpn. J. Appl. Phys.* **2009**, *48*(5S2), 05EB04.

[194] P. Mele, H. Kamei, H. Yasumune, K. Matsumoto, K. Miyazaki, "Development of Thermoelectric Module Based on Dense $Ca_3Co_4O_9$ and $Zn_{0.98}Al_{0.02}O$ Legs", *Met. Mater. Int.*, **2014**, *20*, 389.

[195] G.S. Nolas, H.J. Goldsmid, *Thermal Conductivity: Theory, Properties and Applications*, Kluwer Academic/Plenum, New York, **2004**, p. 114.

[196] L. Zhu, M. Hong, G.W. Ho, "Hierarchical Assembly of SnO_2/ZnO Nanostructures for Enhanced Photocatalytic Performance", *Sci. Rep.* **2015**, *5*, 11609.

[197] Z. Lu, Q. Zhou, C. Wang, Z. Wei, L. Xu, Y. Gui, "Electrospun ZnO-SnO_2 Composite Nanofibers and Enhanced Sensing Properties to SF_6 Decomposition Byproduct H_2S", *Front. Chem.* **2018**, *6*, 540.

[198] H. Kawazoe, M. Yasukawa, H. Hyodo, M. Kurita, H. Yanagi, H. Hosono, "*p*-type electrical conduction in transparent thin films of $CuAlO_2$", *Nature* **1997**, *389*, 939-942.

[199] H. Kawazoe, H. Yanagi, K. Ueda, H. Hosono, "Transparent *p*-Type Conducting Oxides: Design and Fabrication of *p-n* Heterojunctions", *MRS Bull.* **2000**, *25*, 28-36.

[200] Y. Feng, X. Jiang, E. Ghafari, B. Kucukgok, C. Zhang, I. Ferguson, N. Lu, "Metal oxides for thermoelectric power generation and beyond", *Adv. Compos. Hybrid Mater.* **2018**, *1*, 114-126.

[201] D.O. Scanlon, K.G. Godinho, B.J. Morgan, G. W. Watson "Understanding conductivity anomalies in CuI-based delafossite transparent conducting oxides: Theoretical insights", *J. Chem. Phys.* **2010**, *132*, 024707.

[202] Z. Deng, X. Fang, R. Tao, W. Dong, D. Li, X. Zhu, "The influence of growth temperature and oxygen on the phase compositions of $CuAlO_2$ thin films prepared by pulsed laser deposition", *J. Alloys Compd.* **2008**, *466*(1-2), 408-411.

[203] M. Neumann-Spallart, S.P. Pai, R. Pinto, "PLD growth of $CuAlO_2$", *Thin Solid Films* **2007**, *515*(24), 8641-8644.

[204] A.N. Banerjee, R. Maity, P.K. Ghosh, K.K. Chattopadhyay, "Thermoelectric properties and electrical characteristics of sputter-deposited *p*-$CuAlO_2$ thin films", *Thin Solid Films* **2005**, *474*(1-2), 261-266.

[205] P.H. Hsieh, Y.M. Lu, W.S. Hwang, "Effects of RF power on the growth behaviors of $CuAlO_2$ thin films", *Ceram. Int.* **2014**, *40*(7), 9361-9366.

[206] S.H. Chiu, J.C.A. Huang, "Characterization of *p*-type $CuAlO_2$ thin films grown by chemical solution deposition", *Surf. Coat. Technol*. **2013**, *231*, 239-242,

[207] C. Bouzidi, H. Bouzouita, A. Timoumi, B. Rezig, "Fabrication and characterization of $CuAlO_2$ transparent thin films prepared by spray technique", *Mater. Sci. Eng. B* **2005**, *118*(1-3), 259-263.

[208] M. Neumann-Spallart, R. Pinto, "Growth conditions of $CuAlO_2$ films - Thermodynamic considerations", *Thin Solid Films* **2011**, *520*(4), 1299-1302.

[209] J. Pellicer-Porres, D. Martínez-García, A. Segura, P. Rodríguez-Hernández, A. Muñoz, J. C. Chervin, N. Garro, D. Kim, "Pressure and temperature dependence of the lattice dynamics of $CuAlO_2$ investigated by Raman scattering experiments and ab initio calculations", *Phys. Rev. B* **2006**, *74*, 184301.

[210] S. Li, X. Zhang, P. Zhang, X. Sun, H. Zheng, W. Zhang, "Preparation and Characterization of Solution-Processed Nanocrystalline *p*-Type $CuAlO_2$ Thin-Film Transistors", *Nanoscale Res. Lett.* **2018**, *13*, 259.

[211] N. Benreguia, A. Barnabe, M. Trari, "Sol–gel synthesis and characterization of the delafossite $CuAlO_2$", *J. Sol-Gel Sci. Technol.* **2015**, *75(3)*, 670-679.

[212] D. Byrne, A. Cowley, N. Bennett, E. McGlynna, "The luminescent properties of $CuAlO_2$", *J. Mater. Chem C* **2014**, *2*, 7859.

[213] E. Ghanti, R. Nagarajan, "Synthesis of $CuAl_2(acac)_4(OiPr)_4$, its hydrolysis and formation of bulk $CuAl_2O_4$ from the hydrolyzed gels; a case study of molecules to materials", *Dalton Trans*. **2010**, *39*, 6056–6061.

[214] N. Tomar, E. Ghanti, A.K. Bhagi, R. Nagarajan, "Studies on the hydrolysis of $\{Cu[Al(OPri)_4]_2\}$, a single source precursor for $CuAl_2O_4$ spinel", *J. Non-Cryst. Solids* **2009**, *355*, 2657–2662.

[215] S. Liu, Z. Wu, Y. Zhang, Z. Yao, J. Fan, Y. Zhang, J. Hu, P. Zhang, G. Shao, "Strong temperature-dependent crystallization, phase transition, optical and electrical characteristics of *p*-type $CuAlO_2$ thin films", *Phys. Chem. Chem. Phys.* **2015**, *17(1)*, 557–562.